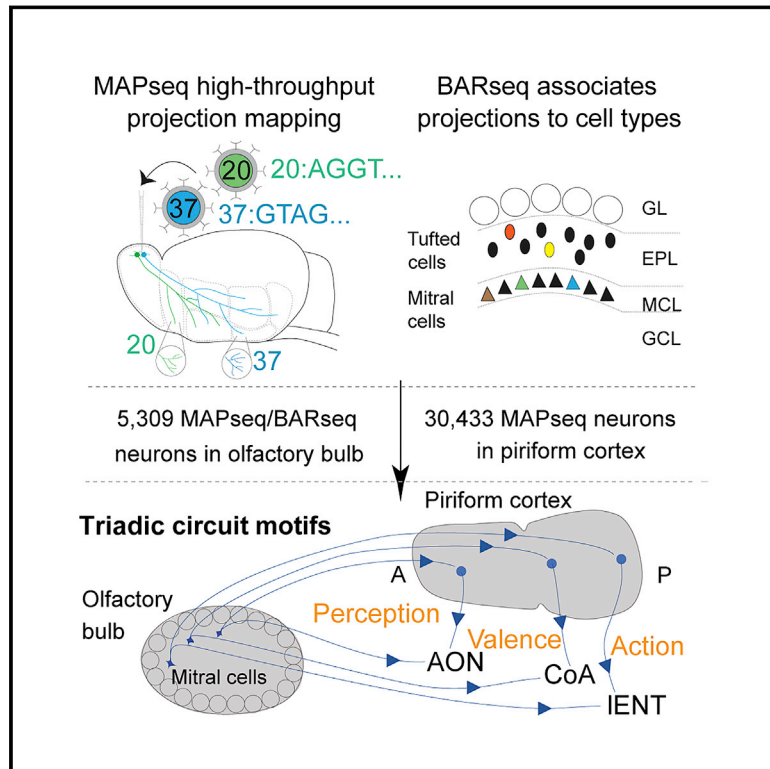


High-throughput sequencing of single neuron projections reveals spatial organization in the olfactory cortex

Graphical abstract



Authors

Yushu Chen, Xiaoyin Chen, Batuhan Baserdem, ..., Anthony M. Zador, Alexei A. Koulakov, Dinu F. Albeanu

Correspondence

albeanu@cshl.edu (D.F.A.),
koulakov@cshl.edu (A.A.K.),
zador@cshl.edu (A.M.Z.)

In brief

Contrary to the prevailing random connectivity view, high-throughput barcode sequencing reveals that the olfactory cortex connectivity is spatially structured in triadic circuit motifs along the anterior-posterior axis of the piriform cortex.

Highlights

- High-throughput barcode sequencing reveals structured olfactory neuron projections
- Mitral cell projections to the piriform cortex and other targets are interdependent
- Piriform cortex projections to other target regions are organized along the A-P axis
- Mitral cell and piriform cortex projections form matched triadic circuit motifs



Article

High-throughput sequencing of single neuron projections reveals spatial organization in the olfactory cortex

Yushu Chen,^{1,5} Xiaoyin Chen,^{1,3,5} Batuhan Baserdem,² Huiqing Zhan,¹ Yan Li,¹ Martin B. Davis,¹ Justus M. Kebschull,^{1,4} Anthony M. Zador,^{1,*} Alexei A. Koulakov,^{1,*} and Dinu F. Albeanu^{1,6,*}

¹Cold Spring Harbor Laboratory, Cold Spring Harbor, NY 11724, USA

²Stony Brook University, Stony Brook, NY, USA

³Present address: Allen Institute for Brain Science, Seattle, WA 98103, USA

⁴Present address: Department of Biomedical Engineering, Johns Hopkins School of Medicine, Baltimore, MD 21205, USA

⁵These authors contributed equally

⁶Lead contact

*Correspondence: albeanu@cshl.edu (D.F.A.), koulakov@cshl.edu (A.A.K.), zador@cshl.edu (A.M.Z.)

<https://doi.org/10.1016/j.cell.2022.09.038>

SUMMARY

In most sensory modalities, neuronal connectivity reflects behaviorally relevant stimulus features, such as spatial location, orientation, and sound frequency. By contrast, the prevailing view in the olfactory cortex, based on the reconstruction of dozens of neurons, is that connectivity is random. Here, we used high-throughput sequencing-based neuroanatomical techniques to analyze the projections of 5,309 mouse olfactory bulb and 30,433 piriform cortex output neurons at single-cell resolution. Surprisingly, statistical analysis of this much larger dataset revealed that the olfactory cortex connectivity is spatially structured. Single olfactory bulb neurons targeting a particular location along the anterior-posterior axis of piriform cortex also project to matched, functionally distinct, extra-piriform targets. Moreover, single neurons from the targeted piriform locus also project to the same matched extra-piriform targets, forming triadic circuit motifs. Thus, as in other sensory modalities, olfactory information is routed at early stages of processing to functionally diverse targets in a coordinated manner.

INTRODUCTION

The structure of intra- and inter-brain region connectivity provides a scaffolding for neural computation (Brewer and Barton, 2016; Chklovskii and Koulakov, 2004; Harding-Forrester and Feldman, 2018; Kaas, 1997; Knudsen et al., 1987; Nauhaus and Nielsen, 2014). Neuronal connectivity across different sensory modalities (vision, audition, somato-sensation, etc.) is organized into topographic maps of relevant stimulus features such as spatial location, orientation, sound frequency or body location (Blockus and Polleux, 2021; Brewer and Barton, 2016; Harding-Forrester and Feldman, 2018; Kaas, 1997; Knudsen et al., 1987; Nauhaus and Nielsen, 2014; Uchida et al., 2014a; Wilson and Sullivan, 2011). This structured organization reflects the computations that a neural circuit performs, and thereby provides a window into how each sensory system processes its inputs.

In this respect, olfaction has traditionally been considered fundamentally different from other sensory modalities. Despite a large body of work across several decades (Bekkers and Suzuki, 2013; Choi et al., 2011; Franks et al., 2011; Ghosh et al., 2011; Giessel and Datta, 2014; Gottfried, 2010; Haberly, 1985, 2001; Haberly and Price, 1977; Hagiwara et al., 2012; Igarashi et al., 2012; Johnson et al., 2000; Luskin and Price, 1982; Miyamichi et al., 2011; Nagayama et al., 2010; Price, 1973; Ren-

naker et al., 2007; Scott et al., 1980; Skeen and Hall, 1977; Sosulski et al., 2011; Stettler and Axel, 2009), no apparent structure has been found in the mammalian olfactory bulb (OB) projections to the olfactory cortex (piriform) or the intra-piriform recurrent connectivity. This is in striking contrast with the structured connectivity observed in all other sensory modalities. Thus, in the absence of evidence of structure, the olfactory cortex has been modeled as a *tabula rasa* network. Because piriform cortex circuits were presumed to be devoid of innate structure, models of cortical olfactory learning have assumed random connectivity (Babadi and Sompolinsky, 2014; Hiratani and Latham, 2020a, 2020b; Krishnamurthy et al., 2017; Litwin-Kumar et al., 2017; Schaffer et al., 2018; Schoonover et al., 2021; Srinivasan and Stevens, 2019; Stern et al., 2018; Wilson et al., 2017), and were proposed to rely entirely on plasticity to construct meaningful representations. Previous work, however, also reported anatomical and functional differences between the anterior and posterior parts of olfactory cortex (Calu et al., 2007; Haberly, 2001; Haberly and Price, 1978; Kadohisa and Wilson, 2006; Large et al., 2018; Millman and Murthy, 2020; Poo et al., 2022; Sanders et al., 2014; Wang et al., 2020b). To date, it remains unknown how such differences relate to the apparent unstructured nature of the inputs and local piriform cortex connectivity.



Here, we have revisited the question of structure in the olfactory cortex circuit. We asked whether newer and more sensitive methods might uncover structure in the olfactory cortex representations where none had previously been observed. Enabled by high throughput of mapping connectivity using Multiplexed Analysis of Projections by Sequencing (MAPseq) (Chen et al., 2019; Han et al., 2018; Huang et al., 2020; Kebschull et al., 2016; Sun et al., 2021), we mapped the brain-wide projections of thousands of individual output neurons originating from both the OB (5,309) and piriform cortex (30,433). To begin, we mapped the projections of the bulb and piriform cortex output neurons agnostic of their inputs, aiming to investigate in an unbiased manner the connectivity rules between these brain regions. The high yield of these methods and the resulting sample sizes—two to three orders of magnitude larger than in previous studies—reveal the wiring between the bulb, piriform cortex, and extra-piriform bulb targets at unparalleled scale and resolution.

Our findings challenge the prevailing belief of random connectivity in olfactory cortex and, instead, reveal structure and specificity in connections. We demonstrate a systematic relationship between the inputs from the OB to the piriform cortex and the piriform cortex outputs. We identify non-random features of connectivity in the form of structured, matching input-output projection gradients along the anterior-posterior (A-P) axis of the piriform cortex with respect to connections to extra-piriform regions, as well as local connectivity within the piriform cortex. We find that single neurons in the bulb targeting a specific region of piriform cortex also project with high probability to other brain regions that are targeted by individual piriform cortex neurons in that locality, forming triadic circuit motifs. Our results suggest that, as reported for other brain circuits (e.g., “what/where” pathways in vision), olfactory information is routed to functionally diverse targets in a coordinated manner along parallel streams.

RESULTS

Mapping the brain-wide projections of olfactory bulb outputs using neuronal barcoding

To date, identifying structure in the connectivity of the mammalian olfactory cortex has been impeded by the scarcity of single-cell connectivity data available (Srinivasan and Stevens, 2019), despite recent advances in optical imaging-based single-neuron tracing (Peng et al., 2020; Winnubst et al., 2019). Owing to the extensive intertwining of neural processes, axonal tracing studies reconstructed only dozens of individual bulb-to-cortex projections (Ghosh et al., 2011; Igarashi et al., 2012; Nagayama et al., 2010; Sosulski et al., 2011), a number insufficient for analyzing the statistics of their branching patterns across multiple target regions. We reasoned that massively increasing the number of single neurons mapped, as well as interrogating the projections of multiple brain regions at cellular resolution, may uncover organization in projection patterns that was previously missed based on limited single-cell tracing data. Toward these goals, we leveraged the throughput of sequencing-based neuro-anatomical approaches. Specifically, we used two single-neuron projection mapping techniques: MAPseq and Barcoded Anatomy Resolved by sequencing (BARseq) (Chen et al., 2019; Han

et al., 2018; Huang et al., 2020; Kebschull et al., 2016; Sun et al., 2021) (Figures 1A–1C, S1, and STAR Methods).

The somata of principal neurons of the OB, the mitral and tufted cells, are positioned across different layers and differ in size, morphology, intrinsic excitability, local wiring, and projection patterns (Burton and Urban, 2014; Fukunaga et al., 2012; Geramita and Urban, 2017; Geramita et al., 2016; Gire et al., 2012; Igarashi et al., 2012; Jordan et al., 2018; Kapoor et al., 2016; Nagayama et al., 2010; Otazu et al., 2015; Yamada et al., 2017). To distinguish mitral from tufted cells and possibly other bulb output neurons, we applied BARseq to a subset of the sampled brains. BARseq builds upon MAPseq, but additionally uses *in situ* sequencing to spatially resolve barcoded somata, thus enabling one to distinguish output neuron types barcoded in the injection area based on their laminar locations (Figure 1D). We collected tissue from the major OB projection targets at 200 μm resolution along the A-P axis of the brain, including the anterior and posterior piriform cortex (APC/PPC), the anterior olfactory nucleus (AON), the olfactory tubercle (OT), olfactory striatum, cortical amygdala (CoA), and the lateral entorhinal cortex (IENT). In total, we mapped the projections of 5,309 olfactory bulb output neurons (415 neurons from two brains using BARseq, and 4,894 neurons from six brains using MAPseq), amounting to two orders of magnitude more individual neuronal projections than all previous single-cell studies of bulb connectivity combined.

The distribution of olfactory bulb projections to their targets displays structured correlations

To determine the statistical structure of olfactory bulb projections, we first used BARseq to identify mitral and tufted cells based on the location of their somata (Figures 1D and 1E). We defined putative mitral cells (pMC) as those with somata in the mitral cell layer and putative tufted cells (pTC) as those with somata in the external plexiform layer (STAR Methods). Consistent with previous reports (Haberly and Price, 1977; Igarashi et al., 2012; Nagayama et al., 2010; Scott et al., 1980; Skeen and Hall, 1977; Zeppilli et al., 2021), pTC predominantly projected to the AON and/or OT, whereas mitral cells sent their axons broadly throughout the olfactory stream and displayed strongest projections to the anterior-to-posterior piriform cortex (Figure 1E). Interestingly, we also found a small, but distinct, third group of putative deep cells (pDC) in the granule cell layer that resembled deep short axon cells previously reported to innervate higher olfactory areas (Eyre et al., 2008; Kosaka and Kosaka, 2007). Therefore, BARseq identifies and recapitulates known differences in the projection of olfactory bulb output neurons.

Although BARseq can distinguish cell types based on their somata positions, MAPseq can map the projections of a larger number of neurons. However, because the precise locations of the barcoded neurons are unknown in MAPseq, we cannot directly determine their identities. To take advantage of the higher throughput of MAPseq and distinguish across different neuronal types, we next used the BARseq dataset as a template to classify 4,894 bulb output neurons whose projections we mapped using MAPseq. We trained and cross-validated a neural network-based probabilistic classifier to assign each

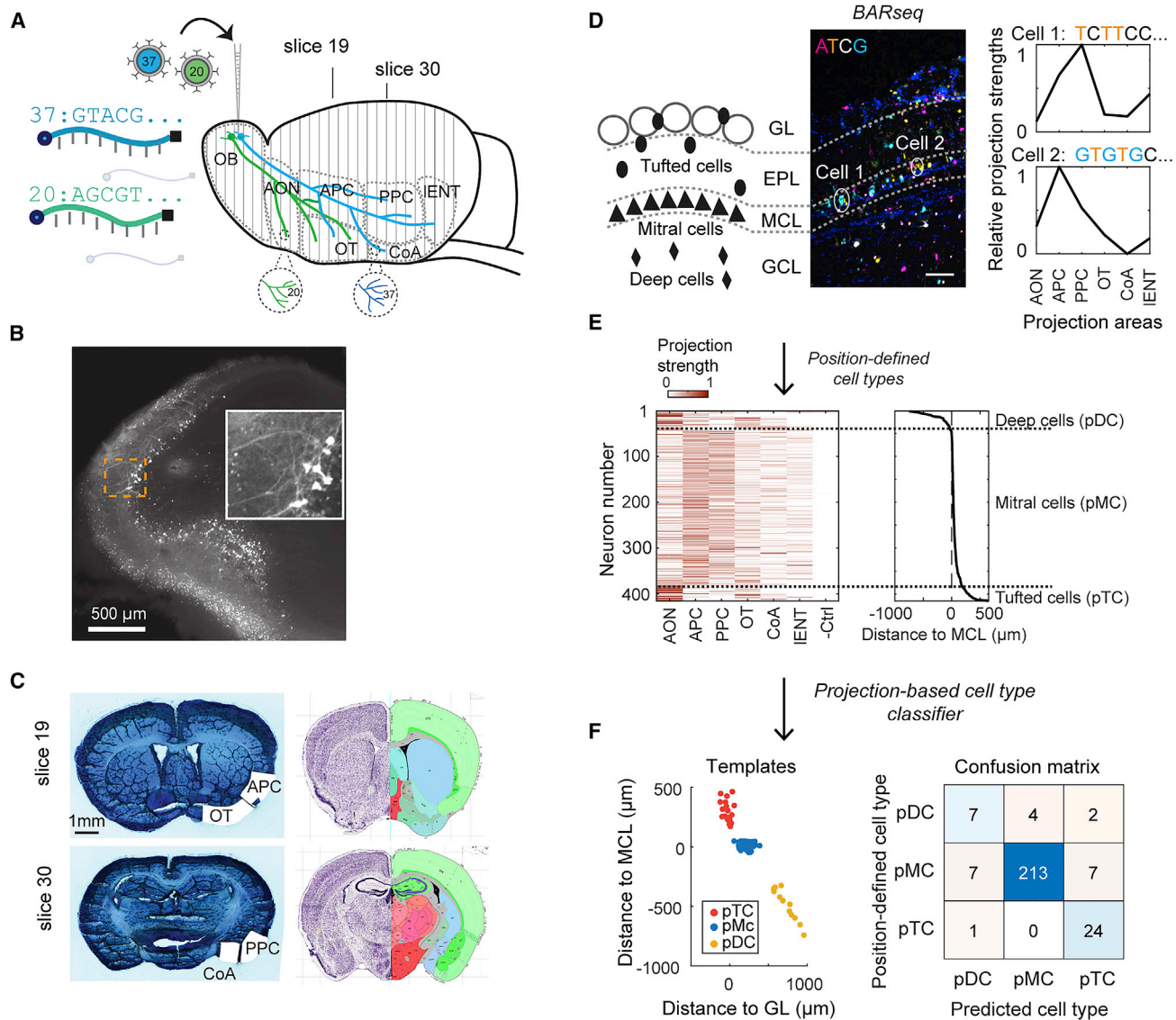


Figure 1. MAPseq and BARseq projection mapping of individual olfactory bulb neurons

(A) Schematics of the MAPseq strategy which uses RNA barcodes to label neurons and map their brain-wide projections.

(B) Infection of mitral and tufted cells by Sindbis virus carrying the barcodes and a fluorophore (EGFP).

(C) Laser Capture Micro-Dissection of target brain regions from Nissl stained coronal sections registered to the Allen Brain reference atlas.

(D) Illustration of laminar positions of mitral, tufted, and deep cells (left) and an example BARseq sequencing image of the barcoded cells (center). The first several bases of the barcode sequences in two example neurons analyzed via BARseq and their projection patterns across 6 bulb target regions (right). Scale bar = 100 μm.

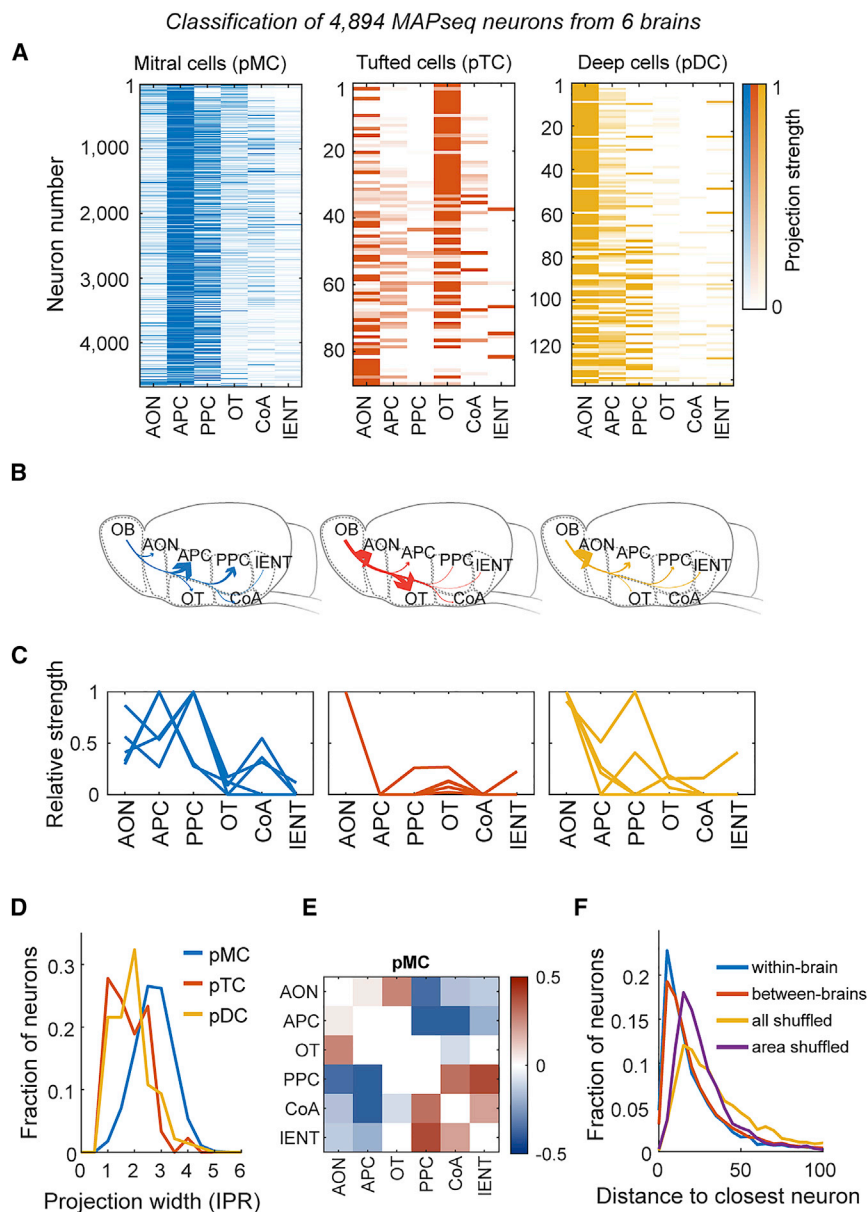
(E) (Left) projection patterns (415 neurons, 2 mice) identified via BARseq and their soma locations relative to the mitral cell layer (MCL). Columns represent bulb projection target regions and rows indicate individual neurons. (right) Cell identities based on soma positions. Projection strength of each barcoded neuron has been normalized so that the maximum strength is 1 (row).

(F) (Left) Soma positions of template neurons shown relative to MCL (y axis) and to glomerular layer (x axis) that were used to train the projection-based classifier. The sectioning planes are not necessarily perpendicular to the mitral cell layer, and thus the distances measured may be inflated. Neuronal identity (colors) is based on laminar positions (tufted, mitral, and deep cells). (Right) Classification confusion matrix of all three cell classes using the BARseq-based classifier versus position-defined classes.

See also Figures S1 and S2.

neuron to the most likely type (mitral, tufted or deep cell) given its projections across the bulb target regions sampled. As ground truth for the classifier, we used the cell types defined by their somatic locations measured via BARseq (Figure 1F, S2A–S2G, and STAR Methods). In both BARseq and MAPseq

experiments, viral injections were targeted to the mitral cell layer, allowing far more pMC to be infected than pTC and reflecting differences in cell density (Figures 1B, D, E, 2A, STAR Methods). Indeed, running the classifier on neurons mapped using MAPseq, we identified 4,665 pMC, 90 pTC, and 139



pDC (Figures 2A–2C). The projection patterns of the classified neurons were distinct across types and were consistent with BARseq-identified neurons of the same type (Figure 1E). Because of the prevalence of labeling in the mitral cell layer, we focused most of the subsequent analysis on a subset of pMC neurons (4,388) classified with high confidence (>85% classification accuracy; Figure S2H, STAR Methods).

Unlike pTC and pDC, individual mitral cells branched and projected broadly (Figures 2A–2D). To quantify the sparseness of projections, we calculated the inverse participation ratio (IPR), a metric which describes how many brain regions individual mitral cells project to (Figures 2D, S2I, and STAR Methods). Higher IPR values indicate more uniform projections (IPR of pMC is 2.71 ± 0.69 mean \pm SD, compared to 1.79 ± 0.66 for pTC and 1.90 ± 0.66 for pDC; $p < 10^{-10}$ comparing pMC to

Figure 2. MAPseq reveals structured correlations in the distribution of olfactory bulb projections to their targets

(A–C) The projection patterns of all MAPseq analyzed neurons (A), their mean projection patterns (B), and five example neurons (C) of the three classes of bulb projection neurons identified via a BARseq-based classifier. In (A), columns represent target brain regions and rows individual bar-coded neurons. Bar-coded neurons are sorted by the probability of cell type classification based on running their projection patterns through the classifier.

(D) Distribution of the broadness of projections, as measured by inverse participation ratio (IPR), x axis) at brain region-level.

(E) Pearson correlation between putative mitral cell (pMC) projections to different target regions. Only correlations that passed statistical significance after Bonferroni correction are shown.

(F) Distribution of the city block distance between the projection patterns of each pMC identified using the BARseq-based classifier and the most similarly projecting pMC within the same brain (blue), across brains (6) (red), across brains after shuffling all elements in the projection matrix (yellow), or after shuffling neuron identities for each area separately (purple).

See also Figures S1, S2, S3, and S5.

pTC, and pMC to pDC, rank-sum test after Bonferroni correction). These observations raise the question of whether the axons of individual pMC project randomly, or if instead the projections are structured in some way. For example, one group of mitral cells might project preferentially to one subset of targets, whereas another group might favor a different subset of targets. To test this hypothesis, we calculated the Pearson correlation between pMC projections to different bulb targets. Indeed, bulb projections to the AON were correlated with bulb inputs to OT (Figures 2E and S2J

for pMC; $r = 0.26$, $p < 10^{-10}$ after Bonferroni correction; Figure S2K for pTC and pDC), whereas projections to the PPC were correlated with projections to the CoA and IENT (Figures 2E, S2J; $r = 0.31$, $p < 10^{-10}$ between PPC and CoA, and $r = 0.39$, $p < 10^{-10}$ between PPC and IENT after Bonferroni correction; Figure S2K for pTC and pDC). Consistent with the presence of correlations in the projections of individual pMC to bulb targets, shuffling projections across cells to each target independently of other regions significantly increased the minimal distance in projection space between pairs of pMC (Figure 2F; $p < 10^{-10}$, rank-sum test). In agreement with previous work (Miyamichi et al., 2011; Scott et al., 1980), we also identified differences in the connectivity of pMC originating from the dorsal versus ventral olfactory bulb aspects (Figures S3A–S3C and STAR Methods), but no biases along the A–P axis of the bulb

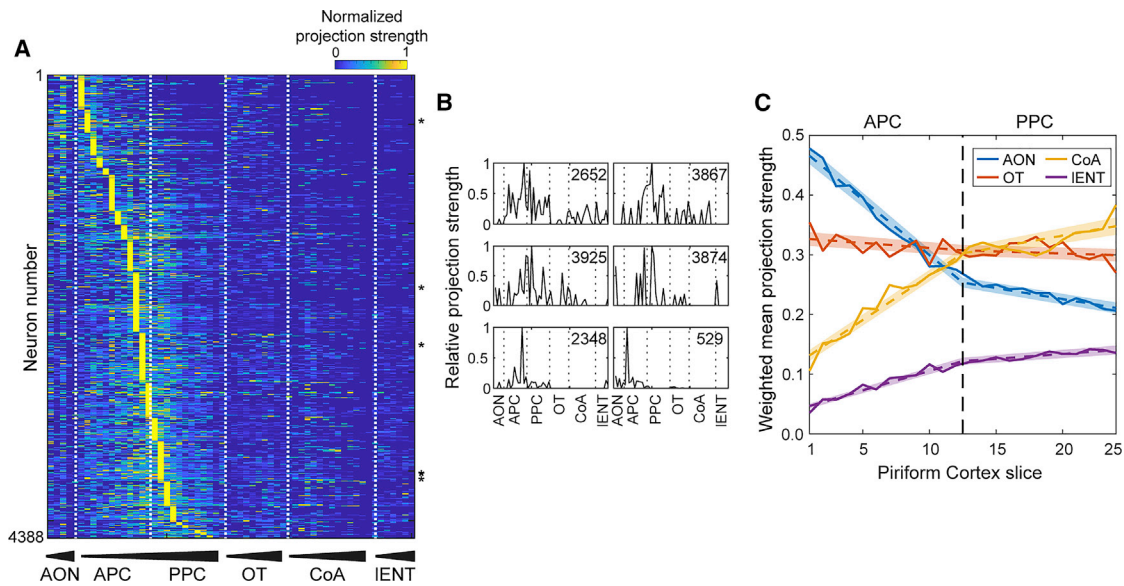


Figure 3. Olfactory bulb pMC projections tile the anterior-posterior axis of the piriform cortex and are interdependent with co-projections to extra-piriform target regions

(A) Projections patterns of pMC neurons at 200 μm resolution along the piriform cortex A-P axis. Rows represent neurons and each column a single 200 μm section in the brain region indicated at the bottom. Within each region, slices are arranged by A-P position, with the most anterior sections on the left.

(B) Projection patterns of example pMC neurons normalized by maximum barcode count for each neuron. Neuron numbers indicated on top of each plot correspond to the fiduciary marks in (A).

(C) Weighted mean projection strength for olfactory bulb neurons to four major extra-piriform targets as function of location of piriform cortex co-innervation [the conditional probability of co-innervation $P(\text{target}|\text{PC location})$, solid lines]. Dashed lines/shaded areas show piecewise linear fits in anterior (APC) and posterior (PPC) piriform cortex with 95% confidence interval obtained by bootstrap.

See also [Figures S4](#) and [S5](#) and [Table S1](#).

([Figures S3D–S3F](#)). In summary, individual pMC form several axonal branches that target multiple brain structures, but this connectivity is structured, with specific combinations of regions targeted in a correlated manner.

Olfactory bulb-to-piriform cortex connectivity along the A-P axis and bulb co-innervation of extra-piriform target regions are interdependent

Anterior and posterior piriform cortex each span ~ 2.5 mm along the A-P axis. Axons of individual pMC targeting the piriform cortex branch extensively and co-innervate several functionally distinct extra-piriform targets ([Gadziola and Wesson, 2016](#); [Kikuta et al., 2010](#); [Oettl et al., 2016, 2020, 2020](#); [Root et al., 2014](#); [Tsao et al., 2018](#); [Wang et al., 2018](#)). To better understand the logic of these projections, we investigated whether the finer spatial pattern of individual olfactory bulb neuron projections within the piriform cortex is related to their co-projections to extra-piriform targets. To test this hypothesis, we computed the conditional probability $P(\text{target}|\text{PC location})$ for each barcode sequence to be found in the four extra-piriform regions sampled (*target*), conditioned on the probability of finding the same barcode sequence at a given piriform cortex location along the A-P axis (at 200 μm resolution; [Figures 3A–3C](#), [S4A–S4C](#), and [STAR Methods](#)). Hence, this metric describes the rate (projection strength) at which bulb output neuron axons co-innervate the other four extra-piriform bulb major targets as a function of which location in the piriform cortex they innervate.

Remarkably, the conditional probability $P(\text{target}|\text{PC location})$ displayed orderly, close to linear, variation as a function of the piriform location for the AON, CoA, and IENT, but not the OT. For example, pMC projections to the AON were stronger in neurons that also innervated more strongly the anterior portion of the piriform than those projecting more strongly to the posterior portion ([Figure 3C](#), $\rho_{\text{AON}} = -0.99$, $p = 1.9 \times 10^{-23}$, Spearman correlation after Bonferroni correction; [Figures S4B](#) and [S4C](#)). Conversely, bulb inputs to the CoA and IENT were correlated with strong projections to the posterior portion of the piriform cortex ([Figure 3C](#), for CoA $\rho_{\text{CoA}} = 0.95$, $p = 6.2 \times 10^{-13}$; for IENT $\rho_{\text{IENT}} = 0.98$, $p = 2.7 \times 10^{-17}$, Spearman correlation after Bonferroni correction; [Figures S4B](#) and [S4C](#)). The slopes of $P(\text{target}|\text{PC location})$ along the A-P axis were characteristically distinct for different brain regions (AON versus IENT versus CoA; [Figure 3C](#)) and, furthermore, were different across anterior and posterior piriform cortex ([Figure 3C](#), $p < 0.005$ for AON, CoA, and IENT; p values calculated using bootstrap and Bonferroni correction). The observed interdependence of projections has not been reported to date, possibly because previous datasets were too small for these patterns to become apparent ([Figure S4D](#)).

One possible explanation for these relationships is that projections simply “disperse” locally around a target area ([Chklovskii and Koulakov, 2004](#); [Chklovskii et al., 2002](#); [Stevens, 2007](#); [Wang and Kennedy, 2016](#)). This model predicts that pMC projections to OT, which neighbors anterior but

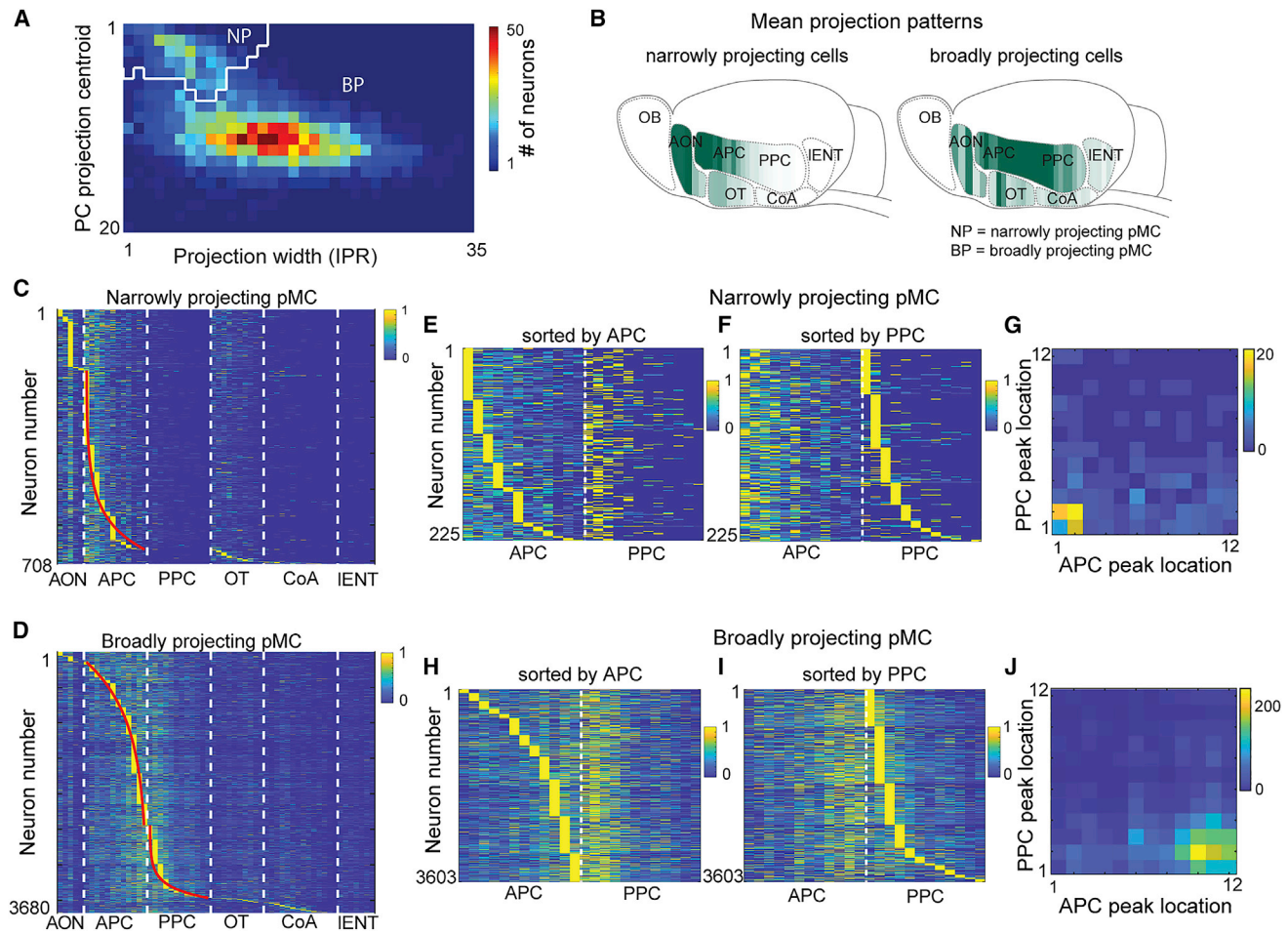


Figure 4. Narrowly and broadly projecting pMC tile differentially the anterior-posterior axis of the piriform cortex

(A) Distribution of neurons as function of projection centroid and projection width (inverse participation ratio [IPR]). Two types of neurons form distinct clusters, the NP and BP putative mitral cells (pMC) (NP and BP). Watershed clustering identifies a separatrix (white line) for the distributions of these two populations.

(B) Heat maps of mean projection patterns of NP and BP neurons.

(C and D) Projection patterns of individual NP (C) and BP (D) pMC across target regions at 200 μ m resolution. Neurons are sorted by peak projection positions across all slices. The maxima of NP cells were predominantly located in anterior rather than PPC. Red curves in the anterior piriform cortex (APC) show fits with exponential [Equation 1] and inverted exponential [Equation 2] functions for NP and BP cell projection strength maxima respectively along the A-P axis. Similarly, the red curve in the PPC (D) shows an exponential fit for the BP projection strength maxima along the A-P axis.

(E and F) NP neurons that project to both the APC and PPC, sorted independently by the strength of their projection maxima along A-P axis of APC (E) and PPC (F). (H and I) Same for BP neurons, sorted by the strength of their projection maxima along the A-P axis of APC (H) and PPC (I). Colors indicate the projection strength at a given location with respect to the maximum projection to APC or PPC.

(G and J) Density plots of the distribution of peak projection positions of the same neurons within APC (x axis) and their peak projection positions in PPC (y axis). Colors indicate number of neurons.

See also Figure S6.

not posterior piriform cortex, would also show a gradient along the A-P axis of the piriform cortex. However, such a gradient was not observed, suggesting that the locality model is not sufficient to account for our findings (STAR Methods). These relationships were robust across individuals (Figure S4B) and were corroborated at the population level using several CAV-2 Cre retrograde labeling experiments (Figures S5A–S5C, STAR Methods). Thus, the distribution of olfactory bulb co-innervation of extra-piriform regions varies in a systematic and specific manner with the location of projection along the A-P axis of the piriform cortex.

Projections of narrowly and broadly projecting pMC differentially tile the A-P axis of the piriform cortex and innervate distinct domains of extra-piriform bulb target regions

Further analysis identified two distinct pMC populations—“narrowly projecting” (NP) and “broadly projecting” (BP)—according to the width and location of projections to both the piriform cortex and extra-piriform targets (Figures 4A–4D, S6, and STAR Methods). The NP population was smaller (~20%) and displayed a more compact innervation pattern (IPR = 7.8 ± 2.8 , mean \pm SD; STAR Methods), whereas the remaining (~80%)

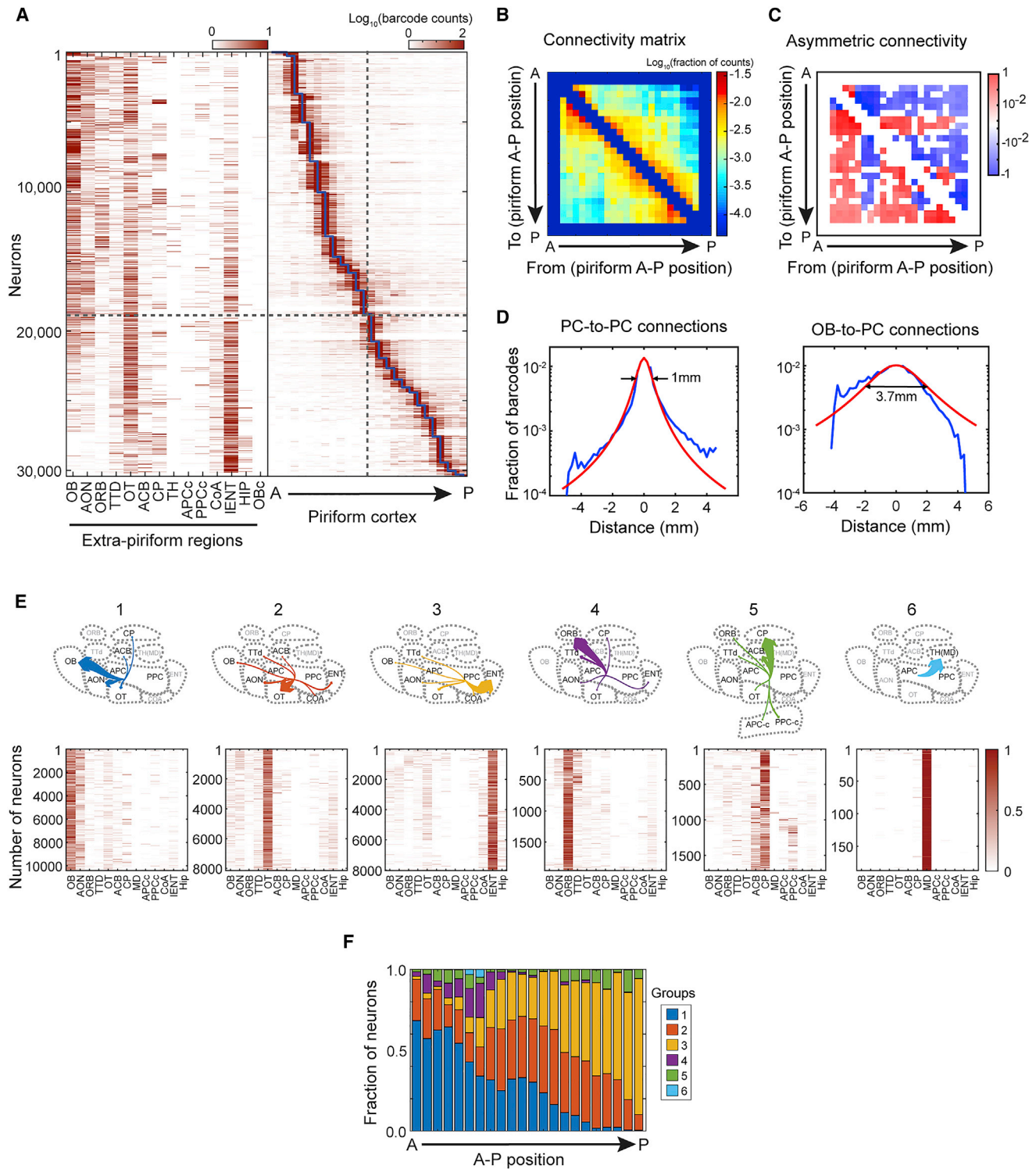


Figure 5. Projection patterns of piriform cortex output neurons are systematically organized along the anterior-posterior axis with respect to their extra-piriform targets

(A) (Left) Projection patterns of piriform output neurons to extra-piriform regions (Table S2) and (Right) within the piriform cortex along the A-P axis. Projection density is color-coded on a log scale. Projection strengths to extra-piriform brain regions (left) are further normalized on a scale of 0 to 1. In the piriform, for a given barcoded neuron the A-P position with the most barcode counts is taken as the location of the soma.

(B) Mean projection strengths (log scale) of projections from somata at the indicated locations (x axis) to the specific A-P positions within the piriform (y axis).

(legend continued on next page)

BP pMC formed more diffuse projections (IPR = 15.2 ± 5.6 , Figure 4A). NP cells targeted more strongly the anterior part of APC (Figures 4B and 4C), whereas the BP population innervated predominantly the caudal part of APC and the boundary between the anterior and posterior piriform cortex (Figures 4B and 4D). Both NP and BP populations tiled the A-P axis of the anterior piriform cortex, but their maximum projection density locations followed different distributions (Figures 4C and 4D). We observed a similar coverage without gaps of the posterior piriform cortex A-P axis by BP cells, but the maxima of NP cells were predominantly located in APC rather than PPC (Figures 4C and 4D). When sorting the NP cells according to the location of their peak projection in the anterior piriform cortex, these cells formed a distribution well-described by an exponential function (red curve in Figure 4C, STAR Methods):

$$x(n) = w \exp[-\alpha(N - n) / N]. \quad (\text{Equation 1})$$

where x is the distance of the projection maximum from the APC anterior boundary, w the width of APC extent along the A-P axis, n the cell's rank according to the sorted location, N the total number of cells in the narrowly projecting population, and $\alpha = 3.8$ the fitting parameter. The projection density of narrowly projecting cells as a function of A-P location in the anterior piriform cortex can be represented by: $\rho(x) = |dn/dx| = N/\alpha x$. Thus, the density of inputs from NP cells diverges near the anterior APC boundary (i.e., when $x \rightarrow 0$, density of inputs is very high).

In comparison, the tiling of the anterior piriform cortex by BP cells was best described by an inverted exponential relationship given by (red curve in Figure 4D):

$$x(n) = w[1 - \exp(-\alpha n / N)] \quad (\text{Equation 2})$$

with $\alpha = 2.9$. Equation 2 shows that the density of piriform cortex innervation for BP cells increases toward the posterior APC boundary, i.e., when $x \rightarrow w$, $\rho(x) = N/\alpha(w - x)$ (Figure 4D). Finally, the tiling of the posterior piriform cortex by BP cells was also accurately described by an exponential distribution, similar to the coverage of the APC by the NP cells [Equation 1 with $\alpha = 6.5$]. For both BP and NP cells, the locations of maximum projections of the same neuron along the A-P axis in the posterior piriform cortex were not correlated with the locations of maxima in the anterior piriform cortex (Figure 4E–4J, S6E–S6J, and STAR Methods), raising the possibility that local neural circuits in these two cortical subdivisions perform

different computations and extract distinct features of odor inputs. Furthermore, the distributions of projection peaks along the A-P axis in each of the extra-piriform bulb targets sampled were distinct for the NP and BP populations (Figure S6B): BP cells projected more posterior in OT ($p < 10^{-10}$), CoA ($p < 10^{-10}$), and IENT ($p < 10^{-10}$), but more anterior in the AON ($p < 10^{-10}$) compared to NP cells.

We investigated whether differences in projection between the NP and BP cells could account for the gradients described along the piriform A-P axis. Area-level correlations between projections to the piriform cortex and extra-piriform targets were weaker when analyzing NP and BP neurons independently versus all pMC jointly (Figure S6C), suggesting that these differences partially accounted for the brain region-level correlations observed. Nonetheless, at single slice resolution, the strength of co-projection to the AON was higher for both NP and BP neurons targeting the anterior versus posterior part of the piriform cortex. Similarly, the strength of co-projection to CoA and IENT was higher for narrowly and broadly projecting cells targeting the posterior versus anterior part of the piriform, forming orderly gradients (Figure S6D and Table S1). Thus, the relationships described above (Figure 3C) between the anterior-posterior spatial patterns of individual bulb neuron projections within the piriform cortex and their extra-piriform co-projections were preserved for both populations of mitral cells.

In summary, the olfactory bulb-to-piriform cortex connectivity along the A-P axis is interdependent with the bulb co-innervation of extra-piriform targets across different cell types (mitral versus tufted cells; Igarashi et al., 2012; Nagayama et al., 2010), between two populations of mitral cells (NP and BP), and within the NP and BP populations. Thus, these systematic relationships between projections to the piriform cortex and extra-piriform areas likely reflect a general wiring principle.

Piriform cortex output neurons distributed along the anterior-posterior axis project to different target regions

The correlations identified between the bulb projections along the A-P axis of the piriform and the strength of their co-innervation of extra-piriform targets, together with reports on asymmetric rostro-caudal intra-piriform inhibition (Large et al., 2018; Luna and Pettit, 2010) and biases in the piriform cortex output projections (Chen et al., 2014; Diodato et al., 2016; Mazo et al., 2017), raised the possibility that downstream piriform cortical circuitry is also organized along A-P spatial gradients. To test this hypothesis, we used MAPseq to analyze the projections of the piriform cortex output neurons spanning 5 mm along the

(C) Differences in reciprocal projections between two A-P positions in piriform obtained by calculating the difference between the connectivity matrix (B) and its transpose. Blue indicates stronger projection in the posterior direction, and red indicates stronger projection in the anterior direction.

(D) (Left) The strength of intra-piriform projections relative to their soma locations (blue). Red line indicates fit using an inverse power law model (Lorentzian function, STAR Methods). The density of projections decreases by half at about 0.5 mm from estimated soma location, making the projection width ~ 1 mm at 50% density (arrows). Contribution from the dendritic neuropil of barcoded neurons was minimized by removing slices adjacent to the peak of barcode molecule counts (STAR Methods). (Right) Same distribution obtained for pMC is substantially broader.

(E) Mean projection patterns (top) and projection patterns of individual neurons (bottom) of groups of piriform cortex output neurons to extra-piriform target regions.

(F) Fraction of neurons belonging to each group at the indicated A-P positions within the piriform cortex. Same color codes are used in (E) and (F). See also Figure S7 and Table S2.

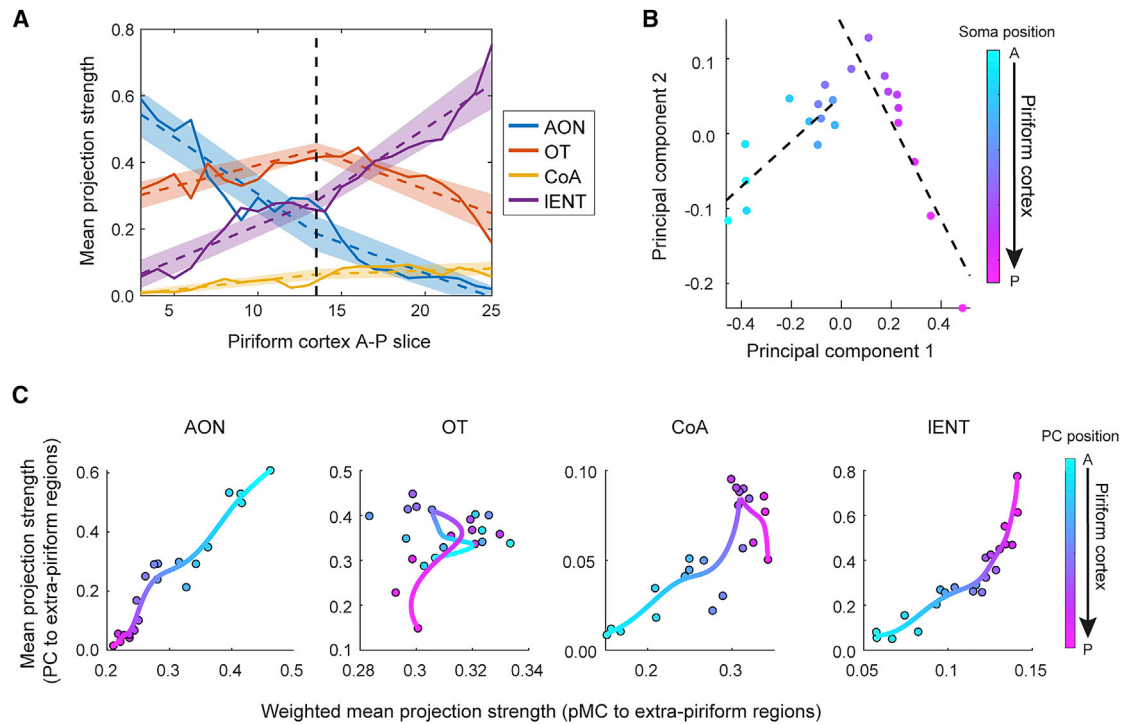


Figure 6. Matched input and output circuit motifs in the piriform cortex

(A) Mean projection patterns of piriform cortex output neurons at the indicated A-P position of barcoded somata in piriform cortex. Dotted lines indicate linear fits and shaded areas the range of fits from bootstrap.

(B) Mean loadings for the first two principal components of the mean projection strengths of piriform output neurons to the AON, CoA, IENT, and OT sampled at the indicated A-P positions in the piriform cortex. Dotted lines indicate linear fits for APC and PPC.

(C) Mean projection strengths of piriform projection neurons to extra-piriform target regions, organized by the location of their somata along the piriform A-P axis (y axis) plotted against the mean projection strengths of pMC neurons to extra-piriform bulb target regions weighted by projections to a particular A-P position in piriform cortex, $P(\text{target}|\text{PC location})$ (x axis). Colors indicate A-P positions in the piriform cortex.

See also [Figures S7](#) and [S8](#) and [Table S1](#).

A-P axis (30,433 neurons from five mice, [Figure 5A](#)). We sampled the piriform cortex (APC and PPC, [Figure 5A](#), right) and 14 of its projection target regions ([Table S2](#) and [Figure 5A](#), left), identifying the locations of barcoded somata of the piriform cortex outputs (blue line in [Figure 5A](#), *Right*) and both their intra-piriform projections at 200 μm resolution ([Figures 5B](#), [5C](#), and [S7A](#)) as well as their projections to extra-piriform targets ([Figures S7B–S7E](#) and [STAR Methods](#)).

We found that the intra-piriform connections of the piriform cortex output neurons, though fairly long-range, decrease with distance, following an inverse power law (Lorentzian function, [STAR Methods](#), [Figure 5D](#)). The density of connections dropped by approximately an order of magnitude at distances from somata of about 2 mm. Overall, the decay in intra-piriform projection strength was more substantial for the anterior than for posterior oriented connections in agreement with a previously observed anterior-to-posterior projection bias ([Datiche et al., 1996](#); [Hagiwara et al., 2012](#)) ([Figures 5A–5C](#)). The fact that mitral cell barcodes were successfully transported along several millimeters from the bulb ([Figures 3A](#) and [5D](#)), as well as previous demonstrations of long-distance (>10 mm) transport of barcodes from other brain structures ([Chen et al., 2019](#); [Huang et al., 2020](#); [Kebschull et al., 2016](#)), argued against the possibility

that the observed locality of intra-piriform connectivity was an artifact of barcode transport. Thus, a distinctive feature of intra-piriform connectivity is its power-law decay as a function of distance from somata. Although this contrasts the sharper exponential decay observed in other brain regions ([Markov et al., 2011](#); [Song et al., 2005](#); [Wang and Kennedy, 2016](#)), it points to a more local organization of the piriform cortical circuit than previously proposed in all-to-all connectivity models.

We further investigated whether the piriform cortex outputs are systematically organized along its A-P axis with respect to their extra-piriform targets. We separated the piriform cortex output neurons into six groups based on their extra-piriform projection targets using Louvain community detection ([Figure 5E](#) and [STAR Methods](#)). These groups were indeed differentially distributed with respect to the A-P position of their somata, had distinct intra-piriform connectivity, and innervated specific combinations of functionally diverse brain regions, each having a dominant target region ([Figures 5E](#), [S7F–S7K](#), and [STAR Methods](#)). For example, groups 1 and 4 projected most strongly to the OB and orbitofrontal cortex (ORB), respectively, and were enriched in the anterior piriform cortex. In contrast, neurons of group 3 projected most strongly to the IENT and were predominantly found in the posterior piriform cortex ([Figure 5F](#)). These

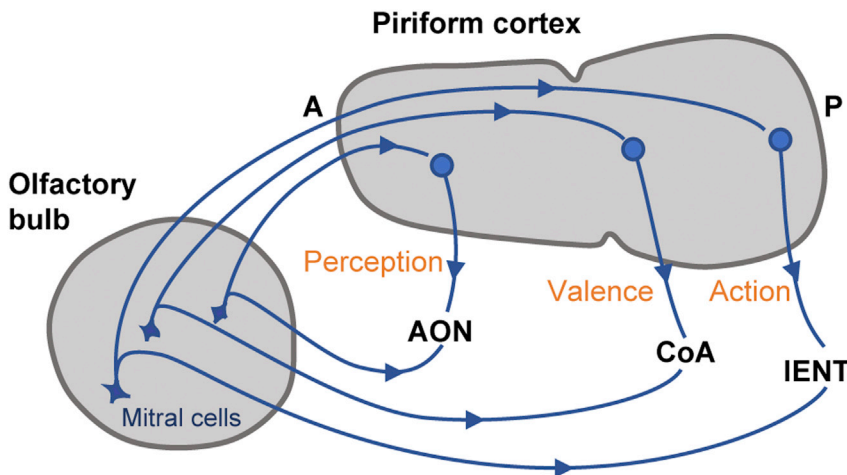


Figure 7. Cartoon schematics of parallel olfactory processing streams structured along the anterior-posterior axis of the piriform cortex according to triadic connectivity motifs

An olfactory bulb (OB) output neuron that targets the anterior portion of the piriform cortex likely also projects to the anterior olfactory nucleus (AON); and neurons in the targeted (anterior) piriform locus complete the triad by also projecting to the AON. The same triadic organization is replicated at different positions within the piriform cortex along its anterior-posterior (A-P) axis for other target regions, such as the amygdala (CoA) and lateral entorhinal cortex (IENT). We propose that the triadic circuit motifs identified along the A-P axis of the piriform cortex form the basis of parallel, functionally distinct olfactory processing streams.

differences in soma distribution for the six groups were consistent across animals (Figure S7H). In summary, piriform cortex output neurons that project to different sets of target brain regions are enriched at specific locations along the anterior-posterior axis.

Matching projection gradients of piriform cortex inputs and outputs along the anterior-posterior axis

We investigated whether the piriform cortex outputs form projection gradients reminiscent of the olfactory bulb-to-piriform cortex inputs. Consistent with the overall organization of the bulb-to-piriform cortex projections, the strength of piriform cortex output projections to the AON, IENT, and CoA varied along its A-P axis (Figure 6A). The mean strength of piriform projection to the AON decreased systematically from the anterior to the posterior end of the piriform cortex (Spearman correlation $\rho = -0.96$, $p = 2.0 \times 10^{-12}$ after Bonferroni correction), while the mean strength of the piriform projection to IENT and CoA increased (Spearman correlation $\rho = 0.77$, $p = 7.5 \times 10^{-5}$ for CoA and $\rho = 0.97$, $p = 1.2 \times 10^{-14}$ for IENT after Bonferroni correction). In contrast, piriform projections to OT appeared enriched near the anterior-to-posterior piriform cortex boundary but lacked an overall trend across the whole piriform cortex (Spearman correlation $\rho = -0.11$, $p = 1$ after Bonferroni correction). In addition, performing principal component analysis (PCA) on the projection strengths of the piriform output neurons across these four extra-piriform areas revealed a sharp change in slope at the APC/PPC boundary (Figure 6B, S7L, S7M, and STAR Methods). The observed gradients were further supported by retrograde bulk labeling experiments using fluorescent microbeads (RetroBeads) (Figures S8A–S8C). Thus, piriform cortex outputs to different brain regions form projection gradients along the A-P axis which follow different slopes in the anterior-to-posterior piriform cortex.

Because both the bulb-to-piriform cortex inputs and the piriform cortex output projections appear spatially ordered along the piriform A-P axis (Figures 3C, 5A, 5F, and 6A), we next asked whether they match. Strikingly, along the A-P axis, the mean strengths of piriform cortex projections to the AON, CoA, and IENT correlated with $P(\text{target}|\text{PC location})$ of pMC projections

to each of these brain regions (Figure 6C, Spearman correlation $\rho = 0.95$, $p = 1.6 \times 10^{-5}$ for AON, $\rho = 0.73$, $p = 6.7 \times 10^{-4}$ for CoA, and $\rho = 0.97$, $p = 1.4 \times 10^{-5}$ for IENT after Bonferroni correction). For example, neurons in the anterior part of the piriform cortex (Figure 6C, left, cyan dots) project strongly to the AON (y axis), and the pMC neurons that target this part of piriform cortex also strongly target the AON (x axis). Conversely, neurons in the posterior part of the piriform cortex (magenta dots) project weakly to the AON, matching the weak AON projections from pMC neurons that also target the posterior part of the piriform cortex. Similar matching relationships between the strength of piriform cortex output projections and of co-innervation by mitral cell inputs were also seen for CoA and IENT, but with reversed mapping along the A-P axis (i.e., strong projections from and to the posterior part of piriform cortex respectively). No robust relationship was observed for projections to the OT when performing the same analysis (Spearman correlation $\rho = 0.03$, $p = 1$ after Bonferroni correction).

Therefore, a given piriform cortex output neuron appears to be wired up such that the strength of its projection to the AON, IENT, or CoA matches the strength of its dominant bulb input's *co-projection* to the same target brain region (Figure 7). These matching gradients in the inputs and outputs of the piriform cortex, consequently, may connect co-innervation targets of individual olfactory bulb neurons (i.e., piriform and extra-piriform areas), completing triadic circuit motifs. The triadic organization is replicated at different positions within the piriform cortex, along its A-P axis, for functionally distinct targets (AON versus CoA versus IENT), suggesting that similar to other senses (i.e., vision, audition), the olfactory information is relayed to different processing streams in a coordinated manner. This organization enables parallel computations and further cross-referencing, because olfactory information reaches a given target brain region via both direct and indirect pathways.

DISCUSSION

We investigated the mesoscopic-level wiring of the olfactory bulb and cortex using high-throughput barcode sequencing-based

mapping with single-cell resolution. We identified multiple bulb-to-piriform cortex projection gradients (Figure 3), as well as a matching set of gradients in the outputs of the piriform cortex (Figure 6). We have found that characteristic groups of bulb neurons tile differentially the anterior-posterior axis of the piriform cortex (Figures 3 and 4) and that piriform cortex outputs are systematically organized along its A-P axis with respect to their extra-piriform targets (Figure 5). Our findings indicate the presence of spatially structured connectivity, both at the level of non-random combinations of olfactory bulb and piriform cortex target regions and, at finer resolution, within the piriform cortex. Furthermore, the matched input-output piriform projection gradients enable triadic circuit motifs that connect specific locations within the piriform cortex and extra-piriform bulb targets with distinct behavioral roles (Figures 6 and 7). This is consistent with anatomical and functional differences between the anterior-to-posterior piriform cortex (Bolding and Franks, 2018; Calu et al., 2007; Haberly, 2001; Haberly and Price, 1978; Kadohisa and Wilson, 2006; Millman and Murthy, 2020; Poo et al., 2022; Roesch et al., 2007; Wang et al., 2020b) and reminiscent of other sensory modalities and the limbic system. Our findings challenge the prevailing view that the olfactory cortex connectivity is a *tabula rasa* network (Babadi and Sompolinsky, 2014; Hiratani and Latham, 2020a, 2020b; Krishnamurthy et al., 2017; Litwin-Kumar et al., 2017; Schaffer et al., 2018; Schoonover et al., 2021; Srinivasan and Stevens, 2019; Stern et al., 2018; Wilson et al., 2017) and that meaningful representations of the sensory inputs emerge from scratch, entirely via plasticity during the lifetime of each individual within a randomly connected piriform network.

Structured bulb-to-piriform cortex connectivity

Previous studies have largely concluded that the olfactory bulb sends broad projections to the piriform cortex, lacking discernable spatial organization (Ghosh et al., 2011; Haberly, 2001; Haberly and Price, 1977; Nagayama et al., 2010; Scott et al., 1980; Skeen and Hall, 1977; Sosulski et al., 2011), but see (Ojima et al., 1984; Zeppilli et al., 2021). These results led to the hypothesis that the piriform cortex is an unstructured neural network. Our data instead show that OB-to-piriform cortex connectivity contains both distributed and spatially organized components. Differences in projection along the A-P axis are accompanied by distinct co-projections to extra-piriform bulb target regions. These relationships in projection patterns are found reproducibly across different cell types (mitral versus tufted cells) and subpopulations within cell types (NP and BP cells). In conjunction with previously observed gradients in the piriform cortex inhibitory connections (Large et al., 2018; Luna and Pettit, 2010), they point to a model in which the A-P location within the piriform cortex reflects a feature or a set of features of OB responses that are important for cortical processing. These features appear to *not* be represented topographically in the bulb. Furthermore, as it follows from the uncorrelated nature of NP and BP cells tiling the anterior-to-posterior piriform cortex (Figures 4G and 4J), the features represented may differ in these cortical subdivisions. We note that, although following similar trends, this spatially organized connectivity is more diffuse than in other sensory cortical areas (i.e., visual, auditory, somatosensory), suggesting that it reflects stimulus-specific features that need further investigation.

Our results suggest that a spatial organization, distinct from the topography of the odorant receptors at the level of the glomerular inputs to the bulb, emerges between the projections of individual mitral cells, the piriform cortex, and extra-piriform areas. From the standpoint of neural computation, mitral cells, but not glomeruli, represent the outputs of the olfactory bulb which convey information to the rest of the brain. Individual mitral cell responses are substantially different from the responses of glomeruli (Chae et al., 2018; Fantana et al., 2008; Gschwend et al., 2015). Furthermore, sister mitral cells, which receive primary excitatory input from the same glomerulus, are not redundant in their odor responses, but rather differ substantially in spike timing (Arneodo et al., 2018; Dhawale et al., 2010; Kikuta et al., 2013). The differences between glomerular and mitral cell responses, and the functional heterogeneity across sister cells emerge due to substantial reformatting of the inputs via both local bulb processing circuits and top-down feedback from many regions, including the olfactory cortex. Indeed, in other sensory systems, the topographic organization of the sensory inputs is not the only organization that shapes neural processing. In the visual system, for example, the retinotopy is preserved from the periphery to the thalamus, superior colliculus, and the cortex. However, in addition, different types of retinal ganglion cells process visual information differentially in distinct parallel streams. These cells extract various stimulus features (e.g., direction, object-motion, looming, etc.) (Barlow and Hill, 1963; Lettvin et al., 1959; Münch et al., 2009; Olveczky et al., 2003), and project to different brain regions (Dhande et al., 2015; Field and Chichilnisky, 2007; Sanes and Masland, 2015). The logic of projections of individual sister mitral and tufted cells grouped by glomeruli is thus separate from the spatial organization analyzed here and can be investigated further in future studies.

Function- and location-based connectivity schemes

The spatial organization of connectivity we report (Figure 3C) could in principle be understood based on spatial locality in connectivity (Chklovskii and Koulakov, 2004; Chklovskii et al., 2002; Stevens, 2007; Wang and Kennedy, 2016): axons tend to form connections to nearby neurons/areas and, consequently, the density of connections decreases as function of distance. This may emerge, for example, because brain regions are arranged so as to minimize the total length of connections (Chklovskii and Koulakov, 2004; Klyachko and Stevens, 2003). As such, the locality rule is the default model to apply to connectivity. We find, however, that several features in our data cannot be explained by this purely geometric model. First, the connectivity to the OT appears to be independent of position, despite distance to the tubercle varying substantially along the piriform A-P axis. Second, the slope of spatial dependence of connection probability differs across bulb target regions (IENT versus CoA versus AON; Figure 3C). Third, at the boundary between the anterior-to-posterior piriform cortex, we observe sudden changes in slope (Figure 6B) for projections to different extra-piriform bulb target regions. Finally, the choice of dominant projection of the piriform cortex output neurons cannot be explained by proximity of the target region to the soma location within the piriform (e.g., projections to the bulb are stronger than those to the AON; Figure 5E). Overall, these features may be better explained instead by a function-based topographical model. We

note that the function- and location-based connectivity models are not mutually exclusive. Indeed, because circuit function is expected to define connectivity, the geometry and locations of connected regions may be determined based on connection length minimization (Chklovskii and Koulakov, 2004; Klyachko and Stevens, 2003). As a consequence, location-based connectivity features may be explained by the functional needs of the circuit. Though the geometric and functional connectivity models yield similar first order spatial biases in projection, the functional model more accurately explains details in the data, such as differences in the slopes of projection variations (Figures 3C and 6A).

Local piriform cortex connectivity

We find that the density of intra-cortical connections of the piriform cortex output neurons decays as a power-law (Lorentzian) function of distance from somata (Figure 5D). The cells analyzed were identified as cortical output neurons by the presence of their barcoded projections in target regions outside of the piriform. The intra-piriform connectivity decays slower than the exponential decay observed in some brain regions (Markov et al., 2011; Song et al., 2005; Wang and Kennedy, 2016), but does not extend with equal density across the entire piriform. For example, the density of connections decays by more than an order of magnitude for loci separated by 2 mm along the A-P axis. The local nature of intra-piriform connectivity argues for spatial organization of functionality within the piriform cortex. According to classical proposals (Barnes et al., 2008; Haberly, 2001; Wilson and Sullivan, 2011), one key role of the piriform cortex is to implement pattern completion by linking neurons responding to the same stimuli. If relevant parts of these responses are distributed across the piriform cortex, as suggested by the random projection model, the associative intra-piriform circuit is expected to be highly distributed and long-range. Instead, our observations are consistent with a model in which associative connectivity within piriform cortex integrates more locally activated ensembles of neurons than expected by all-to-all connectivity (STAR Methods). Our observations constrain the rate of connectivity decay within the piriform cortex. They, however, do not provide information about whether, locally, the connections are functionally organized according to specific rules.

Matched triadic circuit motifs

Our observations suggest that a triadic connectivity motif organization is replicated at different A-P locations in the piriform cortex with respect to the AON, CoA, and entorhinal cortex. These results are consistent with the existence of different functional subnetworks (Calu et al., 2007; Li et al., 2006). The monotonicity of the piriform cortex input and output projection gradients, their specificity with respect to different extra-piriform targets (e.g., AON versus CoA or IENT), and the differences observed between piriform cortex subdivisions are further indicative of spatially ordered olfactory representations. They open venues for further investigation of the axon guidance molecular mechanisms that potentially underlie the emergence of these gradients.

Interestingly, the triadic circuit motifs identified here are reminiscent of residual neural networks (ResNet) (He et al., 2016) architectures in machine learning which overcome vanishing gradients by skipping layers, and, thus, optimize learning.

They mirror similar motifs reported in both sensory networks, such as the topographically aligned retino-tectal versus retino-thalamo-cortico-tectal projections (Cang and Feldheim, 2013; Tikidji-Hamburyan et al., 2016; Wang and Burkhalter, 2013) and in the limbic system (thalamo-amygdala versus thalamo-cortico-amygdala projections [Ledoux, 1998; LeDoux et al., 1991] or entorhinal cortex-CA1 versus entorhinal cortex-to-dentate gyrus-CA3-CA1 [Basu and Siegelbaum, 2015; van Strien et al., 2009]). This architecture enables both implementing different computations on inputs from the sensory periphery via direct and indirect pathways and crosstalk and comparisons across functional streams that converge on a given target region.

Implications for olfactory processing

The parallel triadic circuits suggest that olfactory information is organized into several processing streams. Distinct processing streams have been observed in other sensory modalities where they connect different sets of brain regions and carry different sensory information. In the visual system, where such streams were first identified, cortical information is organized into a ventral (“what”) pathway involved in perception, and a dorsal (“where”) pathway involved in action (Goodale and Milner, 1992; Mishkin and Ungerleider, 1982; Schneider, 1969). A similar two-stream what/where segregation has been proposed for auditory (Rauschecker and Romanski, 2011) and somatosensory processing (Dijkerman and de Haan, 2007). The adaptive advantage of segregating information into several streams is that features such as the identity, size, shape, orientation, and relative position of visual objects can be computed in parallel. Neurons encoding these features are then organized in multiple neuroanatomical pathways spanning the parietal and temporal lobes. Our data support the view that olfactory information leaving the bulb might similarly be segregated into perception (OB-APC-AON), valence (OB-PPC-CoA), and action (OB-PPC-IENT) pathways, structured according to the triadic connectivity motifs identified here. Interestingly, we find that the piriform cortex can be viewed as a continuous spatial map representing shifting preferences between these three pathways. Processing within the piriform cortex in conjunction with inter-connected extra-piriform targets may distill specific stimulus features represented across the olfactory bulb into functional processing maps that support perception, valence, and actions associated with odorants. Within the perception stream, the triadic circuit consisting of direct OB → APC and OB → AON projections, combined with indirect APC → AON projections, may enable efficient computation of perceptual features such as the identity, intensity, and relative timing of odorants. In this view, the OB carries raw sensory data (Chae et al., 2021), and the APC → AON pathway might carry contextual gating information needed to sift through different stimulus features based on their behavioral relevance. As AON neurons also strongly innervate the APC (Russo et al., 2020), the AON-APC bidirectional connectivity may further consolidate the computation of these features. Similarly, within the valence stream, the triadic circuit consisting of direct OB → PPC and OB → CoA projections, combined with indirect PPC → CoA projections is ideally placed to compute odor valence by mixing both innate and learned neural representations (Root et al., 2014). Finally, within the action stream, the triadic circuit

consisting of direct OB → PPC and OB → IENT projections, combined with indirect PPC → IENT projections, may support computations such as olfactory spatial navigation and fast recall of olfactory objects memories (Tsao et al., 2018; Wang et al., 2018). These triadic processing streams enable a given extra-piriform target region to compare a direct input from the bulb with a version of the same that has been processed by the piriform cortex. This view is supported by a recent study in the context of an odor-cues allocentric spatial choice task (Poo et al., 2022). The authors suggest that neurons in the PPC represent both spatial location and odor identity, enabling spatial cognitive maps, associations between odors and places during odor-cued spatial navigation, and are less likely to represent odor identity per se. In contrast with the slow rise time and long integration window for representing odor identity of the posterior piriform neurons, neurons in the APC have fast onset and sniff-locked responses and represent odor identity robustly (Bolding and Franks, 2018; Millman and Murthy, 2020; Miura et al., 2012; Schoonover et al., 2021).

Limitations of the study

Although the spatial organization of connectivity suggests interesting functional implications, our observations are based on anatomical connectivity alone, which does not necessarily correspond to functional connectivity. Furthermore, we investigated the logic of long-range projections between brain regions, but not the local synaptic connectivity within regions. Finally, each brain region contains multiple cell types with diverse properties, such as morphology, gene expression, local connectivity, and specific activity. Our data did not link the connectivity patterns of neurons directly to a set of diverse cell types. Future functional interrogation and synaptic connectivity mapping at the cell-type-level is necessary to fully resolve the olfactory circuit architecture and its functional significance.

Conclusions

In summary, our results reveal that the architecture of the olfactory cortex is structured, and thus need not rely on algorithms that assume random connectivity. We suggest an alternative model in which odor stimuli are processed along parallel, spatially segregated, functionally distinct streams. By connecting the odorant receptor molecular identity of glomeruli to the brain-wide connectivity and responses of individual neurons within the olfactory bulb, piriform cortex, and extra-piriform regions, future work will determine the relationship between functional cell types, structured connectivity, and the algorithms for processing olfactory information.

STAR★METHODS

Detailed methods are provided in the online version of this paper and include the following:

- KEY RESOURCES TABLE
- RESOURCE AVAILABILITY
 - Lead contact
 - Material availability
 - Data and code availability

- EXPERIMENTAL MODEL AND SUBJECT DETAILS

- Animals

- METHOD DETAILS

- Barcoded Sindbis viral library
- Viral labeling of olfactory bulb (OB) output neurons
- Cryo-sectioning and laser micro-dissection for MAPseq of OB outputs
- Sequencing library preparation for MAPseq of the OB outputs
- BARseq on OB slices
- Viral labeling of piriform cortex (PC) output neurons
- Cryo-sectioning and dissection for MAPseq of PC outputs
- Sequencing library preparation for MAPseq of PC outputs
- Sequencing of the MAPseq samples
- qPCR measurement of β -actin in OB target samples
- CAV-2 retrograde tracing to validate OB projections
- Retrograde tracing to validate PC outputs
- Mapping the brain-wide projections of individual olfactory bulb output neurons via MAPseq
- Classification of the olfactory bulb projection neurons
- Differences in brain-wide projections of output neurons across different domains of the olfactory bulb
- Correlations between individual neuronal bulb output projections along the A-P axis of piriform cortex and their co-projections to extra-piriform areas
- Using CAV-2 retrograde labeling to validate correlations observed in the putative mitral cell projections to the IENT and PPC

- NARROWLY AND BROADLY PROJECTING PUTATIVE MITRAL CELLS DIFFERENTIALLY TILE THE A-P AXIS OF THE PIRIFORM CORTEX

- INTRA-PIRIFORM AND BRAIN-WIDE PIRIFORM CORTEX PROJECTIONS AND COMPARISONS WITH PREVIOUS WORK

- PIRIFORM CORTEX OUTPUT NEURON GROUPS DIFFER IN THEIR DOMINANT PROJECTION TARGETS ALONG THE A-P AXIS OF THE CORTEX

- QUANTIFICATION AND STATISTICAL ANALYSIS

- MAPseq data processing
- OB projection data analysis
- IPR
- OB target region pairwise correlations
- Classifiers
- Conditional probability analysis
- Regression analysis and shuffled controls
- Down-sampling controls
- Tiling
- Piriform cortex projection data analysis
- Matching of PC input and output circuit motifs
- Statistics

SUPPLEMENTAL INFORMATION

Supplemental information can be found online at <https://doi.org/10.1016/j.cell.2022.09.038>.

ACKNOWLEDGMENTS

The authors would like to acknowledge E. Bulzomi for technical support, S. Li and A. Kepecs for providing AAV_{DJ}-DIO-{hCAR}_{off} and A. Banerjee, K.M. Franks, D. Fürth, P. Gupta, G.B. Keller, S. Lu, S. Li, F. Marbach, S. Navlakha, X. Zheng, and members of the Albeanu, Koulakov, and Zador groups for critical discussions. This work was supported by the following funding sources: BRAIN 1R01NS111673 to D.F.A. and A.A.K., TR01 5R01DC017876 to D.F.A. and A.A.K. and Simons Foundation (350789) to X.C.

AUTHOR CONTRIBUTIONS

D.F.A. and A.A.K. conceived the study. Y.C., X.C., B.B., D.F.A., A.A.K., and A.M.Z. contributed to the design of experiments and data analysis. Y.C., X.C., H.Z., J.M.K., and Y.L. performed MAPseq/BARseq experiments. M.B.D. and Y.C. performed viral injections and bulk fluorescence tracing. D.F.A., A.A.K., and A.M.Z. supervised the project. Y.C., X.C., A.M.Z., A.A.K., and D.F.A. wrote the manuscript with input from all authors.

DECLARATION OF INTERESTS

A.M.Z. is a founder and equity owner of Cajal Neuroscience and a member of its scientific advisory board.

Received: October 19, 2021

Revised: July 22, 2022

Accepted: September 28, 2022

Published: October 27, 2022

REFERENCES

- Armeodo, E.M., Penikis, K.B., Rabinowitz, N., Licata, A., Cichy, A., Zhang, J., Bozza, T., and Rinberg, D. (2018). Stimulus dependent diversity and stereotypy in the output of an olfactory functional unit. *Nat. Commun.* 9, 1347. <https://doi.org/10.1038/s41467-018-03837-1>.
- Babadi, B., and Sompolinsky, H. (2014). Sparseness and expansion in sensory representations. *Neuron* 83, 1213–1226. <https://doi.org/10.1016/j.neuron.2014.07.035>.
- Barlow, H.B., and Hill, R.M. (1963). Selective sensitivity to direction of movement in ganglion cells of the rabbit retina. *Science* 139, 412–414. <https://doi.org/10.1126/science.139.3553.412>.
- Barnes, D.C., Hofacer, R.D., Zaman, A.R., Rennaker, R.L., and Wilson, D.A. (2008). Olfactory perceptual stability and discrimination. *Nat. Neurosci.* 11, 1378–1380. <https://doi.org/10.1038/nn.2217>.
- Basu, J., and Siegelbaum, S.A. (2015). The Corticohippocampal Circuit, Synaptic Plasticity, and Memory. *Cold Spring Harb. Perspect. Biol.* 7, a021733. <https://doi.org/10.1101/cshperspect.a021733>.
- Bekkers, J.M., and Suzuki, N. (2013). Neurons and circuits for odor processing in the piriform cortex. *Trends Neurosci.* 36, 429–438. <https://doi.org/10.1016/j.tins.2013.04.005>.
- Blockus, H., and Polleux, F. (2021). Developmental mechanisms underlying circuit wiring: Novel insights and challenges ahead. *Curr. Opin. Neurobiol.* 66, 205–211. <https://doi.org/10.1016/j.conb.2020.12.013>.
- Blondel, V.D., Guillaume, J.-L., Lambiotte, R., and Lefebvre, E. (2008). Fast unfolding of communities in large networks. *J. Stat. Mech. Theory Exp.* 2008, P10008. <https://doi.org/10.1088/1742-5468/2008/10/P10008>.
- Bolding, K.A., and Franks, K.M. (2018). Recurrent cortical circuits implement concentration-invariant odor coding. *Science* 361, eaat6904. <https://doi.org/10.1126/science.aat6904>.
- Brewer, A.A., and Barton, B. (2016). Maps of the Auditory Cortex. *Annu. Rev. Neurosci.* 39, 385–407. <https://doi.org/10.1146/annurev-neuro-070815-014045>.
- Burton, S.D., and Urban, N.N. (2014). Greater excitability and firing irregularity of tufted cells underlies distinct afferent-evoked activity of olfactory bulb mitral and tufted cells. *J. Physiol.* 592, 2097–2118. <https://doi.org/10.1113/jphysiol.2013.269886>.
- Calu, D.J., Roesch, M.R., Stalnaker, T.A., and Schoenbaum, G. (2007). Associative Encoding in Posterior Piriform Cortex during Odor Discrimination and Reversal Learning. *Cereb. Cortex* 17, 1342–1349. <https://doi.org/10.1093/cercor/bhl045>.
- Cang, J., and Feldheim, D.A. (2013). Developmental Mechanisms of Topographic Map Formation and Alignment. *Annu. Rev. Neurosci.* 36, 51–77. <https://doi.org/10.1146/annurev-neuro-062012-170341>.
- Caron, S.J.C., Ruta, V., Abbott, L.F., and Axel, R. (2013). Random convergence of olfactory inputs in the *Drosophila* mushroom body. *Nature* 497, 113–117. <https://doi.org/10.1038/nature12063>.
- Chae, H., Kepple, D., Bast, W.G., Murthy, V.N., Koulakov, A., and Albeanu, D.F. (2018). Mosaic representations of odors in the input and output layers of the mouse olfactory bulb. *BioRxiv* 259945. <https://doi.org/10.1101/259945>.
- Chae, H., Banerjee, A., and Albeanu, D.F. (2021). A Non-canonical Feedforward Pathway for Computing Odor Identity. *bioRxiv* 2020. 09.28.317248.
- Chen, C.-F.F., Zou, D.-J., Altomare, C.G., Xu, L., Greer, C.A., and Firestein, S.J. (2014). Nonsensory target-dependent organization of piriform cortex. *Proc. Natl. Acad. Sci. USA* 111, 16931–16936. <https://doi.org/10.1073/pnas.1411266111>.
- Chen, X., Sun, Y.-C., Zhan, H., Kebschull, J.M., Fischer, S., Matho, K., Huang, Z.J., Gillis, J., and Zador, A.M. (2019). High-Throughput Mapping of Long-Range Neuronal Projection Using In Situ Sequencing. *Cell* 179, 772–786.e19. <https://doi.org/10.1016/j.cell.2019.09.023>.
- Chklovskii, D.B., and Koulakov, A.A. (2004). Maps in the brain: what can we learn from them? *Annu. Rev. Neurosci.* 27, 369–392. <https://doi.org/10.1146/annurev.neuro.27.070203.144226>.
- Chklovskii, D.B., Schikorski, T., and Stevens, C.F. (2002). Wiring Optimization in Cortical Circuits. *Neuron* 34, 341–347. [https://doi.org/10.1016/S0896-6273\(02\)00679-7](https://doi.org/10.1016/S0896-6273(02)00679-7).
- Choi, G., Stettler, D., Kallman, B., Bhaskar, S., Fleischmann, A., and Axel, R. (2011). Driving opposing behaviors with ensembles of piriform neurons. *Cell* 146, 1004–1015. <https://doi.org/10.1016/j.cell.2011.07.041>.
- Dasgupta, S., Stevens, C.F., and Navlakha, S. (2017). A neural algorithm for a fundamental computing problem. *Science* 358, 793–796. <https://doi.org/10.1126/science.aam9868>.
- Datiche, F., Litaudon, P., and Cattarelli, M. (1996). Intrinsic association fiber system of the piriform cortex: A quantitative study based on a cholera toxin B subunit tracing in the rat. *J. Comp. Neurol.* 376, 265–277. [https://doi.org/10.1002/\(SICI\)1096-9861\(19961209\)376:2<265::AID-CNE8>3.0.CO;2-1](https://doi.org/10.1002/(SICI)1096-9861(19961209)376:2<265::AID-CNE8>3.0.CO;2-1).
- Dhande, O.S., Stafford, B.K., Lim, J.-H.A., and Huberman, A.D. (2015). Contributions of Retinal Ganglion Cells to Subcortical Visual Processing and Behaviors. *Annu. Rev. Vis. Sci.* 1, 291–328. <https://doi.org/10.1146/annurev-vision-082114-035502>.
- Dhawale, A.K., Hagiwara, A., Bhalla, U.S., Murthy, V.N., and Albeanu, D.F. (2010). Non-redundant odor coding by sister mitral cells revealed by light addressable glomeruli in the mouse. *Nat. Neurosci.* 13, 1404–1412. <https://doi.org/10.1038/nn.2673>.
- Dijkerman, H.C., and de Haan, E.H.F. (2007). Somatosensory processes subserving perception and action. *Behav. Brain Sci.* 30, 189–201. discussion 201–239. <https://doi.org/10.1017/S0140525X07000392>.
- Diodato, A., Ruinart de Brimont, M., Yim, Y.S., Derian, N., Perrin, S., Pouch, J., Klatzmann, D., Garel, S., Choi, G.B., and Fleischmann, A. (2016). Molecular signatures of neural connectivity in the olfactory cortex. *Nat. Commun.* 7, 12238. <https://doi.org/10.1038/ncomms12238>.
- Eichler, K., Li, F., Litwin-Kumar, A., Park, Y., Andrade, I., Schneider-Mizell, C.M., Saumweber, T., Huser, A., Eschbach, C., Gerber, B., et al. (2017). The complete connectome of a learning and memory centre in an insect brain. *Nature* 548, 175–182. <https://doi.org/10.1038/nature23455>.
- Esquivelzeta Rabell, J., Mutlu, K., Noutel, J., Martin del Olmo, P., and Haesler, S. (2017). Spontaneous Rapid Odor Source Localization Behavior Requires

- Interhemispheric Communication. *Curr. Biol.* 27, 1542–1548.e4. <https://doi.org/10.1016/j.cub.2017.04.027>.
- Eyre, M.D., Antal, M., and Nusser, Z. (2008). Distinct deep short-axon cell subtypes of the main olfactory bulb provide novel intrabulbar and extrabulbar GABAergic connections. *J. Neurosci. Off. J. Soc. Neurosci.* 28, 8217–8229. <https://doi.org/10.1523/JNEUROSCI.2490-08.2008>.
- Fantana, A.L., Soucy, E.R., and Meister, M. (2008). Rat olfactory bulb mitral cells receive sparse glomerular inputs. *Neuron* 59, 802–814. <https://doi.org/10.1016/j.neuron.2008.07.039>.
- Field, G.D., and Chichilnisky, E.J. (2007). Information Processing in the Primate Retina: Circuitry and Coding. *Annu. Rev. Neurosci.* 30, 1–30. <https://doi.org/10.1146/annurev.neuro.30.051606.094252>.
- Franks, K., Russo, M., Sosulski, D., Mulligan, A., Siegelbaum, S., and Axel, R. (2011). Recurrent circuitry dynamically shapes the activation of piriform cortex. *Neuron* 72, 49–56. <https://doi.org/10.1016/j.neuron.2011.08.020>.
- Fukunaga, I., Beming, M., Kollo, M., Schmaltz, A., and Schaefer, A. (2012). Two distinct channels of olfactory bulb output. *Neuron* 75, 320–329. <https://doi.org/10.1016/j.neuron.2012.05.017>.
- Fürth, D., Vaissière, T., Tzortzi, O., Xuan, Y., Märtin, A., Lazaridis, I., Spigolon, G., Fisone, G., Tomer, R., Deisseroth, K., et al. (2018). An interactive framework for whole-brain maps at cellular resolution. *Nat. Neurosci.* 21, 139–149. <https://doi.org/10.1038/s41593-017-0027-7>.
- Gadziola, M.A., and Wesson, D.W. (2016). The Neural Representation of Goal-Directed Actions and Outcomes in the Ventral Striatum's Olfactory Tubercle. *J. Neurosci. Off. J. Soc. Neurosci.* 36, 548–560. <https://doi.org/10.1523/JNEUROSCI.3328-15.2016>.
- Geramita, M., and Urban, N.N. (2017). Differences in Glomerular-Layer-Mediated Feedforward Inhibition onto Mitral and Tufted Cells Lead to Distinct Modes of Intensity Coding. *J. Neurosci. Off. J. Soc. Neurosci.* 37, 1428–1438. <https://doi.org/10.1523/JNEUROSCI.2245-16.2016>.
- Geramita, M.A., Burton, S.D., and Urban, N.N. (2016). Distinct lateral inhibitory circuits drive parallel processing of sensory information in the mammalian olfactory bulb. *Elife* 5, e16039. <https://doi.org/10.7554/eLife.16039>.
- Ghosh, S., Larson, S.D., Hefzi, H., Marnoy, Z., Cutforth, T., Dokka, K., and Baldwin, K.K. (2011). Sensory maps in the olfactory cortex defined by long-range viral tracing of single neurons. *Nature* 472, 217–220. <https://doi.org/10.1038/nature09945>.
- Giessel, A.J., and Datta, S.R. (2014). Olfactory maps, circuits and computations. *Curr. Opin. Neurobiol.* 24, 120–132. <https://doi.org/10.1016/j.conb.2013.09.010>.
- Gire, D.H., Franks, K.M., Zak, J.D., Tanaka, K.F., Whitesell, J.D., Mulligan, A.A., Hen, R., and Schoppa, N.E. (2012). Mitral cells in the olfactory bulb are mainly excited through a multistep signaling path. *J. Neurosci. Off. J. Soc. Neurosci.* 32, 2964–2975. <https://doi.org/10.1523/JNEUROSCI.5580-11.2012>.
- Goodale, M.A., and Milner, A. (1992). Separate visual pathways for perception and action. *Trends Neurosci.* 15, 20–25. [https://doi.org/10.1016/0166-2236\(92\)90344-8](https://doi.org/10.1016/0166-2236(92)90344-8).
- Gottfried, J.A. (2010). Central mechanisms of odour object perception. *Nat. Rev. Neurosci.* 11, 628–641. <https://doi.org/10.1038/nrn2883>.
- Gruntman, E., and Turner, G.C. (2013). Integration of the olfactory code across dendritic claws of single mushroom body neurons. *Nat. Neurosci.* 16, 1821–1829. <https://doi.org/10.1038/nn.3547>.
- Gschwend, O., Abraham, N.M., Lagier, S., Begnaud, F., Rodriguez, I., and Carleton, A. (2015). Neuronal pattern separation in the olfactory bulb improves odor discrimination learning. *Nat. Neurosci.* 18, 1474–1482. <https://doi.org/10.1038/nn.4089>.
- Haberly, L.B. (1985). Neuronal circuitry in olfactory cortex: Anatomy and functional implications. *Chem. Senses* 10, 219–238. <https://doi.org/10.1093/chemse/10.2.219>.
- Haberly, L.B. (2001). Parallel-distributed processing in olfactory cortex: new insights from morphological and physiological analysis of neuronal circuitry. *Chem. Senses* 26, 551–576. <https://doi.org/10.1093/chemse/26.5.551>.
- Haberly, L.B., and Price, J.L. (1977). The axonal projection patterns of the mitral and tufted cells of the olfactory bulb in the rat. *Brain Res.* 129, 152–157. [https://doi.org/10.1016/0006-8993\(77\)90978-7](https://doi.org/10.1016/0006-8993(77)90978-7).
- Haberly, L.B., and Price, J.L. (1978). Association and commissural fiber systems of the olfactory cortex of the rat. I. Systems originating in the piriform cortex and adjacent areas. *J. Comp. Neurol.* 178, 711–740. <https://doi.org/10.1002/cne.901780408>.
- Hagiwara, A., Pal, S.K., Sato, T.F., Wienisch, M., and Murthy, V.N. (2012). Optophysiological analysis of associational circuits in the olfactory cortex. *Front. Neural Circuits* 6, 18. <https://doi.org/10.3389/fncir.2012.00018>.
- Han, Y., Kebschull, J.M., Campbell, R.A.A., Cowan, D., Imhof, F., Zador, A.M., and Mrsic-Flogel, T.D. (2018). The logic of single-cell projections from visual cortex. *Nature* 556, 51–56. <https://doi.org/10.1038/nature26159>.
- Harding-Forrester, S., and Feldman, D.E. (2018). Somatosensory maps. *Handb. Clin. Neurol.* 151, 73–102. <https://doi.org/10.1016/B978-0-444-63622-5.00004-8>.
- He, K., Zhang, X., Ren, S., and Sun, J. (2016). Deep Residual Learning for Image Recognition. 2016 IEEE Conference on Computer Vision and Pattern Recognition (CVPR) (Las Vegas, NV, USA: IEEE), pp. 770–778.
- Hiratani, N., and Latham, P.E. (2020a). Developmental and Evolutionary Constraints on Olfactory Circuit Selection.
- Hiratani, N., and Latham, P.E. (2020b). Rapid Bayesian learning in the mammalian olfactory system. *Nat. Commun.* 11, 3845. <https://doi.org/10.1038/s41467-020-17490-0>.
- Huang, L., Kebschull, J.M., Fürth, D., Musall, S., Kaufman, M.T., Churchland, A.K., and Zador, A.M. (2020). BRICseq Bridges Brain-wide Interregional Connectivity to Neural Activity and Gene Expression in Single Animals. *Cell* 182, 177–188.e27. <https://doi.org/10.1016/j.cell.2020.05.029>.
- Igarashi, K.M., Ieki, N., An, M., Yamaguchi, Y., Nagayama, S., Kobayakawa, K., Kobayakawa, R., Tanifuji, M., Sakano, H., Chen, W.R., and Mori, K. (2012). Parallel mitral and tufted cell pathways route distinct odor information to different targets in the olfactory cortex. *J. Neurosci. Off. J. Soc. Neurosci.* 32, 7970–7985. <https://doi.org/10.1523/JNEUROSCI.0154-12.2012>.
- Johnson, D.M.G., Illig, K.R., Behan, M., and Haberly, L.B. (2000). New Features of Connectivity in Piriform Cortex Visualized by Intracellular Injection of Pyramidal Cells Suggest that “Primary” Olfactory Cortex Functions Like “Association” Cortex in Other Sensory Systems. *J. Neurosci.* 20, 6974–6982. <https://doi.org/10.1523/JNEUROSCI.20-18-06974.2000>.
- Jordan, R., Fukunaga, I., Kollo, M., and Schaefer, A.T. (2018). Active Sampling State Dynamically Enhances Olfactory Bulb Odor Representation. *Neuron* 98, 1214–1228.e5. <https://doi.org/10.1016/j.neuron.2018.05.016>.
- Kaas, J.H. (1997). Topographic maps are fundamental to sensory processing. *Brain Res. Bull.* 44, 107–112. [https://doi.org/10.1016/s0361-9230\(97\)00094-4](https://doi.org/10.1016/s0361-9230(97)00094-4).
- Kadohisa, M., and Wilson, D.A. (2006). Separate encoding of identity and similarity of complex familiar odors in piriform cortex. *Proc. Natl. Acad. Sci.* 103, 15206–15211. <https://doi.org/10.1073/pnas.0604313103>.
- Kapoor, V., Provost, A.C., Agarwal, P., and Murthy, V.N. (2016). Activation of raphe nuclei triggers rapid and distinct effects on parallel olfactory bulb output channels. *Nat. Neurosci.* 19, 271–282. <https://doi.org/10.1038/nn.4219>.
- Kebschull, J.M., Garcia da Silva, P., Reid, A.P., Peikon, I.D., Albeanu, D.F., and Zador, A.M. (2016). High-Throughput Mapping of Single-Neuron Projections by Sequencing of Barcoded RNA. *Neuron* 91, 975–987. <https://doi.org/10.1016/j.neuron.2016.07.036>.
- Kikuta, S., Sato, K., Kashiwadani, H., Tsunoda, K., Yamasoba, T., and Mori, K. (2010). Neurons in the anterior olfactory nucleus pars externa detect right or left localization of odor sources. *Proc. Natl. Acad. Sci.* 107, 12363–12368. <https://doi.org/10.1073/pnas.1003999107>.
- Kikuta, S., Fletcher, M., Homma, R., Yamasoba, T., and Nagayama, S. (2013). Odorant response properties of individual neurons in an olfactory glomerular module. *Neuron* 77, 1122–1135. <https://doi.org/10.1016/j.neuron.2013.01.022>.
- Klyachko, V.A., and Stevens, C.F. (2003). Connectivity optimization and the positioning of cortical areas. *Proc. Natl. Acad. Sci.* 100, 7937–7941. <https://doi.org/10.1073/pnas.0932745100>.

- Knudsen, E.I., Lac, S., and Esterly, S.D. (1987). Computational maps in the brain. *Annu. Rev. Neurosci.* *10*, 41–65. <https://doi.org/10.1146/annurev.ne.10.030187.000353>.
- Kosaka, T., and Kosaka, K. (2007). Heterogeneity of nitric oxide synthase-containing neurons in the mouse main olfactory bulb. *Neurosci. Res.* *57*, 165–178. <https://doi.org/10.1016/j.neures.2006.10.005>.
- Krishnamurthy, K., Hermundstad, A.M., Mora, T., Walczak, A.M., and Balasubramanian, V. (2017). Disorder and the Neural Representation of Complex Odors: Smelling in the Real World. *bioRxiv*, 160382. <https://doi.org/10.1101/160382>.
- Large, A.M., Vogler, N.W., Canto-Bustos, M., Friason, F.K., Schick, P., and Oswald, A.-M.M. (2018). Differential inhibition of pyramidal cells and inhibitory interneurons along the rostrocaudal axis of anterior piriform cortex. *Proc. Natl. Acad. Sci.* *115*, E8067–E8076. <https://doi.org/10.1073/pnas.1802428115>.
- Ledoux, J. (1998). *The Emotional Brain: The Mysterious Underpinnings of Emotional Life* (Simon and Schuster).
- LeDoux, J.E., Farb, C.R., and Romanski, L.M. (1991). Overlapping projections to the amygdala and striatum from auditory processing areas of the thalamus and cortex. *Neurosci. Lett.* *134*, 139–144. [https://doi.org/10.1016/0304-3940\(91\)90526-y](https://doi.org/10.1016/0304-3940(91)90526-y).
- Lettvin, J., Maturana, H., McCulloch, W., and Pitts, W. (1959). What the Frog's Eye Tells the Frog's Brain. *Proc. IRE* *47*, 1940–1951. <https://doi.org/10.1109/JRPROC.1959.287207>.
- Li, F., Lindsey, J.W., Marin, E.C., Otto, N., Dreher, M., Dempsey, G., Stark, I., Bates, A.S., Pleijzier, M.W., Schlegel, P., et al. (2020). The connectome of the adult *Drosophila* mushroom body provides insights into function. *Elife* *9*, e62576. <https://doi.org/10.7554/eLife.62576>.
- Li, S.-J., Vaughan, A., Sturgill, J.F., and Kepecs, A. (2018). A Viral Receptor Complementation Strategy to Overcome CAV-2 Tropism for Efficient Retrograde Targeting of Neurons. *Neuron* *98*, 905–917.e5. <https://doi.org/10.1016/j.neuron.2018.05.028>.
- Li, W., Luxenberg, E., Parrish, T., and Gottfried, J.A. (2006). Learning to smell the roses: experience-dependent neural plasticity in human piriform and orbitofrontal cortices. *Neuron* *52*, 1097–1108. <https://doi.org/10.1016/j.neuron.2006.10.026>.
- Litwin-Kumar, A., Harris, K.D., Axel, R., Sompolinsky, H., and Abbott, L.F. (2017). Optimal Degrees of Synaptic Connectivity. *Neuron* *93*, 1153–1164.e7. <https://doi.org/10.1016/j.neuron.2017.01.030>.
- Luna, V.M., and Pettit, D.L. (2010). Asymmetric rostro-caudal inhibition in the primary olfactory cortex. *Nat. Neurosci.* *13*, 533–535. <https://doi.org/10.1038/nn.2524>.
- Luskin, M.B., and Price, J.L. (1982). The distribution of axon collaterals from the olfactory bulb and the nucleus of the horizontal limb of the diagonal band to the olfactory cortex, demonstrated by double retrograde labeling techniques. *J. Comp. Neurol.* *209*, 249–263. <https://doi.org/10.1002/cne.902090304>.
- Markov, N.T., Misery, P., Falchier, A., Lamy, C., Vezoli, J., Quilodran, R., Gariel, M.A., Giroud, P., Ercsey-Ravasz, M., Pilaz, L.J., Huissoud, C., Barone, P., Dehay, C., Toroczkai, Z., Van Essen, D.C., Kennedy, H., and Knoblauch, K. (2011). Weight consistency specifies regularities of macaque cortical networks. *Cereb. Cortex N. Y. N* *1991* *21*, 1254–1272. <https://doi.org/10.1093/cercor/bhq201>.
- Mazo, C., Grimaud, J., Shima, Y., Murthy, V.N., and Lau, C.G. (2017). Distinct projection patterns of different classes of layer 2 principal neurons in the olfactory cortex. *Sci. Rep.* *7*, 8282. <https://doi.org/10.1038/s41598-017-08331-0>.
- Millman, D.J., and Murthy, V.N. (2020). Rapid Learning of Odor-Value Association in the Olfactory Striatum. *J. Neurosci.* *40*, 4335–4347. <https://doi.org/10.1523/JNEUROSCI.2604-19.2020>.
- Mishkin, M., and Ungerleider, L.G. (1982). Contribution of striate inputs to the visuospatial functions of parieto-preoccipital cortex in monkeys. *Behav. Brain Res.* *6*, 57–77. [https://doi.org/10.1016/0166-4328\(82\)90081-x](https://doi.org/10.1016/0166-4328(82)90081-x).
- Miura, K., Mainen, Z., and Uchida, N. (2012). Odor representations in olfactory cortex: distributed rate coding and decorrelated population activity. *Neuron* *74*, 1087–1098. <https://doi.org/10.1016/j.neuron.2012.04.021>.
- Miyamichi, K., Amat, F., Moussavi, F., Wang, C., Wickersham, I., Wall, N.R., Taniguchi, H., Tasic, B., Huang, Z.J., He, Z., et al. (2011). Cortical representations of olfactory input by trans-synaptic tracing. *Nature* *472*, 191–196. <https://doi.org/10.1038/nature09714>.
- Mori, K., Kishi, K., and Ojima, H. (1983). Distribution of dendrites of mitral, displaced mitral, tufted, and granule cells in the rabbit olfactory bulb. *J. Comp. Neurol.* *219*, 339–355. <https://doi.org/10.1002/cne.902190308>.
- Münch, T.A., da Silveira, R.A., Siegert, S., Viney, T.J., Awatramani, G.B., and Roska, B. (2009). Approach sensitivity in the retina processed by a multifunctional neural circuit. *Nat. Neurosci.* *12*, 1308–1316. <https://doi.org/10.1038/nn.2389>.
- Muñoz-Castañeda, R., Zingg, B., Matho, K.S., Chen, X., Wang, Q., Foster, N.N., Li, A., Narasimhan, A., Hirokawa, K.E., Huo, B., et al. (2021). Cellular anatomy of the mouse primary motor cortex. *Nature* *598*, 159–166. <https://doi.org/10.1038/s41586-021-03970-w>.
- Nagayama, S., Enever, A., Fletcher, M.L., Masurkar, A.V., Igarashi, K.M., Mori, K., and Chen, W.R. (2010). Differential axonal projection of mitral and tufted cells in the mouse main olfactory system. *Front. Neural Circuits* *4*, 120. <https://doi.org/10.3389/fncir.2010.00120>.
- Nauhaus, I., and Nielsen, K.J. (2014). Building maps from maps in primary visual cortex. *Curr. Opin. Neurobiol.* *24*, 1–6. <https://doi.org/10.1016/j.conb.2013.08.007>.
- Oettl, L.-L., Ravi, N., Schneider, M., Scheller, M., Schneider, P., Mitre, M., da Silva Gouveia, M., Froemke, R., Chao, M., Young, W., et al. (2016). Oxytocin Enhances Social Recognition by Modulating Cortical Control of Early Olfactory Processing. *Neuron* *90*, 609–621. <https://doi.org/10.1016/j.neuron.2016.03.033>.
- Oettl, L.-L., Scheller, M., Filosa, C., Wieland, S., Haag, F., Loeb, C., Durstewitz, D., Shusterman, R., Russo, E., and Kelsch, W. (2020). Phasic dopamine reinforces distinct striatal stimulus encoding in the olfactory tubercle driving dopaminergic reward prediction. *Nat. Commun.* *11*, 3460. <https://doi.org/10.1038/s41467-020-17257-7>.
- Ojima, H., Mori, K., and Kishi, K. (1984). The trajectory of mitral cell axons in the rabbit olfactory cortex revealed by intracellular HRP injection. *J. Comp. Neurol.* *230*, 77–87. <https://doi.org/10.1002/cne.902300107>.
- Olveczky, B.P., Baccus, S.A., and Meister, M. (2003). Segregation of object and background motion in the retina. *Nature* *423*, 401–408. <https://doi.org/10.1038/nature01652>.
- Otazu, G., Chae, H., Davis, M., and Albeanu, D. (2015). Cortical Feedback Decorrelates Olfactory Bulb Output in Awake Mice. *Neuron* *86*, 1461–1477. <https://doi.org/10.1016/j.neuron.2015.05.023>.
- Peng, H., Xie, P., Liu, L., Kuang, X., Wang, Y., Qu, L., Gong, H., Jiang, S., Li, A., Ruan, Z., et al. (2020). Brain-wide single neuron reconstruction reveals morphological diversity in molecularly defined striatal, thalamic, cortical and claustral neuron types. *BioRxiv* 675280. <https://doi.org/10.1101/675280>.
- Poo, C., Agarwal, G., Bonacchi, N., and Mainen, Z.F. (2022). Spatial maps in piriform cortex during olfactory navigation. *Nature* *601*, 595–599. <https://doi.org/10.1038/s41586-021-04242-3>.
- Price, J.L. (1973). An autoradiographic study of complementary laminar patterns of termination of afferent fibers to the olfactory cortex. *J. Comp. Neurol.* *150*, 87–108. <https://doi.org/10.1002/cne.901500105>.
- Rauschecker, J.P., and Romanski, L.M. (2011). *Auditory Cortical Organization: Evidence for Functional Streams*. In *The Auditory Cortex*, J.A. Winer and C.E. Schreiner, eds. (Boston, MA: Springer US), pp. 99–116.
- Rennaker, R.L., Chen, C.-F.F., Ruyle, A.M., Sloan, A.M., and Wilson, D.A. (2007). Spatial and Temporal Distribution of Odorant-Evoked Activity in the Piriform Cortex. *J. Neurosci.* *27*, 1534–1542. <https://doi.org/10.1523/JNEUROSCI.4072-06.2007>.
- Roesch, M.R., Stalnaker, T.A., and Schoenbaum, G. (2006). Associative Encoding in Anterior Piriform Cortex versus Orbitofrontal Cortex during Odor

- Discrimination and Reversal Learning. *Cereb. Cortex N. Y. N* 1991 17, 643–652. <https://doi.org/10.1093/cercor/bhk009>.
- Root, C.M., Denny, C.A., Hen, R., and Axel, R. (2014). The participation of cortical amygdala in innate, odour-driven behaviour. *Nature* 515, 269–273. <https://doi.org/10.1038/nature13897>.
- Russo, M.J., Franks, K.M., Oghaz, R., Axel, R., and Siegelbaum, S.A. (2020). Synaptic organization of anterior olfactory nucleus inputs to piriform cortex. *J. Neurosci.* 40, 9414–9425. <https://doi.org/10.1523/JNEUROSCI.0965-20.2020>.
- Sanders, H., Kolterman, B.E., Shusterman, R., Rinberg, D., Koulakov, A., and Lisman, J. (2014). A network that performs brute-force conversion of a temporal sequence to a spatial pattern: relevance to odor recognition. *Front. Comput. Neurosci.* 8, 108. <https://doi.org/10.3389/fncom.2014.00108>.
- Sanes, J.R., and Masland, R.H. (2015). The types of retinal ganglion cells: current status and implications for neuronal classification. *Annu. Rev. Neurosci.* 38, 221–246. <https://doi.org/10.1146/annurev-neuro-071714-034120>.
- Schaffer, E.S., Stettler, D.D., Kato, D., Choi, G.B., Axel, R., and Abbott, L.F. (2018). Odor Perception on the Two Sides of the Brain: Consistency Despite Randomness. *Neuron* 98, 736–742.e3. <https://doi.org/10.1016/j.neuron.2018.04.004>.
- Schindelin, J., Arganda-Carreras, I., Frise, E., Kaynig, V., Longair, M., Pietzsch, T., Preibisch, S., Rueden, C., Saalfeld, S., Schmid, B., et al. (2012). Fiji: an open-source platform for biological-image analysis. *Nat. Methods* 9, 676–682. <https://doi.org/10.1038/nmeth.2019>.
- Schneider, G.E. (1969). Two Visual Systems. *Science* 163, 895–902. <https://doi.org/10.1126/science.163.3870.895>.
- Schneider, C.A., Rasband, W.S., and Eliceiri, K.W. (2012). NIH Image to ImageJ: 25 years of image analysis. *Nat Methods* 9, 671–675. <https://doi.org/10.1038/nmeth.2089>.
- Schoonover, C.E., Ohashi, S.N., Axel, R., and Fink, A.J.P. (2021). Representational drift in primary olfactory cortex. *Nature* 594, 541–546. <https://doi.org/10.1038/s41586-021-03628-7>.
- Schwarz, D., Kollo, M., Bosch, C., Feinauer, C., Whiteley, I., Margrie, T.W., Cutforth, T., and Schaefer, A.T. (2018). Architecture of a mammalian glomerular domain revealed by novel volume electroporation using nanoengineered microelectrodes. *Nat. Commun.* 9, 183. <https://doi.org/10.1038/s41467-017-02560-7>.
- Scott, J.W., McBride, R.L., and Schneider, S.P. (1980). The organization of projections from the olfactory bulb to the piriform cortex and olfactory tubercle in the rat. *J. Comp. Neurol.* 194, 519–534. <https://doi.org/10.1002/cne.901940304>.
- Skeen, L.C., and Hall, W.C. (1977). Efferent projections of the main and the accessory olfactory bulb in the tree shrew (*Tupaia glis*). *J. Comp. Neurol.* 172, 1–35. <https://doi.org/10.1002/cne.901720102>.
- Song, S., Sjöström, P.J., Reigl, M., Nelson, S., and Chklovskii, D.B. (2005). Highly nonrandom features of synaptic connectivity in local cortical circuits. *PLoS Biol.* 3, e68. <https://doi.org/10.1371/journal.pbio.0030068>.
- Sosulski, D.L., Bloom, M.L., Cutforth, T., Axel, R., and Datta, S.R. (2011). Distinct representations of olfactory information in different cortical centres. *Nature* 472, 213–216. <https://doi.org/10.1038/nature09868>.
- Srinivasan, S., and Stevens, C.F. (2019). Scaling Principles of Distributed Circuits. *Curr. Biol.* 29, 2533–2540.e7. <https://doi.org/10.1016/j.cub.2019.06.046>.
- Stern, M., Bolding, K.A., Abbott, L.F., and Franks, K.M. (2018). A transformation from temporal to ensemble coding in a model of piriform cortex. *Elife* 7, e34831. <https://doi.org/10.7554/eLife.34831>.
- Stettler, D.D., and Axel, R. (2009). Representations of odor in the piriform cortex. *Neuron* 63, 854–864. <https://doi.org/10.1016/j.neuron.2009.09.005>.
- Stevens, C.F. (2007). 1.17 - Principles of Brain Scaling. In *Evolution of Nervous Systems*, J.H. Kaas, ed. (Oxford: Academic Press), pp. 273–282.
- Stevens, C.F. (2015). What the fly's nose tells the fly's brain. *Proc. Natl. Acad. Sci.* 112, 9460–9465. <https://doi.org/10.1073/pnas.1510103112>.
- van Strien, N.M., Cappaert, N.L.M., and Witter, M.P. (2009). The anatomy of memory: an interactive overview of the parahippocampal-hippocampal network. *Nat. Rev. Neurosci.* 10, 272–282. <https://doi.org/10.1038/nrn2614>.
- Sun, Y.-C., Chen, X., Fischer, S., Lu, S., Gillis, J., and Zador, A.M. (2020). Integrating barcoded neuroanatomy with spatial transcriptional profiling reveals cadherin correlates of projections shared across the cortex. *bioRxiv*. 2020.08.25.266460. <https://doi.org/10.1101/2020.08.25.266460>.
- Sun, Y.-C., Chen, X., Fischer, S., Lu, S., Zhan, H., Gillis, J., and Zador, A.M. (2021). Integrating barcoded neuroanatomy with spatial transcriptional profiling enables identification of gene correlates of projections. *Nat. Neurosci.* 24, 873–885. <https://doi.org/10.1038/s41593-021-00842-4>.
- Tikidji-Hamburyan, R.A., El-Ghazawi, T.A., and Triplett, J.W. (2016). Novel Models of Visual Topographic Map Alignment in the Superior Colliculus. *PLoS Comput. Biol.* 12, e1005315. <https://doi.org/10.1371/journal.pcbi.1005315>.
- Treves, A., and Rolls, E.T. (1991). What determines the capacity of autoassociative memories in the brain? *Netw. Comput. Neural Syst.* 2, 371–397. https://doi.org/10.1088/0954-898X_2_4_004.
- Tsao, A., Sugar, J., Lu, L., Wang, C., Knierim, J.J., Moser, M.-B., and Moser, E.I. (2018). Integrating time from experience in the lateral entorhinal cortex. *Nature* 567, 57–62. <https://doi.org/10.1038/s41586-018-0459-6>.
- Uchida, N., Poo, C., and Haddad, R. (2014a). Coding and transformations in the olfactory system. *Annu. Rev. Neurosci.* 37, 363–385. <https://doi.org/10.1146/annurev-neuro-071013-013941>.
- Uchida, N., Poo, C., and Haddad, R. (2014b). Coding and transformations in the olfactory system. *Annu. Rev. Neurosci.* 37, 363–385. <https://doi.org/10.1146/annurev-neuro-071013-013941>.
- Wang, Q., and Burkhalter, A. (2013). Stream-related preferences of inputs to the superior colliculus from areas of dorsal and ventral streams of mouse visual cortex. *J. Neurosci. Off. J. Soc. Neurosci.* 33, 1696–1705. <https://doi.org/10.1523/JNEUROSCI.3067-12.2013>.
- Wang, X.-J., and Kennedy, H. (2016). Brain structure and dynamics across scales: In search of rules. *Curr. Opin. Neurobiol.* 37, 92–98. <https://doi.org/10.1016/j.conb.2015.12.010>.
- Wang, C., Chen, X., Lee, H., Deshmukh, S.S., Yoganarasimha, D., Savelli, F., and Knierim, J.J. (2018). Egocentric coding of external items in the lateral entorhinal cortex. *Science* 362, 945–949. <https://doi.org/10.1126/science.aau4940>.
- Wang, C.Y., Liu, Z., Ng, Y.H., and Südhof, T.C. (2020a). A Synaptic Circuit Required for Acquisition but Not Recall of Social Transmission of Food Preference. *Neuron* 107, 144–157.e4. <https://doi.org/10.1016/j.neuron.2020.04.004>.
- Wang, L., Zhang, Z., Chen, J., Manyande, A., Haddad, R., Liu, Q., and Xu, F. (2020b). Cell-Type-Specific Whole-Brain Direct Inputs to the Anterior and Posterior Piriform Cortex. *Front. Neural Circuits* 14, 4. <https://doi.org/10.3389/fncir.2020.00004>.
- Wegner, F. (1980). Inverse participation ratio in $2+\epsilon$ dimensions. *Z. Für Phys. B Condens. Matter* 36, 209–214. <https://doi.org/10.1007/BF01325284>.
- Willmore, B., and Tolhurst, D.J. (2001). Characterizing the sparseness of neural codes. *Netw. Bristol Engl.* 12, 255–270. <https://doi.org/10.1080/net.12.3.255.270>.
- Wilson, D., and Sullivan, R. (2011). Cortical processing of odor objects. *Neuron* 72, 506–519. <https://doi.org/10.1016/j.neuron.2011.10.027>.
- Wilson, C.D., Serrano, G.O., Koulakov, A.A., and Rinberg, D. (2017). A primacy code for odor identity. *Nat. Commun.* 8, 1477. <https://doi.org/10.1038/s41467-017-01432-4>.
- Winnubst, J., Bas, E., Ferreira, T.A., Wu, Z., Economo, M.N., Edson, P., Arthur, B.J., Bruns, C., Rokicki, K., Schauder, D., et al. (2019). Reconstruction of 1, 000 Projection Neurons Reveals New Cell Types and Organization of Long-Range Connectivity in the Mouse Brain. *Cell* 179, 268–281.e13. <https://doi.org/10.1016/j.cell.2019.07.042>.

- Yamada, Y., Bhaukaurally, K., Madarász, T.J., Pouget, A., Rodriguez, I., and Carleton, A. (2017). Context- and Output Layer-Dependent Long-Term Ensemble Plasticity in a Sensory Circuit. *Neuron* 93, 1198–1212.e5. <https://doi.org/10.1016/j.neuron.2017.02.006>.
- Zavitz, D., Amematsro, E.A., Borisyuk, A., and Caron, S.J.C. (2021). Connectivity Patterns Shape Sensory Representation in a Cerebellum-like Network. *bioRxiv* 2021. 02.10.430647. <https://doi.org/10.1101/2021.02.10.430647>.
- Zeppilli, S., Ackels, T., Attey, R., Klimpert, N., Ritola, K.D., Boeing, S., Crombach, A., Schaefer, A.T., and Fleischmann, A. (2021). Molecular characterization of projection neuron subtypes in the mouse olfactory bulb. *Elife* 10, e65445. <https://doi.org/10.7554/eLife.65445>.
- Zheng, Z., Li, F., Fisher, C., Ali, I.J., Sharifi, N., Calle-Schuler, S., Hsu, J., Masoodpanah, N., Kmecova, L., Kazimiers, T., et al. (2020). Structured Sampling of Olfactory Input by the Fly Mushroom Body. *bioRxiv* 2020. 04.17.047167. <https://doi.org/10.1101/2020.04.17.047167>.

STAR★METHODS

KEY RESOURCES TABLE

REAGENT or RESOURCE	SOURCE	IDENTIFIER
Antibodies		
Goat anti-GFP antibody	Rockland Immunochemicals	Cat#600-101-215; RRID:AB_218182
Rabbit anti-Cre antibody	Millipore Sigma	Cat#69050-3; RRID:AB_10806983
Bacterial and virus strains		
JK100L2 Sindbis virus	Kebschull et al. (2016) ; Chen et al. (2019)	N/A
CAV2-Cre	Montpellier vectorology platform	N/A
AAV5- pCAG-FLEX-{EGFP} _{on}	Addgene	N/A
AAV _{DJ} -DIO-{hCAR} _{off}	Li et al. (2018)	N/A
Chemicals, peptides, and recombinant proteins		
Red RetroBeads	LumaFluor	Cat# R170
Green RetroBeads	LumaFluor	N/A
Critical commercial assays		
RNAqueous®-Micro Total RNA Isolation Kit	Thermo Fisher Scientific	Cat#AM1931
Deposited data		
MAPseq and BARseq high-throughput sequencing data	This paper, SRA	SRA: PRJNA707572
<i>In Situ</i> sequencing data for BARseq	This paper, Mendeley data	https://doi.org/10.17632/6t9mb3yydy.1
Images for MAPseq brain dissection	Mendeley data	https://doi.org/10.17632/ggbft4btrb.1
Experimental models: Organisms/strains		
C57BL6J male mouse	Jackson Laboratory	RRID:IMSR_JAX:000,664
Oligonucleotides		
Primers for reverse transcription of barcode mRNA in MAPseq: 5'-CTT GGC ACC CGA GAA TTC CAX XXX XXX XXX XXZ ZZZ ZZZ ZTG TAC AGC TAG CGG TGG TCG-3' X ₁₂ is the barcoded unique molecular identifiers (UMI); Z ₈ are barcoded sample specific identifiers (SSI)	Integrated DNA Technologies	N/A
Nested first PCR forward primer: 5'-ACG AGCTGTACAAGTAAACGCGT-3'	Integrated DNA Technologies	N/A
Nested first PCR reverse primer: 5'-CAAG CAGAAGACGGCATAACGATCGTGATG TGACTGGAGTTCCTTGGCACCCGAGAA TTCCA-3'	Integrated DNA Technologies	N/A
Nested second PCR forward primer: 5'-AA TGATACGGCGACCACCGA-3'	Integrated DNA Technologies	N/A
Nested second PCR reverse primer: 5'-CAA GCAGAAGACGGCATAACGA-3'	Integrated DNA Technologies	N/A
Recombinant DNA		
JK100L2	Kebschull et al. (2016)	Addgene plasmid #79785
Software and algorithms		
ImageJ (Fiji)	Schneider et al. (2012)	https://fiji.sc/
MATLAB	Mathworks	RRID: SCR_001622; https://www.mathworks.com/products/matlab.html
Data processing and analysis scripts	This paper, Mendeley and Github	https://doi.org/10.17632/6t9mb3yydy https://github.com/KoulakovLab/OlfactoryProjectomeAnalysis

RESOURCE AVAILABILITY

Lead contact

Further information and requests for resources and reagents should be directed to and will be fulfilled by the lead contact, Dinu F. Albeanu (albeanu@cshl.edu).

Material availability

This study did not generate new unique reagents.

Data and code availability

- The raw sequencing data for all *in vitro* high-throughput sequencing reported in this study (including six OB MAPseq brains, YC61, YC65, YC86, YC92, YC109, and YC111, two BARseq brains, YC107 and YC113, and five PC MAPseq brains, XC113, XC119, XC120, XC127, and YC123 are available on SRA with accession number PRJNA707572. Images for MAPseq brain dissection and a list of Allen Brain Reference Atlas coronal levels corresponding to the dissected brain slices are available on Mendeley Data (<https://doi.org/10.17632/ggbft4btrb.1>). All data matrices representing OB and PC output neuron identities, soma locations and projection patterns included in the analyses presented here are available on Mendeley Data (<https://doi.org/10.17632/6t9mb3yydy.1>). The DOIs are listed in the key resources table.
- All original code used for analysis is available on Mendeley Data and on Github. DOIs and links are listed in the key resources table.
- Any additional information required to reanalyze the data in this paper is available from the lead contact upon request.

EXPERIMENTAL MODEL AND SUBJECT DETAILS

Animals

13C57BL/6J of 8–10-week old male mice (Jackson Laboratory) were used for MAPseq and BARseq experiments (8 for mapping the olfactory bulb output projections, and 5 for mapping the piriform cortex outputs). In addition, 17 mice were used for experiments cross-validating the projection patterns observed via MAPseq (5 for fluorescent microbeads injections and 12 for CAV2-Cre viral labeling, respectively). All animal procedures conformed to NIH guidelines and were approved by the Institutional Animal Care and Use Committee of Cold Spring Harbor Laboratory. A list of all animals used is provided in [Table S3](#).

METHOD DETAILS

Barcoded Sindbis viral library

A barcoded Sindbis virus library (JK100L2, Addgene plasmid #79785) was generated and used for MAPseq and BARseq experiments as described previously ([Chen et al., 2019](#); [Han et al., 2018](#); [Huang et al., 2020](#); [Kebuschull et al., 2016](#)). *In vitro* sequencing of the viral library revealed that the library contained at least 8 million different barcode sequences. No barcode sequence was found more than once in the 5,309 OB output neurons sampled via MAPseq (6 brains) and BARseq (2 brains). Only 17 barcodes were identified more than once in the 30,433 PC output neurons sampled via MAPseq (5 brains).

Viral labeling of olfactory bulb (OB) output neurons

Mice were anesthetized using oxygenated 4% isoflurane and maintained with oxygenated 0.7–1.0% isoflurane throughout the surgery. Mice received subcutaneous injection of meloxicam (2 mg/kg), dexametasonone (1 mg/kg) and baytril (10 mg/kg) immediately before and after surgery. Lack of pain reflexes was monitored throughout the procedure. Mice were positioned such that the skull dorsal surface is horizontal. Animals were mounted in a stereotaxic frame (David Kopf Instruments), and small craniotomies were performed into the skull above the olfactory bulb, such as to enable injections at multiple penetration sites along the anterior-posterior (A-P) axis. We injected 50 nL Sindbis virus (1:3 diluted) at two depths of 100 μ m and 200–250 μ m (from brain surface) at four penetration sites along the A-P axis of the dorsal aspect of the bulb (0.8, 1.2, 1.7, 2.2 mm anterior to the blood vessel between OB and prefrontal cortex, 0.7–1.0 mm lateral from midline). In a subset of animals (4 mice), we also injected 70 nL (1:3 diluted) Sindbis virus across two depths at 3 penetration sites on ventral aspect of the bulb (0.75 mm anterior, 1.2–1.1 mm lateral, 1.2 and 1.45 mm deep; 1.3 mm anterior, 1.0–1.1 mm lateral, 1.0 and 1.3 mm deep; 1.8mm anterior, 0.8–0.9mm lateral, 1.0 and 1.3mm deep) ([Figure S1A](#)). For the BARseq experiments (2 mice), we injected 70 nL viruses at 200–250 μ m from brain surface into six sites, spaced 500 μ m apart along the A-P axis of the dorsal aspect of the bulb ([Figure S1A](#)). We slowly pressure-injected (Picospritzer II, Parker Hannifin) the virus within 10–15 min via a glass pipet at each depth and waited for 5 min afterward. After injection, we applied Kwik-Cast (World Precision Instrument) to cover the exposed craniotomy and sealed the skin above using tissue adhesive (3M vetbond). Mice were allowed to recover, while waiting for expression of the virus, and euthanized 44–48 h post-injection.

Cryo-sectioning and laser micro-dissection for MAPseq of OB outputs

The brain was immediately extracted from the skull, flash-frozen on dry ice and temporarily stored at -80°C before cryo-sectioning. The whole brain was sliced into 200 μm coronal sections along the A-P axis using a Leica CM 3050S cryostat set at -10°C . To avoid cross-contamination, we used a fresh unused part of a blade to cut each slice and cleaned the brush and the holding platform with 100% ethanol between slices. Each brain slice was melted on a steel frame PEN-membrane slide (Leica microsystems, Cat #11600289) pre-coated with Poly-L-Lysine (Sigma). OB slices cut from brains injected with the Sindbis virus on dorsal OB side only (brains YC61&65) were processed slightly differently. These were melted onto a clean microscope glass slide, rapidly frozen on dry ice and later hand-dissected using cold scalpel while keeping the section frozen. Each brain slice placed on a PEN-membrane slide was immediately processed using following procedure as previously described (Huang et al., 2020): fixation in ice-cold 75% EtOH for 3 min, one rapid rinse in Milli-Q water (Millipore) at room temperature, staining in 0.25% Toluidine Blue O (Sigma-Aldrich, MO) in Milli-Q water for 30 s at room temperature, followed by three quick rinses in Milli-Q water and two post-fixation rinses in 75% EtOH (3 min each) at room temperature. After processing OB slices, we changed to fresh buffers for the rest of brain slices containing the OB target regions so as to avoid contamination of the target regions by barcodes from the injection site. After fixation and staining, we placed each brain slice on a PEN-membrane slide to dry for 30–60 min in a vacuum desiccator, with desiccant at bottom, at room temperature before attaching a second fresh PEN-membrane slide on top of the brain slice. The two PEN-membrane slides, sandwiching the brain slice in the middle, were taped together to prevent the brain slice from falling off or curling up as it continued to dry in the vacuum desiccator overnight.

Dorsal and ventral aspects of OB and target brain regions was laser micro-dissected from each brain slice on a Leica LMD7000 using the Allen mouse Brain Atlas as reference. Each region of interest dissected from every brain slice was collected and transferred into a single homogenizing tube with a homogenizing bead, added with 100 μL lysis solution of RNAqueous-Micro total RNA Isolation kit (Thermo Fisher Scientific), immediately frozen on dry ice, and stored at -80°C as previously described (Huang et al., 2020). To assess cross-sample contamination, we also collected, as negative controls, tissue from brain regions known to receive no direct input from the OB, such as contralateral piriform cortex, ipsilateral primary motor, somatosensory and visual cortex, from at least three brain slices cut along the A-P axis of the brain. To minimize RNA degradation, Laser Capture Micro-dissection was completed within 3–4 days for a single brain post cryo-sectioning.

In our MAPseq experiments, we carefully removed the fibers of passage - the lateral olfactory tract (LOT) - to minimize contamination from fiber tracts. The mitral cell projections mainly travel along the LOT and branch out at different locations to innervate both the PC and extra-PC areas (Ghosh et al., 2011; Igarashi et al., 2012; Nagayama et al., 2010; Sosulski et al., 2011). We identified the LOT using Nissl staining and took advantage of the fact that it is positioned near the surface of the brain (Allen reference atlas) and, thus, easy to remove it using laser dissection.

Sequencing library preparation for MAPseq of the OB outputs

The general procedure of RNA extraction and sequencing library preparation has been described previously (Chen et al., 2019; Han et al., 2018; Huang et al., 2020; Kecsichull et al., 2016). Briefly, we extracted the total RNA of each region of interest dissected from each brain slice using RNAqueous-Micro Total RNA Isolation Kit (Thermo Fisher Scientific) and eluted RNA in 20 μL solution. Before library preparation, we randomly selected and ran several RNA samples from each brain on Bioanalyzer (Agilent Technology) to ensure good RNA quality. We mixed 9 μL total RNA of each sample with 1 μL spike-in RNA ($\sim 1 \times 10^{-9}$ $\mu\text{g}/\mu\text{L}$ spike-in RNAs for each target sample and 1 μL of 1×10^{-7} $\mu\text{g}/\mu\text{L}$ spike-in RNAs for each OB sample), and reverse-transcribed the barcode mRNA into the first-strand cDNA using a gene specific barcoded reverse transcription primer and SuperScript IV (Thermo Fisher Scientific). The barcoded reverse transcription primer has sequence 5'-CTT GGC ACC CGA GAA TTC CAX XXX XXX XXX XXZ ZZZ ZZZ ZTG TAC AGC TAG CGG TGG TCG-3', where X_{12} are the barcoded unique molecular identifiers (UMI) and Z_8 are barcoded sample specific identifiers (SSI). The synthesized first strand cDNA of each sample was labeled with a 12 nt UMI (unique for each RNA molecule) and 8nt SSI (unique for each sample). After synthesis of the first strand cDNA, every 10 to 12 samples of target brain regions or OB (targets and OB of each brain separately before sequencing) were pooled together for clean-up by 1.8 \times SPRI select beads and synthesis of the second strand cDNA. The double-stranded cDNA samples were cleaned up by 1.8 \times SPRI beads (Beckman Coulter) and treated with Exonuclease I (New England Biolabs) to remove the single-stranded reverse transcription primers before PCR amplification.

The double-stranded cDNA samples were amplified by two rounds of nested PCR reactions using standard Accuprime Pfx protocols (Thermo Fisher Scientific) with 2 min extension for each cycle. Primers 5'-ACGAGCTGTACAAGTAAACGCGT-3' and 5'-CAAG CAGAAGACGGCATAACGAGATCGTGATGTGACTGGAGTTTCCTTGGCACCCGAGAATTCCA-3' were used for the first PCR reaction and primers 5'-AATGATACGGCGACCACCGA-3' and 5'-CAAGCAGAAGACGGCATAACGA-3' were used for the second PCR reaction. In the first PCR reaction, the pooled cDNA samples for OB target brain regions and OB were amplified for 12 cycles and 9 cycles respectively in 150 μL volume per 10–12 samples. After treatment with Exonuclease I (New England Biolabs) to remove excess primers, all the PCR1 products of target areas and OB of each brain were pooled together respectively. A quarter of the pooled PCR1 products of target areas and OB were amplified by 14–16 cycles in 8 mL and 13–15 cycles in 4 mL respectively. The PCR2 products were cleaned up and concentrated by SV wizard PCR cleanup kit (Promega), Ampure XP beads (Beckman Coulter), and finally 2% agarose gel electrophoresis. The 233 bp PCR product was cut from the agarose gel, cleaned up by Qiagen

MinElute Gel Extraction Kit and quantified by Bioanalyzer (Agilent Technology) and qPCR. Afterward, we combined OB target regions and OB of two sampled brains together into one sequencing library.

BARseq on OB slices

Mice were euthanized 24–28 h after Sindbis virus injection by brief isoflurane anesthesia followed by decapitation, and the brains were immediately extracted. The olfactory bulb was cut off and either fixed in 4% paraformaldehyde (PFA, Electron Microscopy Sciences) in PBS, post-fixed for 24 h, and cryoprotected before frozen, or directly frozen as previously described (Chen et al., 2019). The bulb hemispheres were then sliced into 20 μm thick sections and processed for BARseq. BARseq library preparation and sequencing was done as previously described (Chen et al., 2019). *In situ* sequencing was performed with a custom-made automated fluidic sequencing system on either a Nikon TE-2000 or an Olympus IX-81 with a Crest X-light v2 spinning disk confocal microscope using an LDI 7-laser light source. Filters and lasers used for each imaging channel documented in Table S4.

Viral labeling of piriform cortex (PC) output neurons

Mice were anesthetized by ketamine (60 mg/kg) and xylazine (10 mg/kg) administered intraperitoneally after a brief induction with oxygenated 4% isoflurane. Mice were positioned with skull dorsal surface horizontal and mounted in a stereotaxic frame as described above and small craniotomies were performed into the skull above the piriform cortex. We injected 100 nL Sindbis viruses (1:3 diluted) unilaterally to three sites along the A-P axis of piriform cortex by positive pressure (anterior: AP +1.75 mm, ML 2.8 mm, DV 4.75 mm from the skull surface of bregma; middle: AP +0.15 mm, ML 3.9 mm, DV 5 mm from the skull surface of bregma; posterior: AP -1.5 mm, ML 4.25 mm, DV 5.5 mm from the skull surface of bregma). 24–48 h after injection, mice were perfused with 4% PFA in PBS, and post-fixed in 4% PFA in PBS for 24 h at 4°C, mounted into OCT in dry ice ethanol batch and stored at -80°C.

Cryo-sectioning and dissection for MAPseq of PC outputs

The brain was sliced from the anterior to posterior end into 200 μm coronal sections with a cryostat (Leica CM 3050S). Each slice was cut by a fresh, unused part of the blade and mounted on a clean microscope glass slide, rapidly frozen on dry ice, and stored at -80°C until dissection. Brain slices were thawed, stained in 0.1% Toluidine blue O (dissolved in 1.0% NaCl, pH = 2.3) for 1 min, washed in PBS for 2 min at room temperature, and kept on wet ice until dissection. Brain areas were hand-dissected from each brain slice under dissection scope by scalpel at room temperature, immediately transferred to 1.5 mL safe-lock Eppendorf tube, frozen on dry ice, and stored at -80°C until RNA extraction. We collected the injection site, ipsilateral piriform cortex, from each brain slice individually and combined together each region of interest collected across multiple slices from a single PC target brain region. To assess cross-sample contamination, we collected as negative controls tissue from the contralateral OB and cerebellum, which are known to receive no input from the piriform cortex. Images of the brain slices were taken before and after dissection.

Sequencing library preparation for MAPseq of PC outputs

Each dissected brain sample was digested with 8 μL of protease in 200 μL of digestion buffer from the RecoverAll™ Total Nucleic Acid Isolation Kit for FFPE (Thermo Fisher Scientific). Samples containing big chunks of brain tissue were homogenized in an electronic homogenizer. Samples were then incubated at 50°C for 15 min and then 80°C for 15 min while shaking at 3,000 rpm. 1 mL of Trizol (Thermo Fisher Scientific) was immediately added to each digested sample and mixed well. We used half of the Trizol-sample mixture to extract the total RNA and stored the other half at -80°C.

General procedures of reverse-transcription and the rest of library preparation were performed as described above. Briefly, after synthesis of the first strand cDNA, PC target brain regions and the piriform cortex injection sites of each sampled brain were pooled together respectively for further library preparation. The double-stranded cDNA was amplified by 15 cycles for the PC target regions and 10 cycles for the piriform cortex injection sites in the first PCR reaction in 250 μL volume (per 8–10 samples) and a quarter of PCR1 products were further amplified by 6–8 cycles in 2 mL total volume for the target brain regions and 6–9 cycles in 12 mL total volume for the piriform cortex injection sites.

Sequencing of the MAPseq samples

The pooled library constructed as described above was sequenced on an Illumina Nextseq500 high output run at paired end 36 with Illumina compatible Read 1 Sequencing Primer and Illumina compatible small RNA read 2 primer as described previously (Kebschull et al., 2016).

qPCR measurement of β -actin in OB target samples

4 μL total RNA extracted from the dissected target areas of one brain (YC61) was reverse transcribed using oligodT primers and Superscript III (Thermo Fisher Scientific) in 20 μL reaction volume. 6 μL of the reverse-transcription products was used to quantify the amount of β -actin cDNA by 3 replicate qPCR reactions in Power SYBR Green PCR Master Mix (Thermo Fisher Scientific) using primers 5'-CGGTTCCGATGCCCTGAGGCTCTT-3' and 5'-CGTCACACTTCATGATGGAATTGA-3'. The relative amount of β -actin mRNA of each sample was normalized to the reference sample and calculated as $2^{-(\text{CT}_{\text{Ref}} - \text{CT}_{\text{Sample}})}$. Sample 7 was used as reference for normalization, which had the smallest CT value, which was consistent across 3 independent qPCR plates.

CAV-2 retrograde tracing to validate OB projections

Mice were anesthetized, positioned and mounted as described above in the viral labeling of PC output neurons section and small craniotomies were performed into the skull above the injection site. We first injected 6–7 weeks old C57BL/6J males (The Jackson Laboratory) unilaterally with 70 nL viral mixture of AAV pCAG-FLEX-{EGFP}_{on} (Addgene plasmid #51502, titer 1.1×10^{12} GC/mL) and AAV-DIO-{CAR}_{off} (titer 1×10^{12} GC/mL) (Li et al., 2018) at 200 μ m depth from the bulb surface, at three penetration sites along the A-P axis of the OB dorsal aspect. Two weeks after the initial injection, we injected 140 nL of CAV2-Cre (Montpellier vector platform, titer 2.75×10^{12} pp/ml) to the middle of piriform cortex (MPC, near the boundary between APC and PPC) or the lateral entorhinal cortex (IENT) in the same hemisphere as the initial OB injection. The stereotaxic coordinates used are the following: MPC, AP 0.15 mm, ML 3.50 mm, DV 5.50 mm and AP 0.15 mm, ML 3.85 mm, DV 5.00 mm from the skull surface of bregma; IENT, AP -3.50 mm, ML 4.40 mm, DV 4.70 mm from the skull surface of bregma. In another set of experiment, two weeks after the initial injection of AAV to the dorsal aspects of OB as described above, we injected 140 nL of CAV2-Cre (Montpellier vector platform, titer 2.75×10^{12} pp/ml) to the middle of piriform cortex (MPC, near the boundary between APC and PPC) or posterior piriform cortex (PPC) in the same hemisphere as the initial OB injection. The stereotaxic coordinates used are the following: MPC, AP 0.4 mm, ML 3.25 mm, DV 5.5 mm and AP 0.4 mm, ML 3.5 mm, DV 5.0 mm from the skull surface of bregma; PPC, AP -2.0 mm, ML 4.25 mm, DV 5.7 mm and DV 5.25 mm from the skull surface of bregma. Two weeks after CAV2-Cre injection, the animals were perfused in 4% PFA in PBS and post-fixed in 4% PFA in PBS for 24 h at 4°C. The fixed brains were sliced into 100 μ m coronal sections on a vibratome (LeicaVT1000S, Leica).

Every other brain slice containing tissue from the piriform cortex was immunostained by Goat anti-GFP antibody (Rockland Immunochemicals, Cat#600-101-215) and Donkey anti-Goat secondary antibody, Alexa Fluor 568 conjugated (Invitrogen) as described (Li et al., 2018). Brain slices with Cav2-Cre injection at MPC, IENT or PPC were immunostained by Rabbit anti-Cre antibody (Millipore Sigma, Cat#69050-3) and Donkey anti-Rabbit secondary antibody, Alexa Fluor 568 conjugated (Invitrogen). After immunostaining, brain slices were stained with DAPI (Sigma), mounted and imaged on an Olympus IX-81 microscope with a Crest X-light v2 spinning disk confocal microscope, an LDI 7-laser light source, and a Photometrics BSI Prime sCMOS camera. Detailed settings of lasers and filters for the imaging channels are shown in Table S4.

The immunofluorescence signals of axonal branches to the piriform cortex from the labeled mitral cells were quantified using Fiji (Schindelin et al., 2012). Rolling ball background subtraction was applied to remove smooth continuous background from each image. The same minimal threshold was then applied for all the images taken of the same brain and the fluorescence intensity above the chosen threshold within OB target brain regions was recorded.

Retrograde tracing to validate PC outputs

We used RetroBeads (LumafLOUR) to retrogradely label PC output neurons that project to different brain regions in 8-to-10-weeks old C57BL/6J male mice (The Jackson Laboratory). Mice were anesthetized, positioned and mounted as described above and small craniotomies were performed into the skull above the injection sites. In one subset of animals (3 mice), we injected 35 nL different fluorescent microbeads (full strength green beads and 1:4 diluted red beads) into the unilateral OB and IENT respectively. In another subset of animals (2 mice), we injected 35 nL green and red beads into the unilateral AON and CoA respectively. The stereotaxic coordinates used are the following: OB, 1.20 mm anterior to the blood vessel between OB and prefrontal cortex, 0.90 mm from the middle line, 0.60 and 1.25 mm deep from the bulb surface; IENT, AP -3.50 mm, ML 4.50 mm, DV 4.75 mm from the skull surface of bregma; AON, AP 3.20 mm, ML 1.25 mm, DV 3.80 mm from the skull surface of bregma; CoA, AP -2.00 mm, ML 2.50 mm, DV 5.80 mm from the skull surface of bregma. To minimize the tracer leakage in the track, we sealed the glass pipette tip using a tiny amount of mineral oil before pipette penetration into the brain and waited for 10 min after injection before slowly retracting the pipette.

Animals were allowed to recover for 3–4 days and perfused and fixed in 4% PFA as described above in CAV-2 retrograde tracing section. The fixed brains were sliced into 100 μ m coronal sections and stained with DAPI. Every other brain slices with piriform cortex was mounted and imaged on an Olympus IX-81 microscope with a Crest X-light v2 spinning disk, an LDI 7-laser light source, and a Photometrics BSI Prime sCMOS camera. Details of lasers and filters for the imaging channels are reported in Table S4.

The fluorescent signals of retrograde labeling in piriform cortex were quantified using Fiji (Schindelin et al., 2012). Rolling ball background subtraction was applied to remove smooth continuous background from each image. The same minimal threshold was then applied for all the images of the same channel (red or green) of each brain. The number of pixels above the chosen threshold within piriform cortex was measured as the intensity of retrograde signals of each brain slice.

Mapping the brain-wide projections of individual olfactory bulb output neurons via MAPseq

Over the past decades, bulk labeling (Haberly and Price, 1977; Luskin and Price, 1982; Price, 1973; Scott et al., 1980; Skeen and Hall, 1977) and axonal tracing studies, in conjunction with dye labeling of single projection neurons from glomeruli (Ghosh et al., 2011; Igarashi et al., 2012; Nagayama et al., 2010; Sosulski et al., 2011) have documented broad and unstructured innervation of large synaptic territories within the piriform cortex (PC), the principal projection target of the olfactory bulb, by individual mitral and tufted cell axons (Bekkers and Suzuki, 2013; Gottfried, 2010; Haberly, 2001; Miyamichi et al., 2011), but see (Ojima et al., 1984; Zeppilli et al., 2021)). Furthermore, pyramidal cells appear to connect to each other in a widely distributed fashion within the piriform cortex (Choi et al., 2011; Franks et al., 2011; Giessel and Datta, 2014; Haberly, 1985; Hagiwara et al., 2012; Johnson et al., 2000; Rennaker et al., 2007; Stettler and Axel, 2009). To date, however, identifying structure in the connectivity of the olfactory system has been impeded by

the scarcity of single cell connectivity data available. While several studies addressed this challenge in insects (Caron et al., 2013; Dasgupta et al., 2017; Eichler et al., 2017; Gruntman and Turner, 2013; Li et al., 2020; Stevens, 2015; Zavitz et al., 2021; Zheng et al., 2020), comparable understanding of the statistics of ensembles of single olfactory bulb or piriform cortex output neuron projections in mammals is lacking (Srinivasan and Stevens, 2019).

Here, we addressed the question of structure in the olfactory cortex circuit taking advantage of high-throughput sequencing based neuroanatomical methods. Multiplexed Analysis of Projections by Sequencing (MAPseq) rapidly maps out the projections of thousands of neurons in a single animal (Han et al., 2018; Kebschull et al., 2016) by uniquely labeling individual neurons in the source region (e.g. mitral cells in the bulb, Figures 1A and 1B) using random RNA barcodes delivered via a Sindbis viral library. The rate of infection is kept low to ensure that most neurons are labeled by only one barcode (Han et al., 2018; Huang et al., 2020; Kebschull et al., 2016). These barcodes are then replicated and transported to the axonal branches. Projections to multiple brain regions can be determined by sequencing and matching axonal barcodes from these target regions (Figure 1C) to the barcodes in the injection area (e.g. olfactory bulb). We collected tissue from the major bulb projection targets at 200 μm resolution along the A-P axis of the brain, including the anterior and posterior piriform cortex (APC/PPC), the anterior olfactory nucleus (AON), the olfactory tubercle (OT, olfactory striatum), cortical amygdala (CoA), and the lateral entorhinal cortex (IENT). These regions play distinct functional roles (Esquivelzeta Rabell et al., 2017; Gadziola and Wesson, 2016; Haberly, 2001; Kikuta et al., 2010; Oetti et al., 2016, 2020; Root et al., 2014; Tsao et al., 2018; Uchida et al., 2014b; Wang et al., 2018, 2020a; Wilson and Sullivan, 2011). We carefully excluded fibers of passage from the lateral olfactory tract (LOT) (STAR Methods).

In MAPseq and Barcoded Anatomy Resolved by sequencing (BARseq), we engineered a carrier protein to bind to RNA barcodes encoded in the Sindbis transcript and transport them to distal axons (Kebschull et al., 2016). The barcode counts are thus largely proportional to the total length of axons. Consistent with this model, the projection patterns of neurons in the visual cortex and motor cortex determined by MAPseq/BARseq were consistent with those determined by single-neuron reconstruction, the gold standard in axonal mapping (Han et al., 2018; Muñoz-Castañeda et al., 2021). Furthermore, MAPseq is also consistent with mesoscale connectivity mapping across the whole cortex (Huang et al., 2020). In these previous studies, we did not notice barcode depletion over long axons, including locus coeruleus projections that cover the whole anterior-posterior span of the cortex (Kebschull et al., 2016; also see discussion in [method details](#) about the projections to OT). Therefore, barcoding-based strategies, including BARseq and MAPseq, can qualitatively capture the distribution of axons across brain regions.

Both BARseq and MAPseq have been extensively validated in other brain regions, and results have confirmed and extended those obtained by classical neuroanatomical methods, including retrograde labeling, bulk anterograde tracing, and single-cell tracing (Chen et al., 2019; Han et al., 2018; Huang et al., 2020; Kebschull et al., 2016). Previous reports also addressed other potential technical concerns, such as double barcode labeling of neurons, distinguishing fibers of passage from axonal termini, and uniformity of barcode transport (Chen et al., 2019; Han et al., 2018; Huang et al., 2020; Kebschull et al., 2016).

The extent of the MAPseq projection data depends on the efficiency of neuronal infection by the virus. To label mitral and tufted cells in the olfactory bulb, we injected barcoded Sindbis virus at multiple sites along the anterior-posterior (A-P) axis on both the dorsal and ventral aspects of the bulb in one hemisphere per experiment (Figure S1A). On average, this approached labeled ~ 800 mitral, tufted and deep cells per bulb hemisphere, amounting to 4,894 olfactory bulb projection neurons recovered from six brains.

The spatial resolution of the MAPseq projection data depends on the parameters used for tissue dissection. Since the entire piriform cortex (PC) covers a long (~ 5 mm) and narrow (~ 1 -2 mm) portion on the ventral-lateral aspect of the mouse brain, we focused on investigating the projection patterns of bulb output neurons along the A-P axis of piriform cortex. To achieve mapping at fine resolution, we cut 200 μm coronal sections along the A-P axis of the brain (Figure 1A). We sampled all 6 major olfactory bulb target brain regions: anterior olfactory nucleus (AON), piriform cortex (anterior, APC and posterior, PPC), olfactory tubercle (OT), cortical amygdala (CoA), and lateral entorhinal cortex (IENT). From each coronal section, we dissected different regions of interest using laser capture micro-dissection (LCM, Figure 1C); to minimize contamination from fibers of passage, we avoided the lateral olfactory tract (LOT, Figure S1B). We also sampled the hippocampus in two brains, but found very few barcodes in this area, indicative of weak olfactory bulb projections. We thus did not harvest it in the other four brains and focused our analyses on the six target regions mentioned above. The sampled olfactory bulb target regions could be readily separated from each other by LCM based on location and Nissl staining. To minimize cross-contamination between these olfactory bulb target regions, we avoided harvesting tissue at the inter-region boundaries. For example, for each sampled bulb target region, we discarded 1–2 tissue slices collected from the most anterior and posterior ends, and also skipped a thin slab of tissue (<0.1 mm wide, Figure 1C) between the anterior piriform cortex and olfactory tubercle.

Images acquired after LCM for each of the brain slices sampled are available on Mendeley Data (<https://doi.org/10.17632/ggbft4btrb.1>). To align the A-P positions of olfactory bulb projections across different brains, we registered each coronal slice to the Allen Brain atlas. We first registered several slices using landmarks such as the closure of corpus callosum and anterior commissure, as well as the anterior end of the hippocampus. Subsequently, we matched the rest of the slices based on the ~ 200 μm nominal distance between two adjacent slices. After registration, we only kept samples that were common across different brains and discarded extra samples, which usually were collected at the beginning or the end of a given brain region and received no, or minimal olfactory bulb input. Our registration aligns well with the non-rigid registration generated by the whole brain software (<http://www.wholebrainsoftware.org/>) (Fürth et al., 2018). The average difference between these two registration methods for individual slices

was 1.4 ± 1.2 (mean \pm std) coronal levels, equivalent to 140 ± 120 μm . The differences in registration across the two methods used may arise from imperfect Nissl staining and cryo-sectioning, especially near the anterior and posterior ends of a brain.

The false positive rate of MAPseq in the data collected was low: only 1.74% barcodes could be detected (have non-zero barcode counts) in negative control samples known to receive no input from the olfactory bulb. Importantly, for these barcodes which had non-zero counts, the mean molecule count was 2 compared to 203 in an olfactory bulb target brain region.

We normalized the variation in library preparation and sequencing across different samples for each brain based on the recovered spike-in RNA added to each sample. To examine whether variations in area size or tissue thickness could contribute to differences in barcode counts, we compared this normalization method to normalization by: 1) dissected area size and 2) tissue volume (measured by qPCR of β -actin) for one brain (YC61). Normalization based on spike-in RNA alone, normalization based on both spike-in RNA and area size, or on tissue volume produced similar projection patterns (Figure S1C) and did not change the correlations in olfactory bulb projections to piriform cortex and extra-piriform areas reported (Figures 2, 3, and S1C–S1E). We therefore normalized only by spike-in RNA for the other brains sampled as also done in previous MAPseq and BARseq studies (Chen et al., 2019; Han et al., 2018; Huang et al., 2020; Kebschull et al., 2016; Sun et al., 2020).

Classification of the olfactory bulb projection neurons

We first trained a neural network-based classifier to distinguish mitral, tufted and deep cells based on the brain region-level projection patterns of the BARseq sampled neurons. To train this classifier, we defined a set of template neurons based on the locations of their cell bodies: putative tufted cells (pTC) were defined as those olfactory bulb projection neurons whose somata were at least 150 μm away from the mitral cell layer (MCL), and less than 100 μm from the inner surface of glomeruli; putative mitral cells (pMC) as those bulb projection neurons whose somata lied within 50 μm of the mitral cell layer; finally, putative deep cells (pDC) were defined as those with somata located 100 μm below MCL, or deeper (Figure 1F). Multiple types of tufted cells exist across different layers in the olfactory bulb, including some very close, or embedded within MCL (Schwarz et al., 2018). As such, pTC used as templates comprised largely of tufted cells located more superficially, whereas pMC neurons may represent a mixture of mostly mitral cells, as well as a minority of deep tufted cells displaced in the MCL.

The classifier was based on a two-layer feedforward neural network that computed the Bayesian probability of a neuron to belong to different cell types (pMCs/pTCs/pDCs) given their density of projection to the six olfactory bulb target regions sampled. The classifier was optimized so as to minimize classification error (softmax) in the BARseq dataset (265 mitral cells/tufted cells/deep cells defined based on soma position in the olfactory bulb), and did not distinguish barcodes based on their fine distributions of projection within each target brain region (Figures 1F and S2A). Our classifier identified pMC with high accuracy (TPR = 94%, FPR = 10%), but performed worse for identifying pDC and pTC (Figure 1F). The higher performance at identifying mitral cells is expected given a bias in viral labeling of mostly mitral cells in our experiments. Such a bias may arise from our injections aimed to target MCL, potential tropism of the Sindbis virus and/or potential bias in barcode recovery near the borders of areas during laser capture micro-dissection. However, our results show that the classifier identifies pMC with high accuracy on the BARseq data. Hence, we further applied the classifier to the (larger) MAPseq dataset (Figure S2D), and found similar fractions of pMC neurons in each sampled brain (Figure S2E).

We chose the neural network parameters for the classifier using a grid search. For the grid search, we trained multiple architectures of networks multiple times (500), and further chose the architecture with lowest cross-entropy loss on average on the template dataset. The architectures tested were: single hidden layer of size 16, single hidden layer of size 20 and two hidden layers of size 10 each. These architectures were chosen to keep the number of weights low compared to the number of training data points so as to avoid overfitting. We chose to train the network on the entirety of the BARseq dataset, since our BARseq dataset is unbalanced and we had a relatively small number of data points. To check for overfitting, we compared this network to networks utilizing the same winning architecture (two hidden layers of size 10 each), but which were trained using a training and testing split approach. In particular, we split the BARseq data 90/10% and 80/20% respectively. We found that, on average, the classification performances obtained from training the classifier using the whole BARseq dataset versus training by splitting the BARseq dataset into training and testing sets were highly correlated (Figures S2F and S2G). Thus, training using the whole dataset appears to generalize well on this dataset. Since the result of the classification is probabilistic, we could evaluate the confidence in classification from these probabilities (Figure S2H). Consistent with robust classification of pMC neurons, most pMC (4,388 out of 4,665) were classified with more than 85% accuracy. We cannot rule out the possibility that, despite our cross-validation strategy (Figure 1), narrowly projecting cells also include a minority of internal tufted cells displaced in the mitral cell layer (Mori et al., 1983; Schwarz et al., 2018). To minimize the effect of potential contamination, we further restricted our analysis to the projections of these bulb output neurons classified as mitral cells with high confidence (>85%). Importantly, while how to exactly classify mitral and tufted cells remains an open issue, independently of cell type identity conventions, both narrowly and broadly cell populations display characteristic co-innervation of specific extra-piriform bulb target regions as a function of their targeted A-P piriform locus.

Differences in brain-wide projections of output neurons across different domains of the olfactory bulb

In four mice, we infected output neurons on both the dorsal and ventral surface of the olfactory bulb (Figures S1A and S3A). Comparing the projection patterns of dorsal and ventral pMC neurons revealed small, but statistically significant differences in the distribution of projections to all six bulb target brain regions sampled (Figure S3B; $p = 0.004$ for AON, $p = 0.027$ for APC, $p = 9.9 \times 10^{-18}$ for PPC, $p = 0.0048$ for OT, $p = 1.2 \times 10^{-11}$ for CoA, and $p = 1.1 \times 10^{-16}$ for IENT, rank sum tests after Bonferroni

correction). For example, differences observed in CoA projections were consistent with previous reports that CoA receives more input from the dorsal than ventral aspects of the olfactory bulb (Miyamichi et al., 2011). In addition, PPC and IENT also appear to receive richer input from the dorsal aspect of the olfactory bulb. Importantly, the correlations between projections to different bulb target regions outlined in Figure 2E were observed in both dorsal pMC and ventral pMC neurons (Figure S3C). For both the dorsal and ventral pMC neurons, we further examined whether projection strengths to particular olfactory bulb target regions were dependent on the A-P positions of neuronal somata in the bulb (Figures S3D and S3E). For projections to each bulb target brain region, we calculated the mean projection strengths of all olfactory bulb output neurons at that A-P position, relative to the mean projection strengths of shuffled neurons with randomized A-P labels (method details). This analysis did not find statistically significant biases in projections for output neurons along the A-P axis of the olfactory bulb (Figures S3D and S3E), consistent with previous reports (Miyamichi et al., 2011; Scott et al., 1980). Also, similar to previous observations, we did not identify a systematic relationship between the location of bulb output neuron somata along the A-P axis of the olfactory bulb and the strength of their projections along the A-P axis of piriform cortex (Figure S3F).

Correlations between individual neuronal bulb output projections along the A-P axis of piriform cortex and their co-projections to extra-piriform areas

Mitral cell axons form orderly representations in the piriform cortex as defined by their co-projections to other brain regions. Both according to our data and previous observations (Ghosh et al., 2011; Sosulski et al., 2011), the same mitral cell usually branches and sends afferents to the piriform cortex and other, extra-piriform, brain regions. Here, for each position in the piriform cortex, we determined the conditional probability of projecting to other olfactory bulb target regions $P(\text{target}|\text{PC location})$. This probability describes the rate at which bulb output axons tend to connect to extra-piriform regions given that they also connect to a given position in the piriform cortex (Figures 3C and S4B). If the olfactory bulb-to-piriform cortex connectivity were absolutely random, these conditional probabilities would be constant throughout the piriform cortex and independent on the piriform cortex location (Figure S4C). Instead, we show that this probability displays orderly, close to linear, variation as a function of piriform cortex location (Figure 3C). This implies that co-innervation of the piriform cortex and three other olfactory bulb major targets (AON, CoA and IENT) varies systematically in the piriform cortex. Our findings are therefore inconsistent with the hypothesis of random connectivity between the olfactory bulb and the piriform cortex. Interestingly, the same conditional probability of projections experiences a discontinuous change in the slope of variation at the border between the anterior and posterior piriform cortex, giving another example of the fine spatial organization of projections (Figure 3C).

We did not observe a systematic organization along the A-P axis of the sampled piriform cortex inputs and outputs in terms of their co-projections to the OT. There may be, however, other subdivisions of the piriform (Haberly, 1985, 2001), not directly defined by the A-P axis. Further investigation of the logic of projections with respect to the dorsal-ventral and medial-lateral (Ojima et al., 1984) axes will provide insight into whether spatially structured organization exists along these dimensions for projections to the OT, and to the other extra-piriform bulb target regions.

Our findings are consistent with an early study (Ojima et al., 1984), which reported spatially restricted projections from the olfactory bulb to the piriform cortex by reconstructing the axonal arborizations of 12 mitral cells in the rabbit. However, spatially restricted projections are consistent with both spatially organized and randomly organized projections. As such, Ojima et al. did not explicitly address the issue of spatial organization of the bulb to piriform projections and was largely overshadowed by later, bulk- and single neuron-tracing studies that concluded that bulb-to-piriform cortex connectivity is random.

Using CAV-2 retrograde labeling to validate correlations observed in the putative mitral cell projections to the IENT and PPC

To validate some of the observations obtained via MAPseq that pMC projections to extra-piriform areas are correlated with dominant projections to specific positions along the A-P axis of piriform cortex (Figure 3C), we used a CAV-2 retrograde viral labeling strategy (Li et al., 2018) (Figure S5). Specifically, we focused on probing the mitral cell projections to the IENT and PPC. We first injected AAV-FLEX- $\{\text{EGFP}\}_{\text{on}}$ and AAV-DIO- $\{\text{CAR}\}_{\text{off}}$ to target mitral cells on the dorsal side of OB and waited two weeks to allow optimal expression of CAR (coxsackievirus and adenovirus receptor), which acts as the receptor for CAV-2 and, thus, can help overcome potential CAV-2 tropism enabling efficient retrograde labeling (Li et al., 2018). Further, in one set of experiment, we injected CAV2-Cre in either IENT or into the middle of piriform cortex (near the boundary between APC and PPC) to retrogradely turn on EGFP expression in mitral cells that were also infected with AAV-FLEX- $\{\text{EGFP}\}_{\text{on}}$. In another set of experiment, we injected CAV2-Cre in either PPC or into the middle of piriform cortex. Because both the IENT, PPC and the middle region of the piriform cortex have been reported to receive inputs only from mitral cells, but not tufted cells (Ghosh et al., 2011; Igarashi et al., 2012; Nagayama et al., 2010; Sosulski et al., 2011), this labeling strategy enables us to examine the distribution of mitral cell projections along the A-P axis of the piriform cortex. Consistent with our MAPseq results, CAV2-Cre injection in IENT showed substantially stronger labeling in the posterior portion of the piriform than CAV2-Cre injection targeted to the middle of the piriform cortex (Figures S5A and S5B). Moreover, CAV2-Cre injection in PPC showed significantly stronger labeling in IENT and CoA than CAV2-Cre injection targeted to the middle of the piriform cortex (Figure S5C). Thus, these results further confirm our finding using MAPseq that mitral cell projections to extra-piriform projections are correlated with the distribution of their co-projections along the A-P axis of piriform cortex.

NARROWLY AND BROADLY PROJECTING PUTATIVE MITRAL CELLS DIFFERENTIALLY TILE THE A-P AXIS OF THE PIRIFORM CORTEX

Our sample of putative mitral cells (pMC) helps understand the remarkable heterogeneity in their connections. We identified two distinct classes of mitral cells according to their projection width (Figures 4A and 4B). The width of projections can be characterized by the Inverse Participation Ratio (IPR), a metric describing the number of tissue slices a given cell projects to (method details). Cells forming narrow/broad projections are described by low/high IPR respectively. Based on the sparseness of whole brain projections, pMCs from six brains were divided into two populations using a watershed algorithm (method details): ~80% were classified as broadly projecting (BP) and the rest 20% as narrowly projecting (NP) (Figures 4A, 4B, and S6A). Indeed, these two groups have distinct projection patterns: Broadly projecting cells project across all olfactory bulb target brain regions sampled and narrowly projecting cells mainly target the AON, APC and OT, though a subset (~50%) of them also project to PPC and CoA (Figures 4C, 4E, and 4F). Within each bulb target brain region, broadly and narrowly projecting mitral cells innervate distinct domains (Figure S6B): broadly projecting neurons project most strongly to the caudal portion of the anterior piriform cortex and the boundary between the anterior and posterior piriform cortex, while narrowly projecting neurons target most strongly the anterior part of APC; furthermore, within AON, broadly projecting neurons project more anteriorly than narrowly projecting neurons and more posteriorly than narrowly projecting cells to the OT, CoA and IENT. Given their different spatial distributions along the A-P axis of the piriform cortex and extra-piriform target regions, the projection gradients formed by the narrowly and broadly projecting mitral cells cannot be explained by technical issues of barcode trafficking.

We identified pMC by checking the MAPseq-based projection results against the projection patterns of mitral, tufted and deep cells found using BARseq (where cell identity is assigned based on soma location within the olfactory bulb). While the narrowly and broadly projecting cells appear to represent two subpopulations of mitral cells which differ in their projection patterns, we cannot rule out the possibility that narrowly projecting cells also include a minority of internal tufted cells displaced in the mitral cell layer (MCL) (Mori et al., 1983; Schwarz et al., 2018). The projections of NP cells, however, are distinct from those of tufted cells identified by previous tracing studies (Igarashi et al., 2012; Nagayama et al., 2010) and also from those of neurons classified here as tufted cells based on their cell body location in the external plexiform layer (EPL) (Figure S4A), and include axonal branches that target, for example, the PPC and CoA. Importantly, independently of cell type identity conventions, both narrowly and broadly cell populations tile the piriform cortex in a non-random and reproducible manner and display characteristic co-innervation of specific extra-piriform bulb targets.

Interestingly, both narrowly and broadly projecting cells' axons tile (cover completely) the A-P axis of anterior piriform cortex. The tiling, however, is different for the narrowly and broadly projecting neurons. Narrowly/broadly projecting cells prefer anterior/posterior APC and follow exponential and inverted exponential distributions respectively, referenced to the anterior boundary of the piriform cortex [Equation 1 and Equation 2]. While only a fraction of the sampled narrowly projecting neurons tile PPC, BP neurons projection maxima cover the full extent of the PPC following an exponential distribution [Equation 1]. The tiling by narrowly projecting cells reveals a potential pitfall for tracing studies involving multiple neurons at the same time. When multiple narrowly projecting cells are traced, they may appear to form a broad projection spanning the entire A-P axis of the anterior piriform cortex, while individual neurons form specific projections, even if these cells may originate in a single glomerulus (Ghosh et al., 2011; Sosulski et al., 2011). Thus, when examining the specificity of the olfactory bulb-to-piriform cortex connectivity, both single-neuron resolution and high throughput are necessary.

Are projections of the same olfactory bulb output neuron to the anterior and posterior piriform cortex correlated? To answer this question, we examined the simultaneous tiling of these piriform cortex subdivisions by projection peaks of the same neurons. The same NP neuron can form projections in both the APC and PPC and locations of the peaks of in projection can be identified in each piriform subdivision (Figures 4E, 4F, S6E, and S6F). As discussed above, narrowly projecting cells (Figures 4E and S6E) display exponential tiling [Equation 1] along the A-P axis of the anterior piriform cortex. The same is true for the narrowly projecting cells which target the posterior piriform cortex. When the same neurons are re-sorted according to the location of PPC projection maxima (Figures 4F and S6F), they follow exponential tiling similar to APC. For the same neuron, the locations of peaks in the anterior and posterior piriform cortex are however uncorrelated (Figures 4G and S6I). A similar feature is observed in the tiling distributions by broadly projecting neurons. For the same neuron, locations of peaks in projection density in the anterior and posterior piriform cortex appear to be independent (Figures 4H, 4I, S6G, and S6H) with no observed correlation (Figures 4J and S6J). Because broadly projecting cells display an inverted exponential tiling in the anterior piriform cortex [Equation (2)], these neurons form denser projections in the posterior APC and anterior PPC respectively, thus contributing to the peak in projection density observed at the boundary between the anterior and posterior piriform cortex (Figure 4J). Overall, our findings suggest that connectivity of the same bulb output cell to the APC and PPC is not correlated. Within a scenario in which the A-P locations of projections in the anterior and posterior piriform cortex correlate with the representation of two variables important for olfactory processing, these variables appear independent. Further investigation is necessary to determine the functional implications of the piriform cortex tiling by bulb projections and of the strong innervation of the APC/PPC boundary region which is suggestive of anatomical modules beyond the APC and PPC cortical subdivisions.

INTRA-PIRIFORM AND BRAIN-WIDE PIRIFORM CORTEX PROJECTIONS AND COMPARISONS WITH PREVIOUS WORK

MAPseq analysis of intra-piriform connectivity and brain-wide organization of piriform cortex output neurons recapitulate previous observations (Chen et al., 2014; Datiche et al., 1996; Diodato et al., 2016; Hagiwara et al., 2012; Large et al., 2018; Luna

and Pettit, 2010). First, clustering of piriform cortex slices based on their bidirectional intra-piriform connectivity across cortical slices identified two groups of slices that were highly connected within each group, but sparsely connected across groups. These two groups corresponded to the anatomically-defined APC and PPC, respectively, indicating that differences found in intra-piriform connectivity match the anatomically defined APC-PPC boundary (Figure S7A). Second, consistent with previous observations on connectivity within the piriform cortex, APC-to-PPC projections were stronger than PPC-to-APC projections (Figures 5B and 5C). Third, at the population level, the projection strengths of the piriform cortex outputs to specific target regions were consistent with bulk tracing data obtained using the Allen Brain Atlas (Figures S7B–S7D). Furthermore, the APC-to-APC and PPC-to-PPC correlations between our data and the Allen Brain atlas were significantly higher than correlations between APC and PPC across these datasets (Figure S7E). Overall, these observations indicate that MAPseq projection data capture well previously reported APC versus PPC differences in both piriform cortex output and intra-piriform connectivity.

Previous work using a combination of optogenetic stimulation and intracellular recordings (Franks et al., 2011) in acute piriform cortex slices reported that the probability of a pyramidal cell receiving any input (at least one synapse) from a given piriform locus is largely independent on the distance to the origin. This study also reported that the density in connectivity decays with distance as assayed by the diminishing amplitude of light-evoked EPSCs. Our results, based on mapping the average spatial decay of the intra-piriform projections of ~30,000 cortical output neurons are in qualitative agreement with these previous findings. The reported quantitative differences in the steepness of spatial decay of connectivity (fitting of our power-law Lorentzian dependence with an exponential yields a spatial constant, λ of 0.7 vs. 2.0 mm (Franks et al., 2011)) could be due to differences in the type of measurement of connectivity (anatomical vs. light-evoked EPSCs), accuracy of the exponential fits calculated from a small number of recorded cells available per slice, uncertainty in the amplitude of EPSCs at the Chr2 infection site and variability across slices.

PIRIFORM CORTEX OUTPUT NEURON GROUPS DIFFER IN THEIR DOMINANT PROJECTION TARGETS ALONG THE A-P AXIS OF THE CORTEX

We used two layers of Louvain community detection (Blondel et al., 2008) to cluster piriform cortex projection neurons into groups, then manually combined groups from the second layer that did not appear disjointed when visualized using t-SNE (Figures 5E and S7F). This resulted in six groups that were differentially distributed along the A-P axis of the piriform cortex (Figures 5F, S7G, and S7H) in a manner reproducible across brains (Figure S7H). The projection patterns of these piriform cortex output neurons partially predicted the A-P locations of their somata compared to the full output projection patterns (method detail). Prediction errors were 1.0 ± 0.1 mm (mean \pm SEM) when using the six groups identity only, compared to 1.3 ± 1.4 mm when using shuffled data, and 0.7 ± 0.5 mm when using the full projection patterns of the sampled piriform cortex output neurons (Figures S7I and S7J). Interestingly, additional, finer gradients of projection along the A-P axis were observed within some of the groups (Figure 5E). For example, while neurons in group 5 were heterogeneous in projecting to many piriform cortex targets, their distribution of along the A-P axis of piriform cortex showed a bimodal projection distribution that correlated specifically with projections to the striatum and the contralateral piriform cortex: neurons in the anterior portion of piriform cortex mostly projected to caudate-putamen (CP), whereas neurons in the posterior portion of piriform cortex also projected to nucleus accumbens (ACB) and the contralateral piriform cortex.

Importantly, the groups of piriform cortex neurons defined by their output projection targets also showed different biases in their intra-piriform projections: e.g., neurons in group 1, which projected to AON, were more likely to project anterior within the piriform cortex ($p = 3.6 \times 10^{-94}$, Sign-rank test after Bonferroni correction), whereas neurons in group 3, which projected to IENT ($p = 1.9 \times 10^{-303}$, sign-rank test after Bonferroni correction), were more likely to project posterior within the piriform cortex (Figure S7K). We cannot rule out, however, the possibility that some of these differences in intra-piriform projections were contributed by passing fibers of the output projections.

Taken together, these findings reveal the existence of systematic gradients, reproducible across individuals, along the A-P axis of the piriform cortex, both in terms of projection modules within the piriform cortex, as well as with respect to the organization of piriform cortex outputs to other brain regions.

QUANTIFICATION AND STATISTICAL ANALYSIS

MAPseq data processing

The raw MAPseq data consist of two fastq files, with paired end 1 covers the 30 nt barcode sequence and paired end 2 covers 12 nt UMI and the 8 nt SSI (Huang et al., 2020; Kecsichull et al., 2016). The raw sequencing data was pre-processed in bash and then analyzed in MATLAB (Mathworks) as previously described (Chen et al., 2019; Han et al., 2018; Huang et al., 2020; Kecsichull et al., 2016). We first sorted the barcodes from each sample based on the SSI sequence and then counted the number of UMI as the molecule number of individual barcodes. Subsequently, we matched the barcodes in the injection sites to barcodes in the target brain regions based on barcode sequences and generated a barcode matrix containing the barcode sequences and their corresponding molecule counts for each sample.

We only analyzed barcodes that had molecule counts larger than 50, but smaller than 100,000 in the injection site (OB or PC) and had more molecule counts in the injection site than in any of the target brain regions sampled. To exclude low-confidence projections, we required a barcode to have at least 10 molecule counts in the PC target regions (sampled at the brain region resolution) or at least 3

molecule counts in the OB target regions (sampled at single slice level). We have also normalized the variation in library preparation and sequencing across different samples within each brain based on recovered spike-in RNA (see Method Details) as described previously (Han et al., 2018; Kecsuschull et al., 2016).

OB projection data analysis

All analyses were based on barcode counts normalized by spike-in RNA counts. All analyses were done in MATLAB.

To examine the relationship between pMC soma positions and their projections, we calculated the “projection bias” for each A/P soma position in the bulb. To calculate the projection bias for a given A/P position, we calculated the mean projection barcode counts to an area for neurons at that A/P position. We also calculated the mean projection barcode counts after shuffling the A/P position labels of neurons. The projection bias is then defined as the ratio between the mean projection barcode counts for the experimentally observed data and that for the shuffled data, and this ratio was plotted as the relative projection strength in Figures S3D and E.

IPR

The inverse participation ratio (IPR) is a frequently used measure of vectors’ sparseness (Wegner, 1980). It is related to the lifetime or population sparseness (Treves and Rolls, 1991; Willmore and Tolhurst, 2001), however, IPR is designed to directly represents the

number of non-zero components in the vector. For a vector \vec{x} with components x_i , IPR is defined as $IPR(\vec{x}) = \left(\sum_i x_i\right)^2 / \sum_i x_i^2$.

For example, for a vector which contains N non-zero components all equal to c , IPR is equal to N . IPR also does not depend on the scale of vector \vec{x} : multiplying \vec{x} by a number, i.e. the transformation $\vec{x} \rightarrow c\vec{x}$, does not change its value. We therefore used IPR to quantify the average number of non-zero vector components for each barcode sequence. For the vector \vec{x} with components x_i describing the number of molecules found in brain slice i for a particular barcode sequence, IPR gives an estimate of the number of slices substantively occupied by that barcode sequence.

OB target region pairwise correlations

Pearson correlation between pMC projections across pairs of OB target regions was calculated in MATLAB using spike-in normalized barcode counts per brain region. Only correlations that passed statistical significance after Bonferroni correction are shown in Figure 2E.

Classifiers

To cluster the MAPseq barcoded neurons into pMCs, pTCs and pDC, we used a three-layer fully connected feedforward neural network (NN). In the BARseq dataset, barcoded neurons of different cell types were clearly identified based on their positions within the olfactory bulb (distance from surface and from the mitral cell layer respectively). We then trained a NN to predict the cell types using the projections of the BARseq identified neurons to the six OB target regions sampled (265/415 neurons sampled via BARseq). The NN was further used to estimate the probability of assigning a barcoded neuron to a certain type using the MAPseq projection dataset (6 brains). We used the trained NN to obtain the classification probabilities of 4,894 barcoded neurons from the MAPseq dataset. A 0.85 or higher probability of belonging to the pMC cluster was considered a hit, and the corresponding barcoded neuron labeled as pMC. Details of the classifier are described in method details.

Conditional probability analysis

We used conditional probability as a measure of normalized co-innervation strength between different locations in the piriform cortex (PC) and target regions (AON, OT, CoA, IENT). The conditional probability is interpreted as the probability of observing a barcode molecule within the target regions, given that a molecule of the same barcode was also observed in a specific slice in PC. Our calculation is based on the matrix $C(b, s)$ of spike-in normalized molecule counts for the barcode b in piriform cortex slice s from the MAPseq data. This matrix was used to calculate the probability of finding a barcode molecule in a given PC slice. Across the PC slices, this probability is $p(s|b) = C(b, s) / \sum_{s' \in PC} C(b, s')$ and across the target regions, enumerated by the index $r = 1..4$, it is $p(r|b) = \sum_{s \in r} C(b, s) / \sum_{s' \in \text{all } r} C(b, s')$. These two conditional probabilities formed the basis for our calculation.

Since most OB pMC project to PC, we can assume that these barcodes are present in PC. We then reasoned that the probabilities of these barcoded neurons to be present in PC should therefore be equal, i.e. $p(b) = 1/N_B$, where N_B is the total number of barcodes detected in PC. We have verified that our conclusions are not affected by this assumption. Indeed, adopting a different model for $p(b)$, such as $p(b) \propto \sum_s C(b, s)$ does not noticeably affect our results. We further used the law of total probability to calculate the probability of a barcode molecule being sampled from a given slice in PC: $p(s) = \sum_b p(s|b)p(b)$.

To compute the conditional probability of finding a barcode molecule b in a given PC slice s , we used Bayes’ theorem: $p(b|s) = p(s|b)p(b)/p(s)$. Then, using the law of total probability, we calculated the probability that a barcode molecule comes from a given target region, granted that another molecule of the same barcode is found in PC slice s : $p(r|s) = \sum_b p(r|b)p(b|s)$. Simplifying the calculation under the uniform sampling of barcoded neurons $p(b) = \text{const}$, we calculated the conditional probability of projecting to a given target region given that molecules of the same barcode are found in the PC slice:

$$\begin{aligned}
 p(r|s) &= \sum_b p(r|b)p(s|b)p(b) / \sum_{b'} p(s|b')p(b') \\
 &= \sum_b p(r|b)p(s|b) / \sum_{b'} p(s|b')
 \end{aligned}
 \tag{Equation 3}$$

Regression analysis and shuffled controls

To determine the robustness of our analysis to sampling effects, we used bootstrap to re-sample the set of barcodes with replacements and recalculate the conditional probability matrices. Piecewise linear regressions on APC and PPC vs. single linear regression along the whole of PC anterior-posterior axis better fitted the data as indicated by using 10-fold cross-validation (Table S1). Similar results were obtained shuffling the PC slices by randomly permuting the AP positioning order in the conditional probability matrix (data not shown).

Down-sampling controls

To investigate the effects of lower throughput on reaching statistical significance on our observations, we down-sampled the pMC neurons of our MAPseq dataset to various sizes. On these sets, we calculated the conditional probability matrices and performed the same analyses. We note that most of our results become statistically insignificant on these smaller datasets, suggesting that large sample size is necessary to discover the patterns of projection observed in our data (Figure S4D).

Tiling

To quantify tiling, we sorted the barcoded neurons according to the A-P location of the maximum projection count in different slices (Figures 3A, 4C–4D, etc.). To separate the barcoded neurons into narrowly and broadly projecting populations, we computed their IPR and average A-P PC locations, and build the 2D distribution according to these quantities (Figure 4A). Narrowly and broadly projecting groups could be well-separated using a watershed algorithm in the 2D plane. The boundary generated by the watershed algorithm in shown in Figure 4A by the white line. We performed exponential fits (red curves in Figure 4) using standard non-linear fitting functions available in MATLAB (Mathworks). The functional model used was $x(r) = w \exp(-\alpha r)$, where x , r , w , and α are the A-P location of a barcoded neuron projection maximum, A-P rank of the barcoded cell (neuron number), the width of the tiled brain region corrected for edge effects (number of slices - 1), and the only fitting parameter, representing the exponent's decay.

Piriform cortex projection data analysis

For all analysis of intra-PC projections, we excluded the three slices adjacent to each soma location (one slice on each side and the central slice, representing $\sim 600 \mu\text{m}$ along the A-P axis) because of possible contribution of barcode molecules from the dendrites of the barcoded neurons. To cluster PC slices, we first re-sampled with replacement 500 neurons for each A-P position to equalize the number of neurons from different A-P positions, then used the correlation of barcode molecule counts between PC slices to build an adjacency matrix and performed Louvain community detection (Blondel et al., 2008). To compare PC outputs to the Allen projection atlas, we calculated the Pearson correlation between the mean barcode molecule counts for each area and GFP intensities from the Allen projection atlas (Figure S7). Neurons in APC were compared to experiment ID 127907465 and neurons in PPC were compared to experiment ID 146857301.

We fitted the piriform projections using the Lorentzian function $f(x) = A/(1 + x^2/w^2)$. Here A and w are the fitting parameters representing the amplitude and the width of the function respectively. These parameters were found using standard non-linear fit function of MATLAB (Mathworks, Inc.). The values of the twice the distribution width are marked in Figure 5D. Thus, for intra PC connectivity, we obtain $w \approx 0.5\text{mm}$, leading to the curve's width at half height of 1mm as indicated in Figure 5D.

To identify groups of PC neurons based on output projections, we performed two layers of Louvain community detection, then manually combined clusters resulted from the second layer if they were intermingled in the t-sne plots (Figure 5E). To determine the relative anterior/posterior bias of intra-piriform projections, for each neuron in slice X along the A-P axis of the piriform cortex, we calculated the difference in barcode molecule counts in slices $X - 8$ to $X - 3$ (anterior to the soma location X) and barcode molecule counts in slices $X + 3$ to $X + 8$ (posterior to the soma location), normalized by the total barcode molecule counts in all these slices. Neurons that did not have eight slices on either side (i.e. neurons in the first eight and last eight slices in the PC) were excluded from this analysis; p values were calculated using a sign rank test (Figure S7K).

To predict soma positions using the piriform output projections, we trained a linear regression model using the piriform output projections as inputs to predict soma A/P positions. We also trained a random forest model (default settings using TreeBagger in MATLAB with 200 trees) in regression mode to predict soma A/P positions using the group labels. For both models, the performance was evaluated using 10-fold cross validation (Figures S8I and S8J).

Matching of PC input and output circuit motifs

To check for input-output circuit motifs, we calculated the conditional probability matrix from the PC injection data, that is the probability of a barcode molecule being sampled from a target region, given that the barcoded neuronal somata is located in a given PC slice. The PC output projection data on target regions was pooled over each target region (r) sampled. To compute the conditional

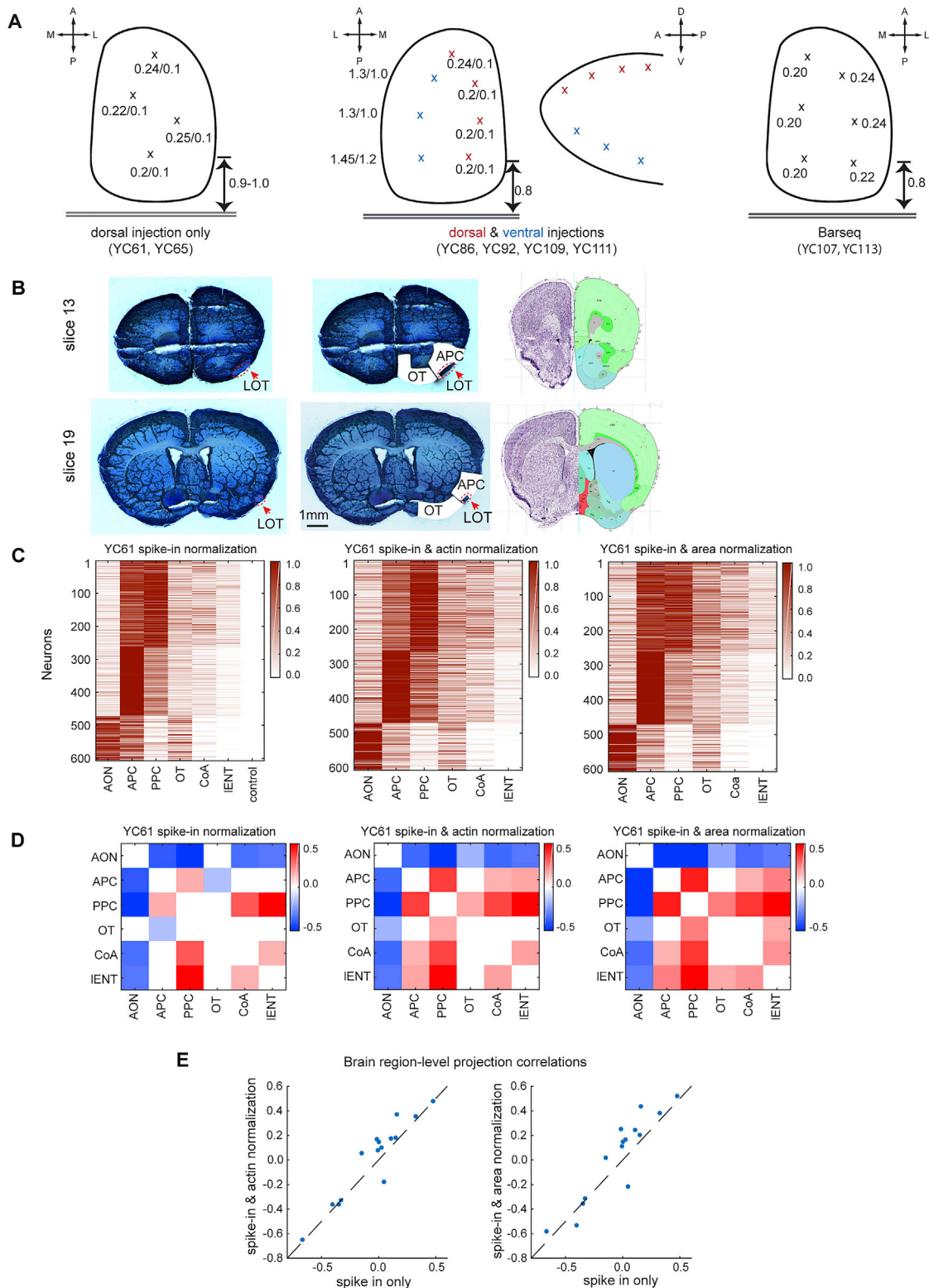
probability of projecting from PC to another region, $p_{PCx}(r|s)$, the equations described above [Equation 3] were slightly amended. Indeed, $p_{PCx}(r|s)$ reflects the rate of projections given that the soma is present at slice s , not an axonal collateral/branch, as in $p(r|s)$ [Equation 3]. Instead of using the distribution of molecules of a barcode $p(s|b) = C(b,s)/\sum_{s' \in PC} C(b,s')$, we used a delta function as the probability distribution of the somata labeled by that barcode: $p_{soma}(s|b) = \delta\left(s, \arg \max_{s'} (B(s',b))\right)$, where $B(s,b)$ are the spike-in normalized molecule count of barcode b in a PC viral injection experiment. We then repeated the calculations that led to Equation 3 to compute $p_{PCx}(r|s)$ (Figure 6A). The probability of barcode b was calculated as $p(r|b) = C(r,b)/(\sum_{r \in target} C(r,b))$, where $C(r,b)$ is the counts of the barcode measured in target region r . We evaluated $p(b|s) = \begin{cases} 1/N_{B, slice} & b \in s \\ 0 & otherwise \end{cases}$ directly, where $N_{B, slice}$ is the number of barcodes with somas located at the specified PC slice. The conditional probability from these quantities was calculated as $p(r|s) = \sum_b p(r|b)p(b|s)$. This conditional probability matrix is interpreted as the mean normalized projection strength from PC to a given target region. We further performed PCA on the $N \times 4$ projection matrix containing the projection strengths to the four extra-piriform areas (AON, OT, CoA, and IENT), where N is the number of PC output neurons. The mean loadings of the first two principal components for PC neurons at each A-P location were then plotted to examine the slope change in projection gradients at the APC/PPC boundary (Figure 6B).

We further calculated the Spearman correlation between the conditional probability matrix of PC inputs and mean projection strength matrix of PC outputs along the A-P axis of piriform cortex with respect to the four extra-piriform target regions sampled (Figure 6C). To visualize the evolution of the projection strengths along the AP axis of the PC, we used a Bézier curve to interpolate a curve representing the two conditional probabilities. We used the formula $B(t) = \sum_{n=0}^N \binom{N}{n} t^n (1-t)^{N-n} P_n$; where P_n is the coordinate constructed by the PC slice $n+1$ and the entries in the two conditional probability matrices.

Statistics

Statistical tests used are indicated in the main text and are two-tailed. All p values are reported after Bonferroni correction.

Supplemental figures



(legend on next page)

Figure S1. Olfactory bulb barcoded Sindbis virus injections and normalization schemes, related to Figures 1 and 2

(A) Schematics for multiple site injections in the olfactory bulb of the barcoded Sindbis virus. The most posterior injection sites are 0.8–1.0 mm rostral to the major blood vessel behind the bulb. Brains of YC61&YC65 (left) were injected at four sites (indicated by x) at two depth of 0.2–0.25 and 0.1 mm (indicated next to injection site) on dorsal side of the bulb. YC86, YC92, YC109, YC111 (middle) were injected at multiple sites on both dorsal (indicated as red x) and ventral aspects of the bulb (indicated by blue x). Each site was injected at two depths (distance in mm next to injection site in schematics). BARseq Brains YC107&YC113 (right) were injected at six sites (indicated as x) on the dorsal OB at a single depth of 0.2–0.25 mm (indicated next to injection site). Details of injection coordinates are provided in [methods](#).

(B) Laser Capture Micro-Dissection of target brain regions from Nissl stained coronal sections (Left: before dissection, middle: after dissection) and corresponding sections registered to the Allen Brain reference atlas (Right). LOT in each brain section is indicated by red dashed line.

(C) Brain area resolution projection matrices of one example brain (YC61) normalized based on spike-in RNA only, spike-in RNA and β -actin (measured by qPCR), and spike-in RNA and dissected brain area size ([methods](#)). Projection strength of each barcode has been normalized to the maximum projection across different brain regions. Data have been arranged into three groups identified by Louvain Community Detection.

(D-E) Pearson correlation between olfactory bulb projections to different brain regions for data normalized to spike-in RNA only, spike-in RNA and actin and spike-in RNA and dissected brain area size for one example dataset (YC61). Only statistically significant correlations (after Bonferroni correction) are shown. Each dot in panel (E) represents a Pearson correlation between bulb projections to different brain regions for data normalized to spike in RNA only (x axis) and spike-in RNA and actin (y axis, left) or spike-in RNA and dissected brain area size (y axis, right).

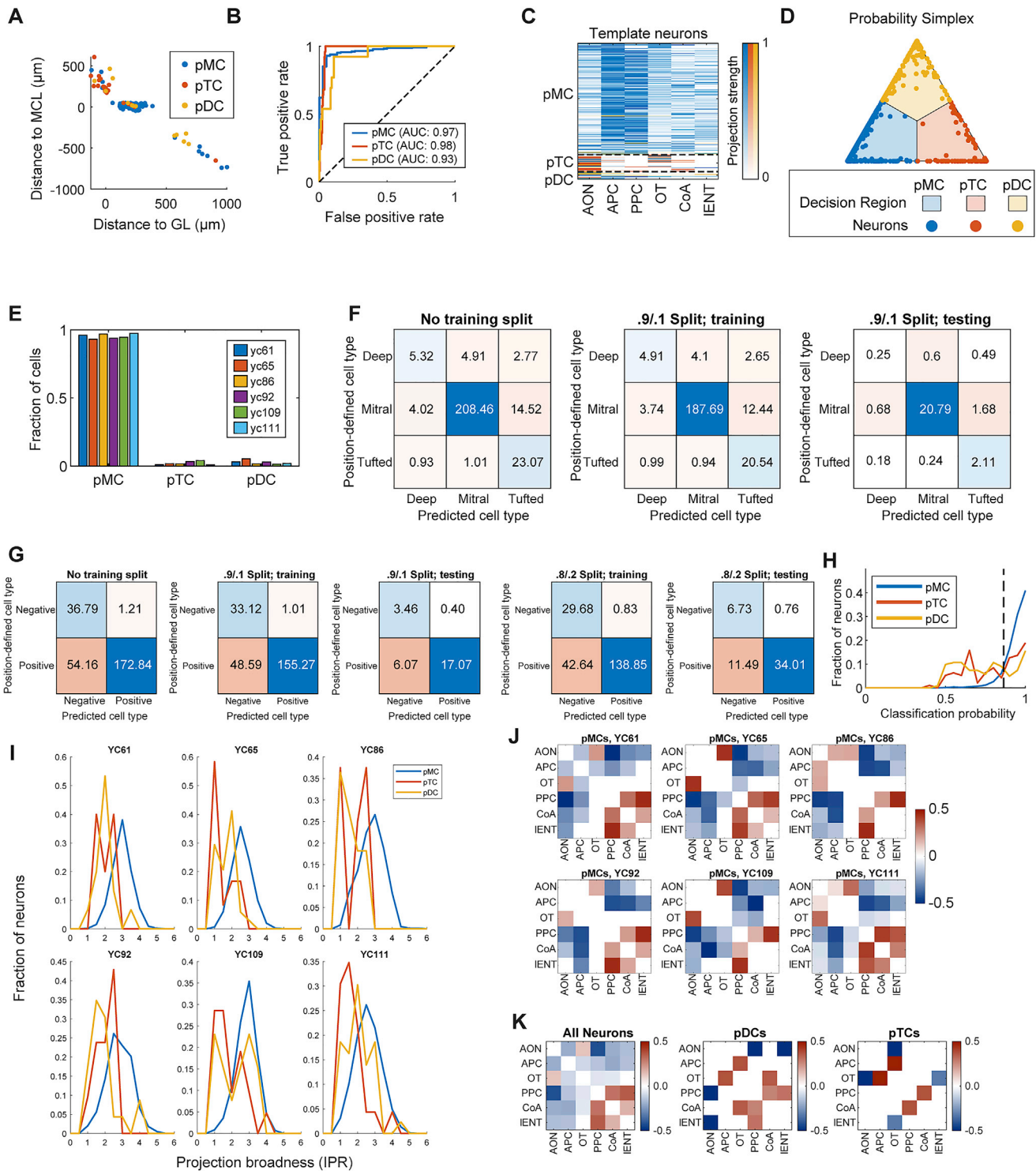


Figure S2. Classification of the olfactory bulb output neurons based on their projection patterns using BARseq data as template, related to Figures 1 and 2

(A) Template neurons identified via BARseq shown in physical space (distance to mitral cell layer, MCL vs. distance to glomerular layer), color coded by the classifier assigned identities (blue - pMC, red - pTC and yellow - pDC).
 (B) Receiver Operating Characteristic (ROC) analysis of the classifier for all three classes.
 (C) Projection patterns of the template neurons. Neurons are sorted according to classifier results and color coded by their true labels based on soma positions in the olfactory bulb (blue - pMC, red - pTC, yellow - pDC).

(legend continued on next page)

(D) MAPseq neurons shown in the space of their classification probabilities, projected onto a 2D plane.

(E) Fraction of classes identified in each individual brain (color coded).

(F) The classification confusion matrix of template neurons, determined by the maximum probability of classification. Matrix values shown were averaged over 500 trained networks, trained on the entire dataset (left), and using a 90%/10% training (center) and testing (right) split.

(G) The classification confusion matrix of template neurons, using a thresholding criterion of pMCs probability larger than 85%. Matrix values shown were averaged over 500 trained networks, trained on the entire dataset (left), using a 90%/10% training/testing (center-left/center) split, and a 80%/20% training/testing (center-right / right) split.

(H) The distribution of classification probability for each class. Dashed vertical line indicates 85% probability threshold.

(I) The distribution of IPR across individual brains.

(J) The Pearson correlation between projections to different areas in pMC in each individual brain.

(K) Pearson correlation between projections to different areas in all neurons, pDC, and pTC. Only statistically significant correlations (after Bonferroni correction) are shown.

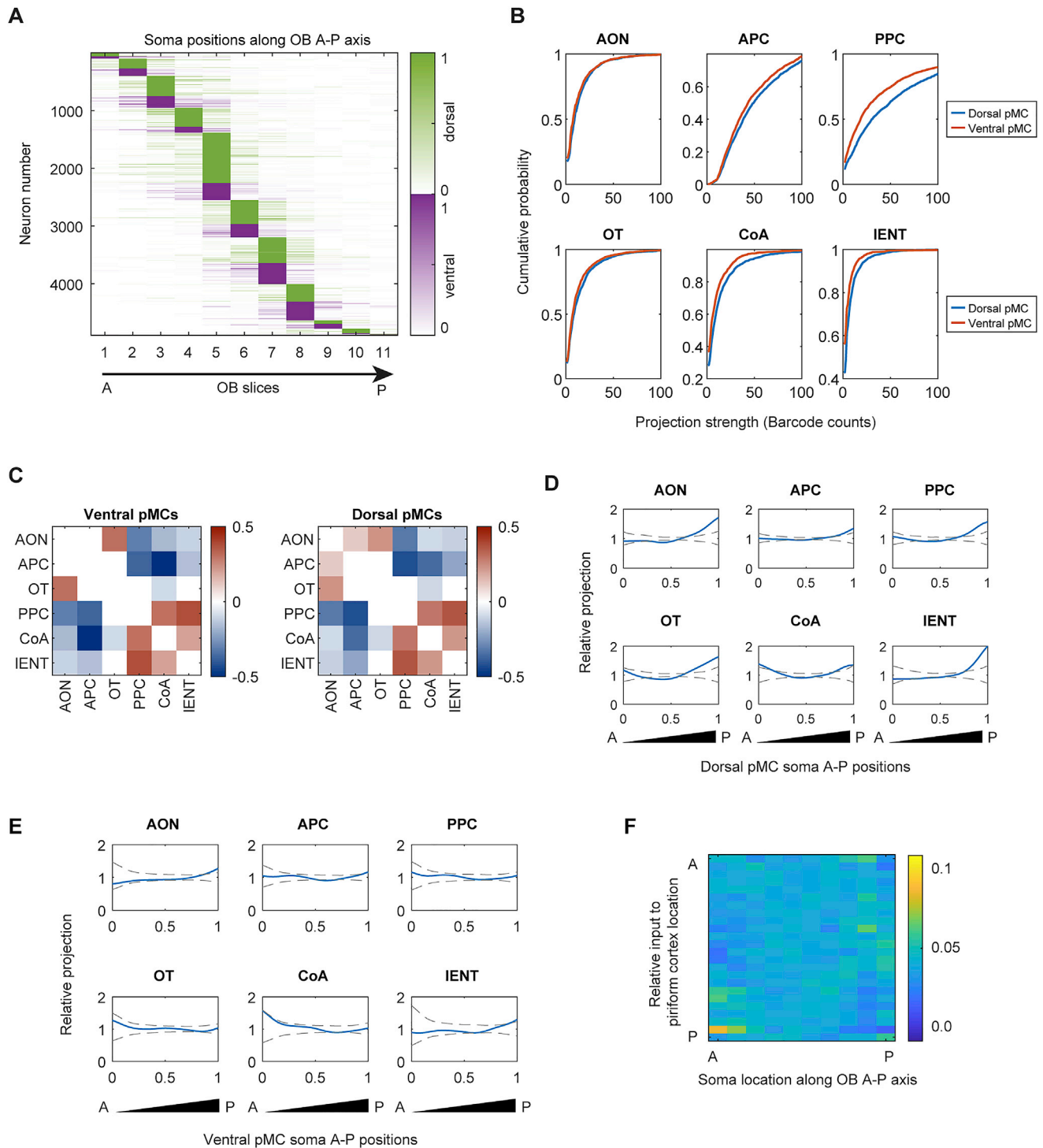


Figure S3. Spatial distribution of barcode labeled pMC somata and projection patterns as a function of different locations within the olfactory bulb, related to Figure 2

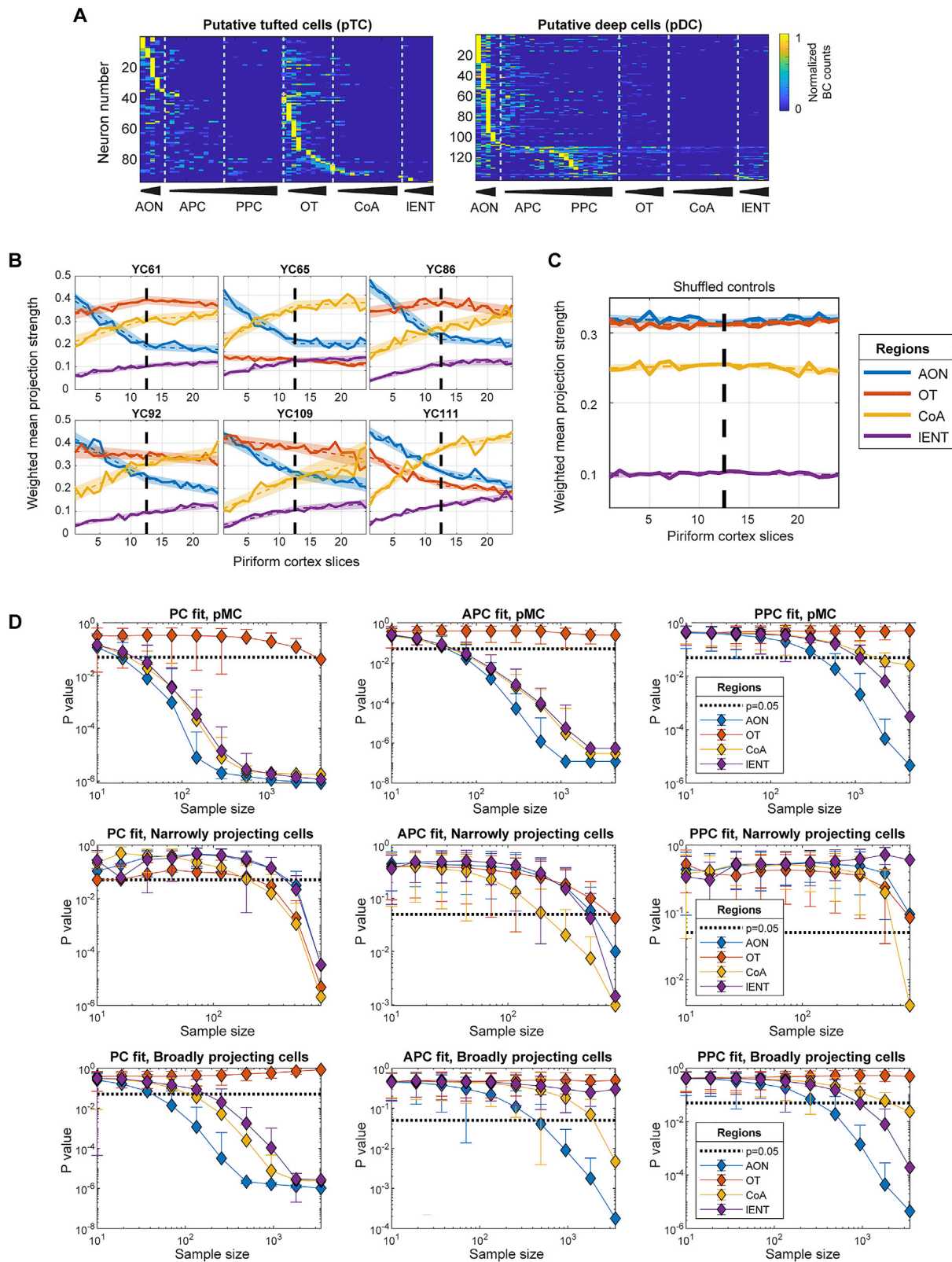
(A) Barcode counts in the olfactory bulb. Neurons are sorted by the peak positions, which indicate the soma locations along the A-P axis of OB. Projection patterns are color coded by the dorsal (green) and ventral (purple) location of their somas.

(B) Cumulative probability distribution of the strength of projections of dorsal and ventral pMC to the indicated brain regions.

(C) Pearson correlation between projections to different bulb target regions for the pMC neurons from the ventral and dorsal aspects of the bulb. Only statistically significant projections are shown.

(legend continued on next page)

(D and E) Relative projection strengths of dorsal (D) and ventral (E) pMC from specific A-P positions in the bulb (x axis) to the indicated olfactory bulb target regions. The projection strength was normalized to the mean projection strength of all dorsal or ventral pMC neurons. Dashed lines indicate 95% confidence interval obtained by shuffling the A-P positions of neurons. (F) Relative projection strengths of pMC neurons to different piriform cortex A-P positions for neurons at different A-P locations within the olfactory bulb. Each column shows the ratio between the mean projection strengths of neurons at the indicated A-P locations in the olfactory bulb (x axis) to different A-P locations in the piriform cortex (y axis) and the mean projection strengths of all neurons to different A-P locations in the piriform cortex (y axis). These ratios are further normalized by the sum of each column to allow visualization.



(legend on next page)

Figure S4. Reproducibility across individuals, shuffled controls and downsampling analysis on the projection patterns of the olfactory bulb output neurons, related to Figure 3

(A) Slice-level (200 μm resolution) projections of pTC and pDC neurons, sorted by the location of their peak positions along the A-P axis of each of the olfactory bulb target regions sampled. Projections were normalized to the maximum projection within each row.

(B and C) Weighted mean co-innervation strength across piriform cortex slices and extra-piriform areas [the conditional probability of co-innervation $P(\text{target}|\text{PC location})$, solid lines] in each of the six brains sampled (B) and the same data obtained by shuffling the piriform cortex slices (C). Dashed lines/shaded areas show piecewise linear fits in APC and PPC with the 95% confidence interval obtained by bootstrap.

(D) Distribution of p values of Spearman correlations after down sampling. The Spearman correlations are calculated between the A-P position of the piriform cortex slice and the weighted mean co-innervation strengths between target regions and the piriform cortex slice considered. Spearman correlation was calculated across the entire piriform cortex (left column), only on APC (center column) and only on PPC (right column). Barcodes used for down sampling were selected among all pMC neurons (top row), narrowly projecting neurons (center row) and broadly projecting neurons (bottom row). Sample sizes are as shown on the x axis of each plot.

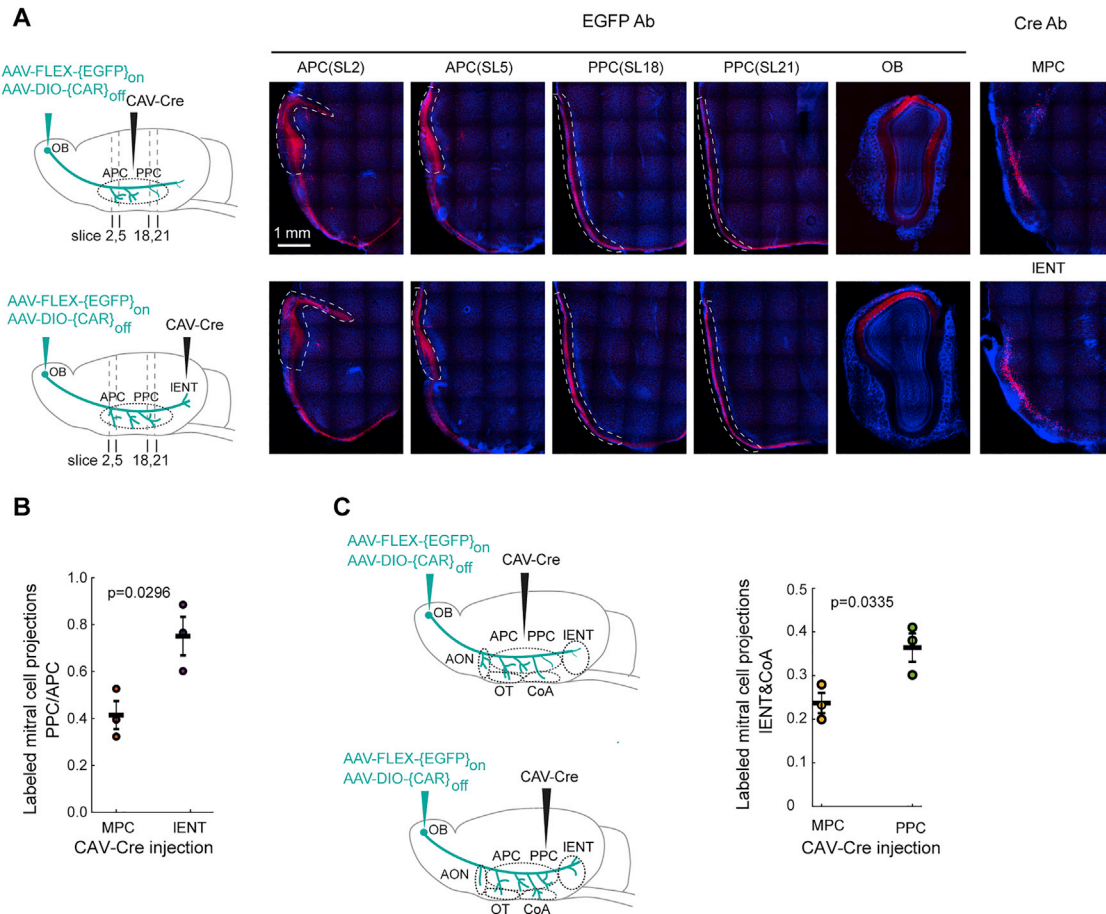
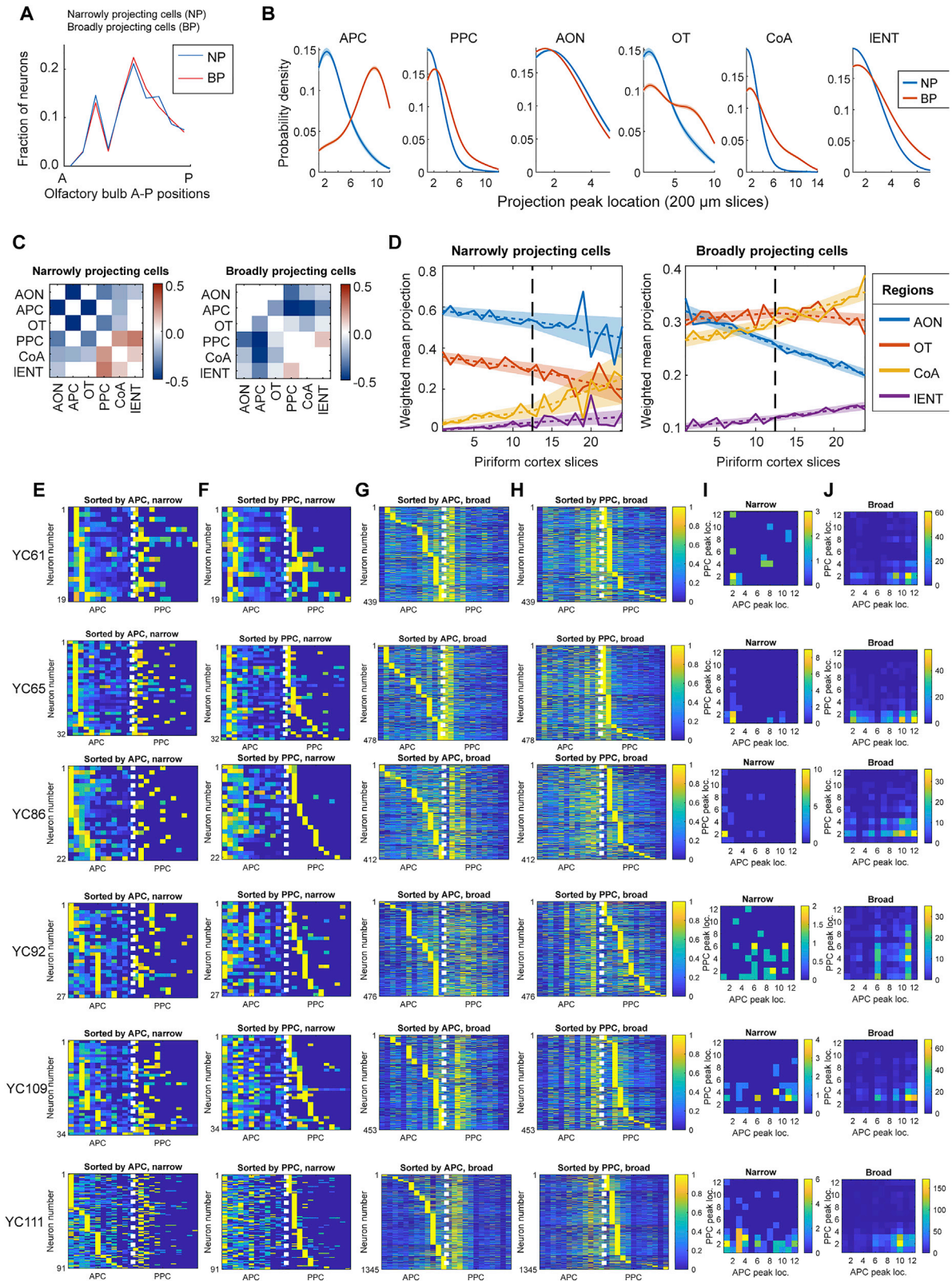


Figure S5. Validation of the spatial organization of pMC projections using CAV-Cre bulk retrograde labeling, related to Figures 2 and 3

(A) Left, schematics of CAV-Cre retrograde labeling in the middle of piriform cortex (MPC, top panel) and IENT (bottom panel). Center, immunofluorescence of labeled mitral cells at different A-P positions of piriform cortex and olfactory bulb. Mitral cell projections to piriform cortex are largely restricted to layer I, as indicated by white dashed lines. Right, immunofluorescence of Cre at MPC (top panel) and IENT (bottom panel).

(B) The ratio of projection strength of labeled mitral cells (as measured by EGFP immunofluorescence) in the posterior portion of the piriform cortex (slices 17–22) to the labeled mitral cell projection strength in the anterior portion of the piriform cortex (slices 1–6). Each dot represents data collected from an animal. Bars indicate mean \pm SEM $n = 3$ mice in each group, $p = 0.03$ by Student's t test.

(C) Left, schematics of CAV-Cre retrograde labeling in the middle of piriform cortex (MPC, top panel) and PPC (bottom panel). Right, the projection strength of labeled mitral cells (as measured by EGFP immunofluorescence) in IENT and CoA normalized by the total projection strength in extra piriform regions including AON, OT, IENT and CoA. Each dot represents data collected from an animal. Bars indicate mean \pm SEM $n = 3$ mice in each group, $p = 0.03$ by Student's t test.



(legend on next page)

Figure S6. Spatial organization of the projections of broadly projecting and narrowly projecting cells, related to Figure 4

- (A) The fraction of broadly and narrowly projecting neurons' somata along the A-P axis of the olfactory bulb.
- (B) Distribution of projection peak positions, smoothed using a gaussian kernel, in the indicated areas for the narrowly and broadly projecting putative mitral cells.
- (C) Pearson correlation between projections to different areas of the narrowly and broadly projecting neurons. Only statistically significant (after Bonferroni correction) correlations are shown.
- (D) Mean projection strengths (solid lines) in the indicated extra-piriform bulb target brain regions weighted by projection strengths to the indicated A-P position in the piriform cortex (x axis) for the broadly and narrowly projecting neurons. Dashed lines indicate piecewise linear fits in APC and PPC and shaded areas indicate range of fits from bootstrapping.
- (E-J) Same plots as Figures 4E-4J, but plotted for each brain separately. (E, F) Narrowly projecting neurons sorted independently by the strength of their projection maxima along A-P axis of APC (E) and PPC (F).
- (G and H) Same for broadly projecting neurons sorted by the strength of their projection maxima along the A-P axis of APC (G) and PPC (H). Colors indicate the projection strength at a given location with respect to the maximum projection to APC or PPC.
- (I and J) Density plots of the distribution of peak projection positions of the same neurons within APC (x axis) and their peak projection positions in PPC (y axis). Colors indicate number of neurons.

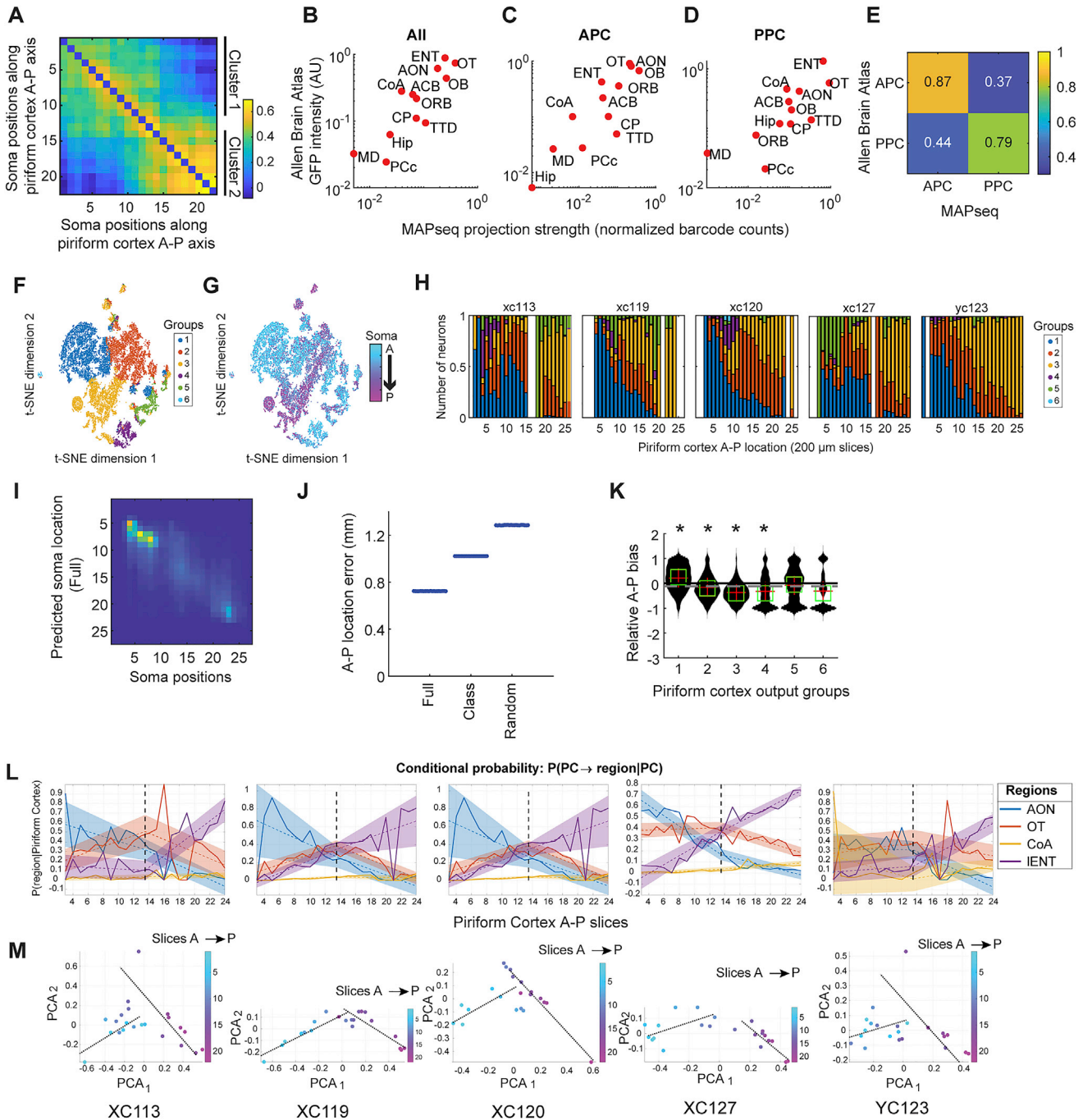


Figure S7. Differential brain-wide projections of groups of piriform cortex output neurons organized in a graded manner along the A-P axis, related to Figures 5 and 6

(A) Spearman correlation between barcode counts in different piriform cortex slices. Clusters indicated on the right indicate highly inter-connected slices obtained by Louvain community detection (see [methods](#)).

(B-D) Projection strengths from the Allen Brain Atlas (ABA) (y axis) and sum of barcodes of neurons from MAPseq (x axis) for the indicated areas for all the piriform cortex neurons (B), APC neurons (C), and PPC neurons (D).

(E) Pearson correlations between the projection strengths from the Allen Brain Atlas (ABA) and barcode counts from MAPseq separately for APC and PPC.

(F-G) t-SNE plots of the piriform cortex output projections color coded by groups defined by the output projections (F) and soma locations (G).

(H) The fraction of neurons belonging to each group at the indicated A-P positions, plotted separately for each brain.

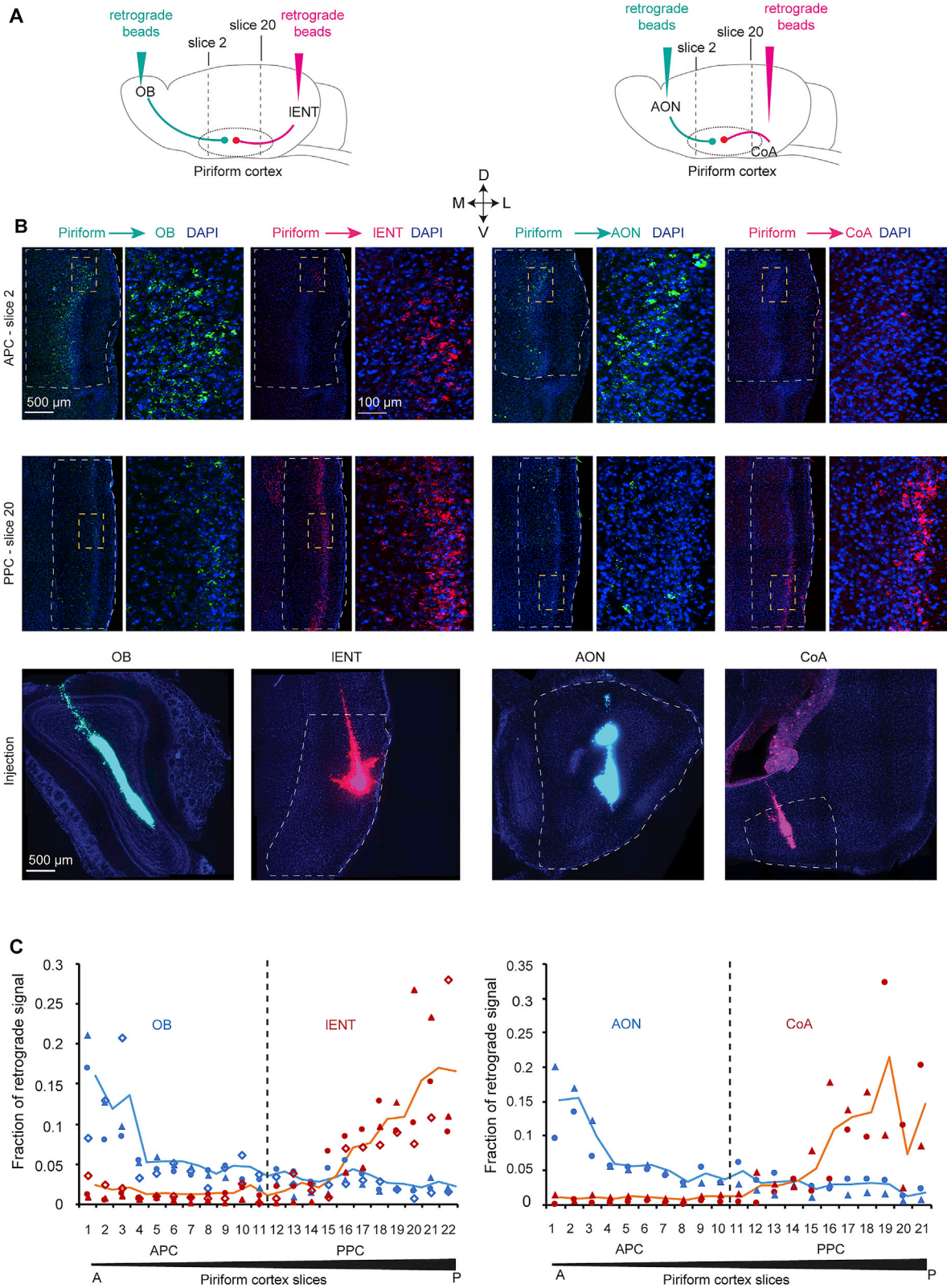
(I) Prediction of soma locations (y axis) using full projection pattern.

(legend continued on next page)

(J) Mean prediction errors of the A-P positions of piriform cortex neuronal somata using full projection pattern, group identities, and randomized output projection patterns. Individual dots indicate trials using cross validation. (K) Differences in intra-piriform cortex projections in the anterior and posterior directions for each piriform cortex projection group identified (methods). Positive numbers indicate stronger anterior projections and negative numbers stronger posterior projections. Dashed line indicates mean projection bias for all the piriform cortex output neurons; * $p < 10^{-10}$ compared to no bias using sign rank tests after Bonferroni correction.

(L) Mean projection patterns of piriform cortex output neurons from the indicated A-P position of barcoded somata in the piriform cortex. Dotted lines indicate linear fits and shaded areas the range of fits from bootstrap.

(M) Mean loadings for the first two principal components of the mean projection strengths of piriform output neurons to AON, CoA, IENT and OT sampled at the indicated A-P positions in the piriform cortex. Dotted lines indicate linear fits for APC and PPC.



(legend on next page)

Figure S8. Validation of piriform cortex output projection patterns along A-P axis via bulk retrograde tracing, related to Figure 6

(A) Cartoon schematics of injecting retrograde beads of different colors into the olfactory bulb vs. IENT and the AON vs. CoA.

(B) Representative example images of retrograde labeling at different A-P positions in the piriform cortex and labeling at different injection sites. A selected area (golden rectangle) in each piriform cortex slice is amplified on the right.

(C) Quantification of retrograde labeling from different brain regions along the A-P axis of the piriform cortex. Retrograde fluorescence signals in the piriform cortex from bulb injections (Left) and AON injections (Right) are shown in blue; retrograde signals from IENT (Left) and CoA (Right) are shown in red. Different shapes represent different animals (3 mice for co-injection into OB & IENT; 2 mice for co-injection into AON & CoA); solid lines indicate the mean across different animals. Individual piriform cortex slices are 100 μm coronal sections arranged from the anterior to the posterior end of the cortex and spaced 200 μm apart. Spearman correlation between the A-P positions of neurons and projection strengths were $\rho = -0.94$, $p = 2.0 \times 10^{-5}$ for AON, $\rho = 0.92$, $p = 1.7 \times 10^{-5}$ for CoA, and $\rho = 0.74$, $p = 4.4 \times 10^{-4}$ for IENT after Bonferroni correction; $n = 2$ mice for AON and CoA and 3 mice for IENT.